A Slow Control System with Gain Stabilization for a Small Animal MR-Compatible PET Insert

By

Ehsan Shams

A Thesis Submitted to the Faculty of Graduate Studies of
The University of Manitoba
in partial fulfillment of the requirements of the degree of

MASTER OF SCIENCE

The Graduate Program in Biomedical Engineering
University of Manitoba
Winnipeg, Manitoba, Canada

Abstract

The Biomedical Imaging Lab at the University of Manitoba is building an MR compatible PET insert system for simultaneous PET-MR imaging of small animals inside a 7T animal MR imaging system. This system consists of detector modules, signal readout circuitry, data acquisition, coincidence detection, and image reconstruction components. The detectors in this system are based on SensL SPM ArraySB-4 silicon photomultipliers (SiPMs) and dual layer offset LYSO crystal blocks with 409 total crystals per detector. The gain of the detectors varies with temperature and bias voltage. Measurements obtained while the PET insert system was operating inside the MR magnet bore revealed that the equilibrium temperature of the SiPMs was around 30°C.

The photopeak amplitude, energy resolution and the number of events recorded per crystal were studied at the baseline temperature (30°C) and also at temperatures ranging from 20°C to 40°C. One series of measurements was obtained with a fixed overvoltage of 2.5V above the breakdown voltage and another with a fixed bias voltage of 27.95V. It was determined that maintaining a fixed overvoltage would help stabilize detector output but was not sufficient. A study of detector characteristics versus overvoltage at the baseline temperature was subsequently conducted. The results of this study were used to construct a lookup table to adjust bias voltage to achieve better stabilization. Results show an acceptable and stable output. A control system is required to oversee the operation of these detectors. The control system developed in this thesis project is a distributed network-based control system that monitors the operating parameters of the detectors.

Acknowledgements

I would like to thank the following individuals without whose support this project would not have been completed:

- Dr. Andrew L. Goertzen, my academic advisor, who mentored me throughout my studies and provided plenty of valuable insight.
- Dr. Jonathan D. Thiessen, who generously took time to answer my questions especially during the first formative months of starting this project and helped me gain an understanding of PET imaging.
- Graham Schellenberg and Bryan McIntosh, my colleagues and fellow graduate students at the time of writing this thesis. I wish you guys all the best always.
- Greg Stortz, for his help with data analysis
- Daryl Bishop, for his input on the design of the power distribution board and the use of Altium®
- My Mom, the tireless advocate of post-graduate education, who never ceases to believe in me.
- And my best friend and partner in life, Mary. Thanks for being there as always.

Contents

List of Tables

List of Figures

List of Copyrighted Material

- Figure 1-2 from (Wehrl, Judenhofer, Wiehr, & Pichler, 2009); reprinted with permission from Springer
- Figure 1-3 from (Pichler, Wehrl, Kolb, & Judenhofer, 2008); reprinted with permission from Elsevier
- Figure 1-4 from (Zaidi et al., 2011); reprinted with permission from IOP Publishing
- Figure 1-5 from (S Yamamoto et al., 2009); ©2009 IEEE
- Figure 1-6 from (Lucas et al., 2006); ©2006 IEEE
- Figure 1-7 from (Judenhofer et al., 2008); reprinted with permission from the Nature Publishing Group
- Figure 1-8 from (Ravindranath et al., 2009); ©2009 IEEE
- Figure 1-10 from (Feege, 2008); reprinted with permission from Nils Feege
- Figure 1-11 from (Hong et al., 2012); reprinted with permission from IOP Publishing
- Figure 1-12, Figure 1-13 and Figure 1-14 (left) from (Marrocchesi et al., 2009); reprinted with permission from Elsevier
- Figure 1-14 (right) and Figure 1-15 (left) from (Petasecca et al., 2008); ©2008 IEEE
- Figure 1-15 (right) from (Ramilli, 2008); ©2008 IEEE
- Figure 1-16 from (Seiichi Yamamoto et al., 2011); reprinted with permission from IOP Publishing

List of Abbreviations

APD.....Avalanche Photodiode
BDA ..... Block Detector Analysis
BNL..... Brookhaven National Laboratory
CFD.....Constant Fraction Timing Discriminator
CLUT ..... Crystal Lookup Table
CT .....Computed Tomography
DAC ..... Digital to Analog Converter
DIB.....Detector Interface Board
ELUT ..... Energy Lookup Table
Lutetium Yttrium Orthosilicate.....LYSO
MPPC..... Multiple Pixel Photon Counter
MR .....Magnetic Resonance
MRI.....MR Imaging
OV.....Overvoltage
PDB..... Power Distribution Board
PDE.....Photon Detection Efficiency
PET ..... Positron Emission Tomography
PMT ..... Photomultiplier Tube
RF.....Radio Frequency
SiPM .....Silicon Photomultiplier
SMA.....SubMiniature version A
SNR..... Signal to Noise Ratio

Preamble

A Positron Emission Tomography (PET) insert system is being developed at the Biomedical Imaging Research Group at the University of Manitoba. The goal of this project is to develop a small animal imaging system capable of acquiring simultaneous PET and Magnetic Resonance (MR) images by using the PET insert inside the magnet bore of an existing small animal MR imaging system. The 7T Bruker small animal MR system located in the Chown building at the University of Manitoba was chosen as the MR system for the PET insert. For acquisition and processing of the signals, the PET insert system relies on the OpenPET system under development at the Lawrence Berkeley National Laboratory. A prototype of the detector gantry was constructed in May, 2014 and is depicted in Figure I.

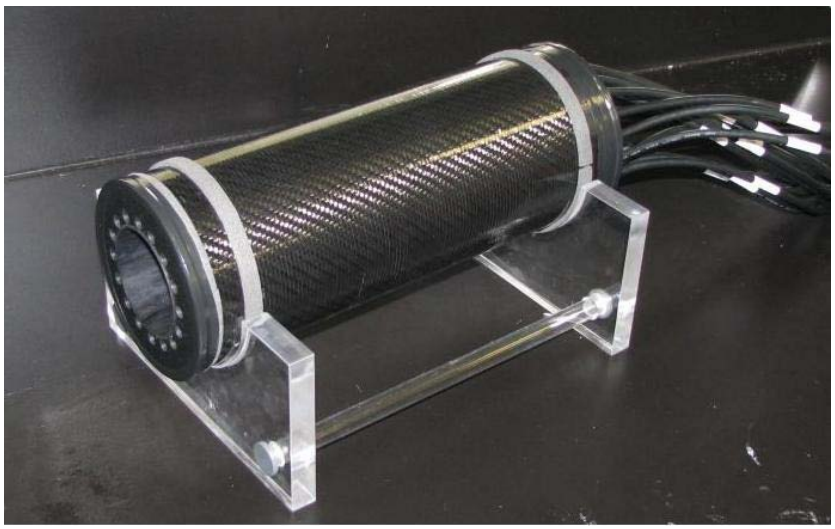

Figure I. The prototype PET insert system constructed in May, 2014 comprises 16 detectors in a ring configuration.

The prototype PET insert has an inner diameter of 60mm and an outer diameter of 114mm with gantry covers constructed out of carbon fiber. The PET insert is limited in its outer diameter by the magnet bore diameter of the MR system. A MR Radio Frequency (RF) coil slides inside the PET insert to avoid disturbance of the RF field of the MR system. This yields an effective bore diameter of 35mm as shown in Figure II. Detectors in this PET insert system are arranged in a

ring configuration forming a gantry. The reasons for this configuration as well as the basics of operation of detector modules are discussed in chapter 1.

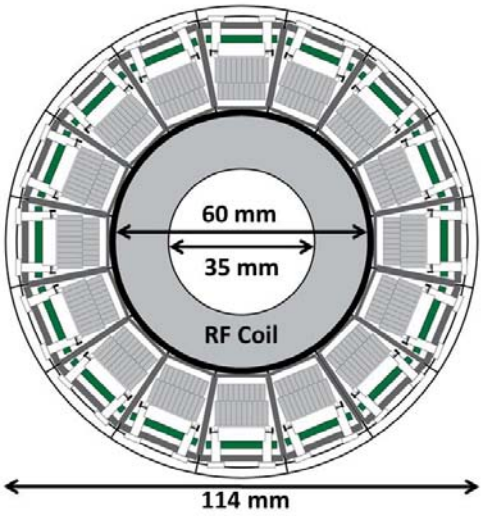

Figure II. The inner and outer diameters of the PET insert are dictated by the magnet bore diameter and the RF coil respectively. The effective bore diameter of the prototype system was equal to 35mm.

This thesis project aimed to implement a control system for the detector modules in the PET insert system. The following were defined as the goals of this thesis project:

1. To study the temperature dependence of gain of the detector modules used in the PET insert system under development at the Biomedical Imaging Research Group at the University of Manitoba and develop a method of compensation for these temperature dependencies.
2. To implement a slow control system capable of controlling the detector modules and providing control and monitoring of the operation of the detector modules in terms of their operating parameters (i.e. voltage, current and temperature).

Chapter 1 lays the groundwork by describing the basics of the operation of a PET imaging system and the rationale for developing a hybrid PET-MR system. An overview of previous

efforts in developing PET-MR systems is presented. This chapter also discusses general challenges in developing such a hybrid system with reference to the relevant literature. Chapter 2 describes in detail the methods and components used in data acquisition and analysis. Most of the experiments and tests in this thesis project have been performed without the OpenPET system. An elaborate system involving readout electronics, sampling and digitization equipment and software programs has been used to acquire signals and to analyze the data. Chapter 3 provides a thorough description of the slow control system developed as part of this thesis project. The results of the study on the temperature characteristics of the detector modules in the PET insert system are discussed in Chapter 4. This chapter also presents details on studies performed to achieve a stable output signal despite fluctuations in ambient temperature. Chapter 5 includes a summary as well as the outlook for future work.

Chapter 1

Introduction

1.1 Positron Emission Tomography

Positron Emission Tomography (PET) is an imaging modality in nuclear medicine that relies on the detection of photons generated as a result of positron annihilation events. Prior to a PET scan, a radio-pharmaceutical (tracer) is injected into the body of the subject. The tracer is chosen so it will follow a specific physiological process or function in the body that needs to be monitored by PET. The nuclei of the tracer atoms emit positrons through the process of decay. The positrons annihilate with an electron and produce two 511keV photons that leave the site of annihilation travelling antiparallel to each other. PET provides information on the distribution of annihilation events by detecting this pair of photons.

PET imaging systems typically use scintillation detectors that consist of a layer of scintillation crystal as well as a photon detector. The crystal converts high-energy annihilation photons to lower-energy optical photons. These lower-energy photons are in turn picked up by photon detectors that produce an electrical signal as their output. Photomultiplier Tubes (PMTs) are the conventional photon detectors used in most PET systems.

The most common topology for detectors of a PET system is that of a ring. Because a pair of photons resulting from the same annihilation event travel at a 180 degree angle from each other, the ring topology is well suited to detect such a pair and locate the site of annihilation. Figure 1-1 shows a schematic of a PET imaging system.

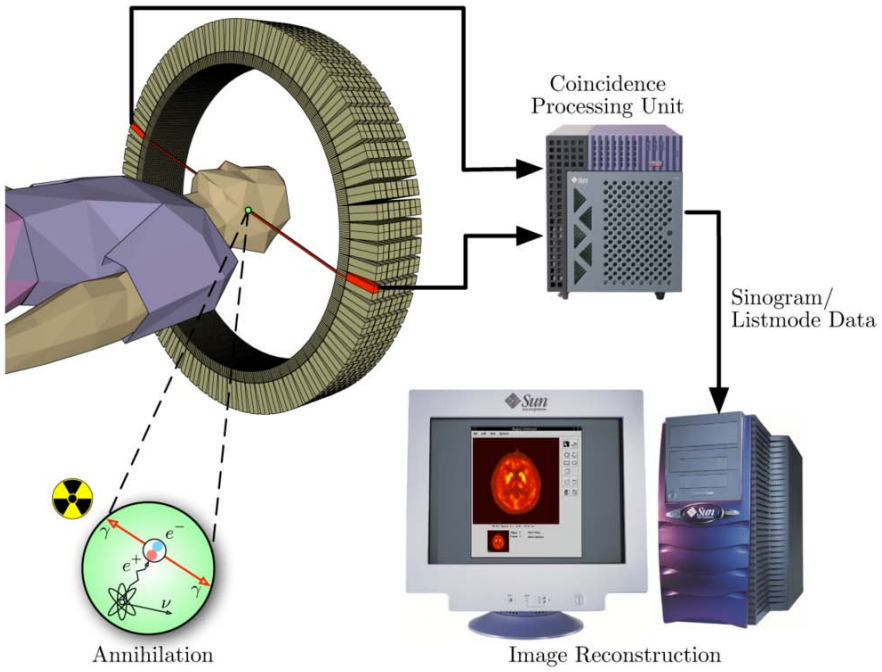

Figure 1-1. Schematics of a PET imaging system.

The output from the PMTs is processed to search for pairs of detected photons originating from the same annihilation event. A pair of photons detected within predefined time and energy windows is assumed to have originated from one annihilation event and is called a coincidence pair. The time and energy window depend mainly on the characteristics of the scintillation crystal. Depending on the type of scintillation crystal used, the timing window could range from 3ns to 20ns and the acceptable energy window could be within 6% to 25% of 511keV. Coincidence data is then sent to the image reconstruction system (Muehllehner & Karp, 2006; Phelps, 2000).

1.2 Bimodal PET imaging systems

PET often provides little anatomical information as tracers bind to biochemicals involved in various physiological processes. To get the benefit of combining functional data obtained by PET with anatomical data, bimodal imaging techniques are employed. One such bimodal imaging technique is PET-Computed Tomography (CT). PET-CT systems are among the most

frequently installed systems in nuclear medicine imaging centres and are far more common in clinical use than PET-only systems (Beyer, Czernin, & Freudenberg, 2011). In a PET-CT system, acquisition of PET and CT images is done sequentially in an integrated system. It is not possible to acquire images from both modalities at the same time as the flux of radiation required for CT imaging would saturate PET detectors (Basu et al., 2011). Furthermore, incompatibilities in the geometrics of PET and CT systems lead to compromises in system imaging performance.

1.3 The case for a PET-MR system

PET and MR Imaging (MRI) are both powerful imaging modalities at the molecular level. As a diagnostic imaging modality, MRI offers advantages over CT due to its higher image resolution and better soft tissue contrast. Unlike CT, MRI does not use ionizing radiations. It also offers functional MRI, Magnetic Resonance Spectroscopy (MRS) and perfusion measurements. PET is the most powerful tool for monitoring biochemical processes at the molecular level. It is able to provide information at sub-pico-molar levels. (Delso & Ziegler, 2009; Wehrl et al., 2009).

A PET-MR system can assist research and diagnosis in several key application areas. Anatomical data from MRI can be combined with functional data from PET scans. It is also possible to monitor function at different levels with simultaneous PET and MRI. There are several areas where PET and MRI both can provide information that complement each other. Data obtained from PET and MRI can be used in conjunction in areas such as measuring perfusion and blood flow, glucose consumption, blood/tissue oxygenation, cell labeling, neurotransmitters, receptor density, metabolite concentration and tissue pH. Figure 1-2 shows images obtained by PET, MR and CT imaging of a mouse injected with a Cu labeled antibody. The MR image offers superior soft tissue contrast to the CT image. The PET image clearly depicts tracer uptake in both the kidneys and to a lesser extent in the tumour (Wehrl et al., 2009).

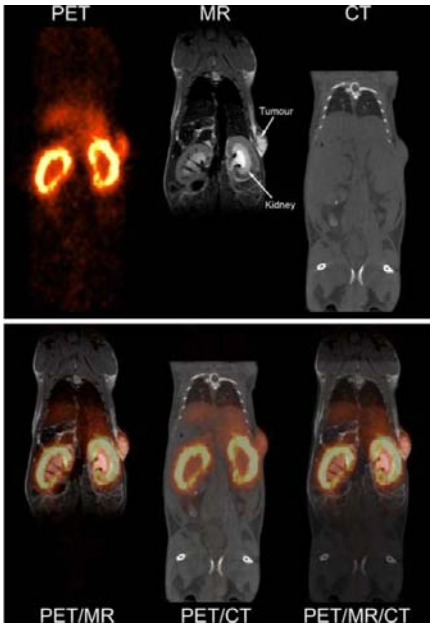

Figure 1-2. Comparison of single modality PET, CT and MRI with combinations of imaging modalities, in images of a mouse injected with a Cu-64 labelled antibody (Wehrl et al., 2009). Reprinted with permission from Springer.

1.4 PET-MR and small-animal research

Small animal models in imaging have gained attention since the 1980's for research and preclinical purposes. Advances in imaging techniques of small animals have enabled non-invasive study of various disease states and monitoring of response to treatments. Developing more effective imaging techniques is a key component in enhancing the accuracy of small animal research.

Both PET and MRI have been extensively used in small animal research. Small animal MRI has been used in the study of cancer in several organs including the brain, lungs and prostate. It has also been used to evaluate the effects of therapy. PET studies in small animals have led to the development of new tracers for PET and contributed to cancer research by providing the opportunity to non-invasively monitor various stages of disease progression (Lewis, Achilefu, Garbow, Laforest, & Welch, 2002).

Several groups have worked on the development of bimodal PET-MR systems for small-animal research. Such systems face challenges stemming from the nature of research on small animals as well as complications of combining two different imaging modalities with potentially conflicting properties. For example, due to the small size of animals, the radiotracers must be used in small doses. In small animal PET applications, special attention has to be devoted to maintaining the spatial resolution and detection sensitivity of the imaging system. Maintaining image quality is a challenge as the size of the animal decreases and the amount of injected radiopharmaceuticals is limited (Chatziioannou, 2002).

1.5 Challenges in combining PET and MRI

PET and MRI have properties that come into conflict with each other when the two imaging modalities are combined into a single system for simultaneous use. The MRI relies for its operation on a constant magnetic field (B_0), a changing magnetic field (the gradients) and a probing RF field (B1). PET is dependent on successful localization of positron annihilation events by detecting pairs of incident photons. The main obstacle in obtaining PET images in proximity to a MR magnet is the sensitivity of photomultiplier tubes in the PET system to magnetic fields. Figure 1-3 shows how the detector elements map of a PMT is distorted in the presence of a magnetic field.

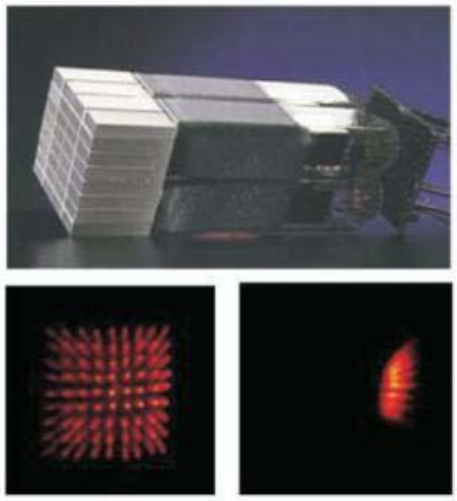

Figure 1-3. Map of detector elements from a PMT (pictured above) in absence of magnetic fields (left) and in presence of a 7T magnetic field (right) (Pichler, Wehrl, Kolb, & Judenhofer, 2008). Reprinted with permission from Elsevier.

The most straightforward solution to the problem of magnetic interference to the PET system from MRI is to use the two systems sequentially while ensuring that the PET system is properly shielded from the magnetic field of the MRI. One commercially available clinical PET-MR system from Philips Medical Systems uses this approach. In this system, a 3T self-shielded MRI magnet is used in the same room as the PET system. The distance between the centres of the fields of view of the systems is 4.2m. Additional shielding is used around the PET gantry to guard it against the magnetic field flux from the MRI. This approach requires no basic modifications to the typical MRI and PET systems; however, the sequential use of MRI and PET means that longer MR imaging sequences could lead to significantly longer PET-MR scan times (Zaidi et al., 2011). Figure 1-4 shows a schematic representation of this system installed at Mount Sinai Medical Center, NY and Geneva University Hospital in Geneva, Switzerland.

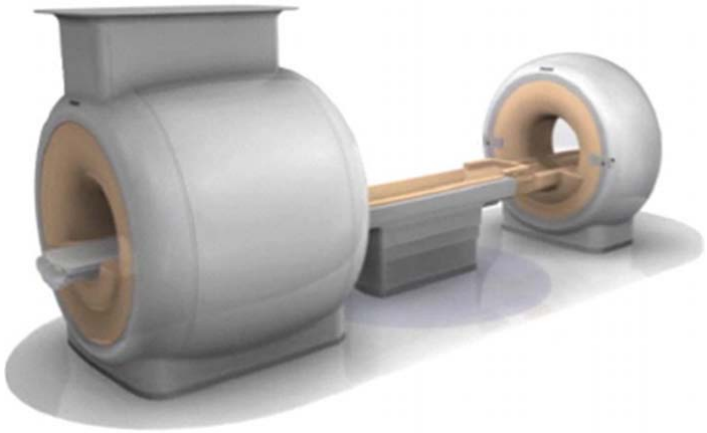

Figure 1-4. The sequential PET-MR imaging system developed by Philips Medical Systems (Zaidi et al., 2011). Reprinted with permission from IOP Publishing.

As another approach, some developers of PET-MR systems have chosen to position the PMT's far from the reach of the MRI magnetic field. In one of the first PET-MR systems, optical fibers were used to connect the scintillators, positioned in a ring inside the gantry, to the PMT's so that the PMT's could be kept outside of the MR magnetic fringe field (Shao et al., 1997). Another similar PET system developed at the University of West Virginia used optical fibers of length 2.5 meters (Raylman et al., 2006).

The use of fiber optics makes it possible to use PMTs in hybrid PET-MR systems, but it has some disadvantages. When dealing with the small magnet bore diameters of small-animal research MRI systems, it is not practical to route the bundle of optical fibers out of the MRI gantry especially as the number of detectors increases. This imposes restrictions on the scalability of the system. Furthermore, long fibers cause light loss and a degraded timing resolution, both of which are undesirable in PET systems (Shao et al., 1997). Figure 1-5 shows the detector ring of a PET insert system developed by Yamamoto et al. (2009) where optical fibers of length 2.6m are used to carry the light away from the magnetic field of the MR system.

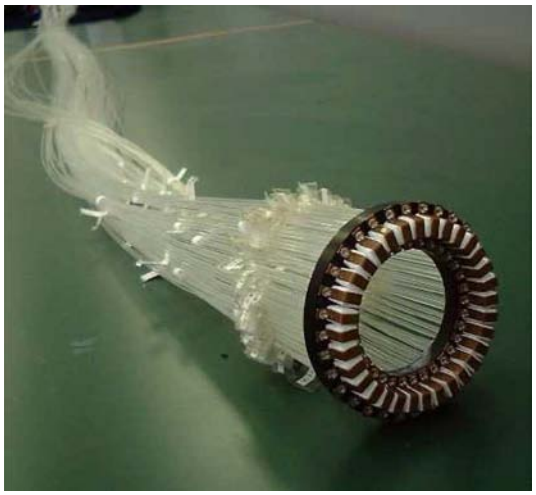

Figure 1-5. 2.6m Optical fibers used to carry the light from scintillators to PMT's in a PET/MR system (S Yamamoto et al., 2009). ©2009 IEEE

Another proposed solution has been to alter the MRI system to facilitate the use of PET. A group at the University of Cambridge has used a split magnet MRI to make room for fiber optics that are used to route the light from the scintillating crystals to the PMT's located outside and around the magnet bore (Lucas et al., 2006). Figure 1-6 shows a schematic of this system. This solution requires a special magnet design and is costly. Furthermore, the fact that PET detectors are in close proximity to the split-magnet means that a MR magnet with a lower field strength has to be used in this approach. As another example of altered MR designs, a team at the University of Western Ontario has designed a field-cycled MRI system which allows PET imaging to be performed when the magnetic field of the MRI system is turned off (Handler, Gilbert, Peng, & Chronik, 2006).

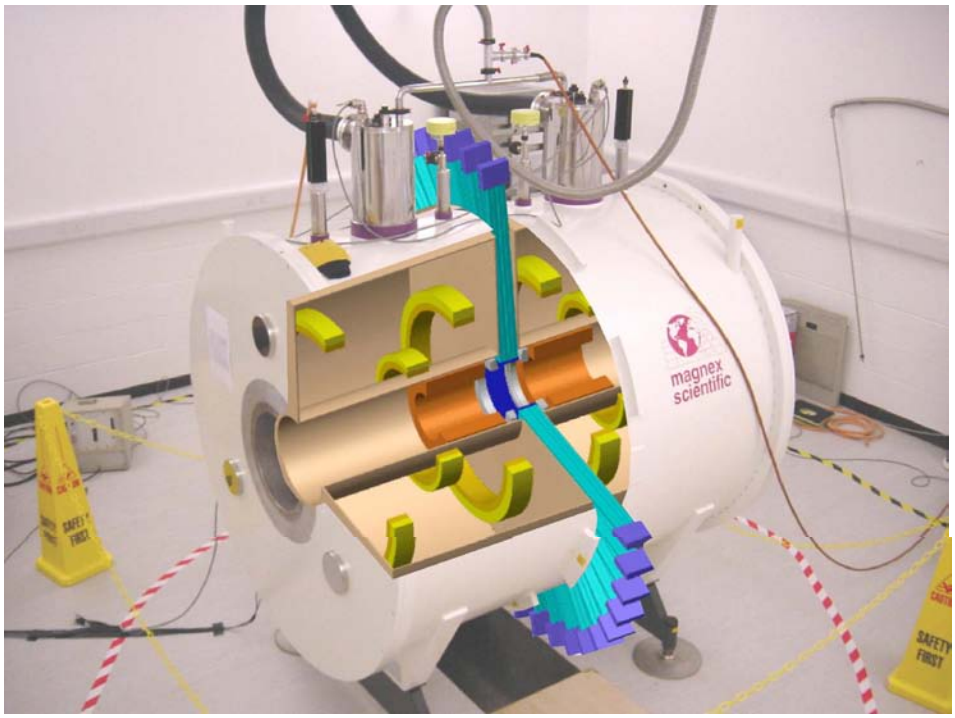

Figure 1-6. Schematic of the combined microPET-MR system in which bundles of fiber optic cables are used to direct the light from the crystals to the PMTs residing outside the magnetic field fringe of the MR system (Lucas et al., 2006). ©2006 IEEE.

A large number of solutions rely on the use of semi-conductor based detectors. There are two main classes of such detectors known as Avalanche Photo Diodes (APDs) and Silicon Photo Multipliers (SiPMs). The functionality of these detectors remains the same in the presence of magnetic fields. The use of APDs and SiPMs has facilitated the development of PET insert systems that can be put inside the MRI magnet bore obviating the need for fibre optics.

1.5.1 PET insert systems based on Avalanche Photodiodes (APDs)

APDs generate electrical signals when optical photons hit their silicon surface through a process known as avalanche multiplication. Incident photons generate photoelectrons in the thin silicon layer of the APD. These photoelectrons are accelerated towards opposite ends of the active region of the APD by the strong electric field creating electron-hole pairs in the process and leading to an avalanche. Avalanche multiplication occurs if the APD is receiving appropriate bias voltage to energize the electric field in the area between the semiconductors. When the bias

voltage supplied to the APD is slightly below a threshold level referred to as breakdown voltage, the device acts as a linear amplifier releasing electrical charge proportional to the number of detected photons (Holl, Lorenz, Natkaniez, Renked, & Schmelz, 1995; Shah, Farrell, Grazioso, Myers, & Cirignano, 2001).

The gain of APDs depends on the bias voltage and typically reaches a maximum value of 10^4. At this gain level, APDs cannot yet match the excellent gain characteristics of the PMTs whose current amplification is typically equal to 10^6 ("*Photomultiplier tubes, basics and applications"*, 2007). Amplification circuitry is required to make sure the signal is strong enough once it arrives at the data acquisition system. However, placing preamplifiers next to the detectors inside the MRI magnet is challenging, as they would lead to distortions in the RF field of the MRI system.

Different research teams that employ APDs in bimodal PET-MR systems have come up with workarounds to this problem. Catana et al (2006) present a hybrid PET-MR solution where the scintillators are connected to the APDs with fiber optics, but the length of the fiber optics used does not exceed 10 cm. The APDs and the electronics are placed inside the MR magnet bore, but far enough towards the outside so they are not inside the RF coil (Catana et al., 2006). Another APD-based PET insert system developed at the University of Tuebingen in Germany used light guides to directly couple the scintillators to the APDs, obviating the need to use fiber optics. A shielding box, with a thin layer of copper coating (< 10 um), was used around each detector in this system to protect the electronics against interference from the RF probe (Judenhofer, Siegel, Cherry, Claussen, & Pichler, 2007). Figure 1-7 shows a schematic as well as a detector module and the PET gantry for this system.

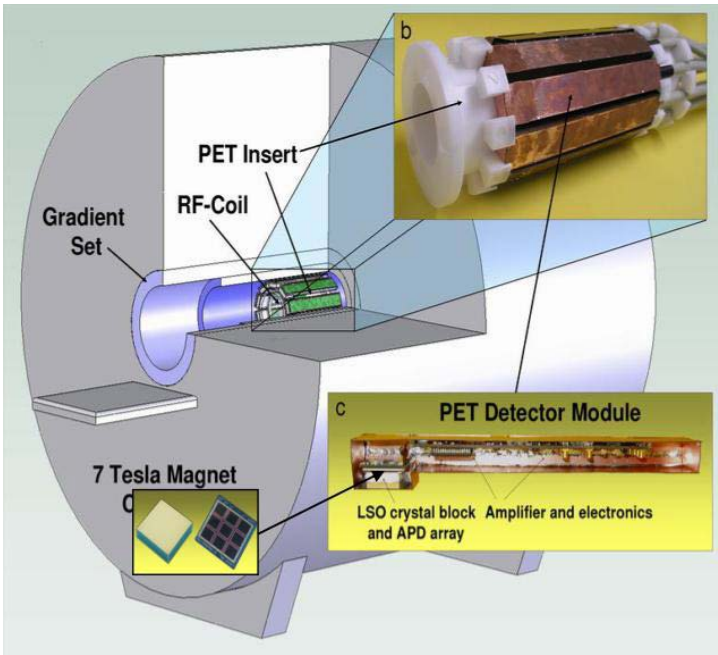

Figure 1-7. The APD-based PET insert system developed at the University of Tuebingen in Germany using light guides to direct the light to APDs (Judenhofer et al., 2008). Reprinted with permission from The Nature Publishing Group.

A group at Brookhaven National Laboratory (BNL) has reported successful acquisition of artefact free images with acceptable Signal to Noise Ratio (SNR) with a prototype PET insert system for breast imaging. The BNL Simultaneous PET-MR Dedicated Breast Scanner has been tested inside a 1.5T breast MR machine. The detector ring in this system has 24 APD-based detectors coupled to LYSO crystals. Figure 1-8 shows schematics of this system (Ravindranath et al., 2009).

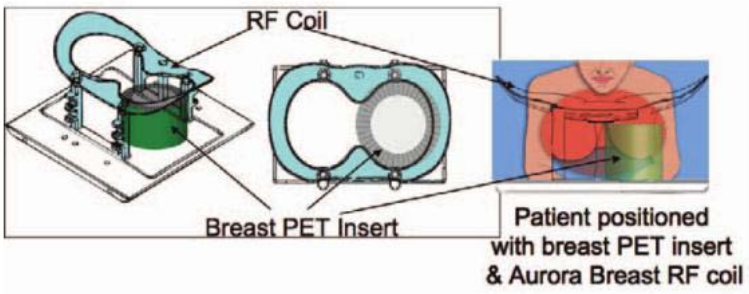

Figure 1-8. Schematics of the BNL PET-MR Dedicated Breast Scanner using APDs (Ravindranath et al., 2009). ©2009 IEEE.

1.5.2 PET insert systems based on Silicon Photomultipliers (SiPMs)

SiPMs exhibit superior characteristics when compared to APDs such as better gain and timing. They were first developed in Russia in the mid-1980s, but have attracted wide-spread attention in the last decade as they have matured as a technology. SiPMs have other intrinsic properties in addition to their insensitivity to magnetic fields that make them suitable for PET applications.

When APDs are biased with voltages above the breakdown voltage, their gain dramatically increases, matching the gain of conventional PMTs and obviating the need for preamplifiers. At these bias voltages, they are said to be operating in Geiger mode. A key feature of Geiger mode operation is that the output signal of the APDs will be independent of the number of photoelectrons. In Geiger mode, the APDs have a high-intensity electric field in the depletion region of the pn-junction which allows them to fire upon the initiation of an avalanche. APDs in Geiger mode act as binary devices signalling the presence of at least a single photoelectron and are called Geiger Mode Avalanche Photodiodes (G-APDs). Figure 1-9 shows the three regions of operation of APDs based on bias voltage.

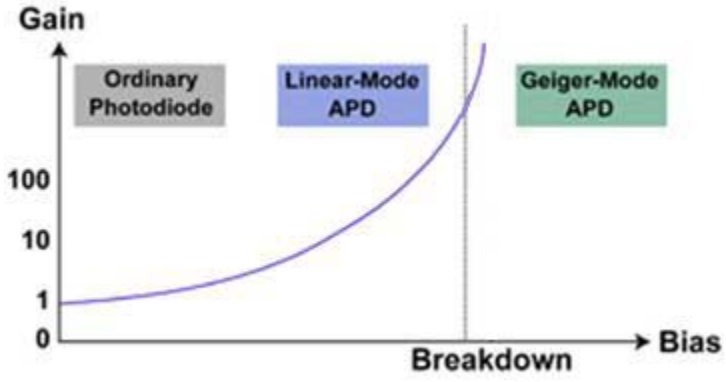

Figure 1-9. Different modes of operation of APDs based on bias voltage.

Silicon Photomultipliers (SiPMs) are matrices composed of units known as microcells. Each microcell is an APD which, when receiving a bias voltage above a certain threshold known as

the breakdown voltage, operates in Geiger mode. In a SiPM, these microcells are connected in parallel in groups known as pixels. Each pixel may contain thousands of microcells. The output of each pixel corresponds with the number of microcells that have fired in each pixel. The charge amplification ratio of SiPMs can reach up to 10^6 (Petasecca et al., 2008).

When the number of microcells in each pixel is greater than the number of optical photons, the output voltage of each pixel could be used to determine the number of optical photons. As the number of optical photons increases, a saturation effect in the response of the SiPM could be seen. A microcell that has just had an avalanche will not be able to fire before a certain amount of time has passed (Feege, 2008). Figure 1-10 demonstrates response saturation for SiPMs when the number of photoelectrons ($N_{ph.e.}$) increases. $N_{ph.e.}$ is proportional to the number of optical photons and is explained later in this chapter. The vertical axis in this graph shows the number of firing pixels.

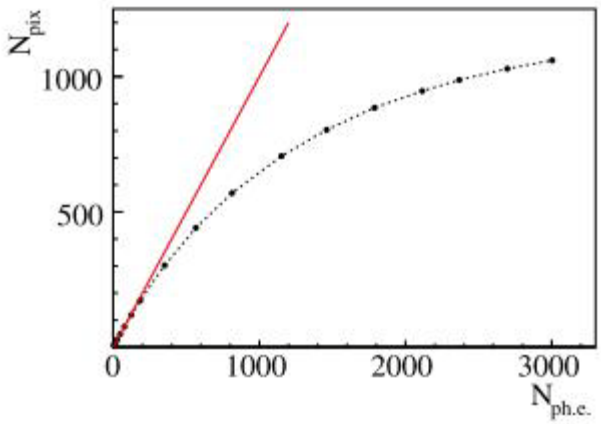

Figure 1-10. SiPM response curve showing saturation. As the number of photoelectrons (which is proportional to the number of optical photons) increases, the number of firing pixels displayed on the vertical axis reaches saturation at some point. The red line shows a line with a slope of 1 (Feege, 2008). Reprinted with permission from Nils Feege.

SiPMs enable the development of PET insert systems that can be used inside an MR magnet just as an APD-based PET insert system would function. The PET insert systems that have been reported in the literature follow the same design principles as the APD-based PET insert built by

Judenhofer et al (2007). A group in South Korea has built a SiPM-based PET insert system using the Hamamatsu Multiple Pixel Photon Counter (MPPC) S11064-050P. The detector ring in this system comprises 12 detectors around a gantry. The scintillator crystals are connected to the SiPMs by short optical fiber. The use of optical fiber in this system is intended to prevent any potential interference with the RF field around the object being imaged. Figure 1-11 shows a schematic of the detector ring in this system as well as a picture of the PET insert system as it is being inserted inside a Siemens 3T MR system (Hong et al., 2012).

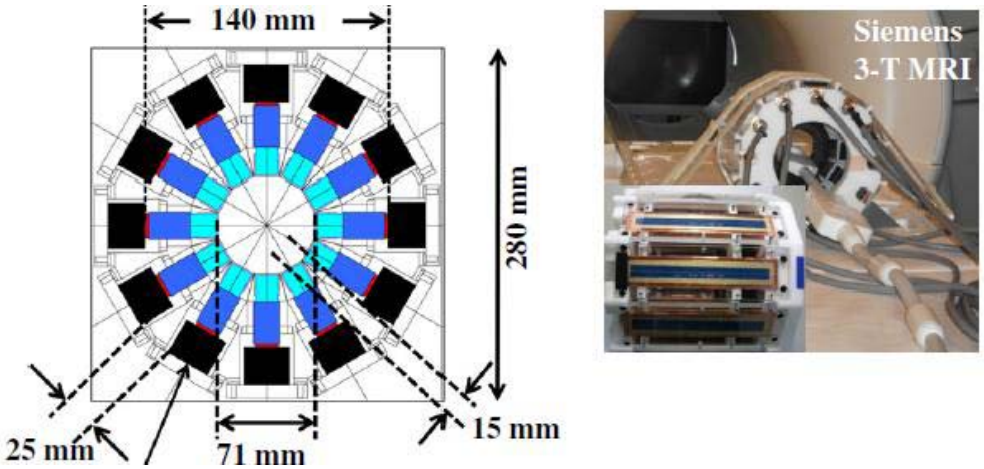

Figure 1-11. Schematic of gantry and picture of the PET insert developed by Hong et al (2012). Reprinted with permission from IOP Publishing.

1.6 Challenges in implementing a MR-compatible SiPM-based PET insert system

Sources of interference between the MR and PET systems have to be pinpointed and addressed for the PET-MR system to achieve acceptable performance. The use of SiPMs in a PET insert allows the PET detectors to work without interference from the MR system. However, there are other sources of interference between the two imaging modalities that preclude easy integration. For example, objects placed inside the magnet bore of a MR system have to be tested for magnetic susceptibility. Furthermore, PET detector electronics placed in the vicinity of detector elements might suffer from interference from the magnetic gradients of the MR system or its RF

field. Some of the most pressing challenges of integrating a PET insert inside a MR system can be summarized as follows.

1.6.1 Homogeneity of the MR main magnetic field

In order for the MRI to maintain optimal image resolution, it is important that the main magnetic field remain homogeneous in the presence of PET components. A heterogeneous MRI main magnetic field leads to distorted images. All components of the PET insert system must be evaluated for their magnetic susceptibility (Wehrl et al., 2009).

1.6.2 Uniformity of the MR RF field

The uniformity of the RF field is of paramount importance to obtaining a clear image from MRI. Any conductive material placed between the RF coil and the object could lead to heterogeneities in the RF field and thus degradation and distortions in the image. The approach in the development of PET insert systems has been to place the RF coil between the PET detector ring and the object to minimize distortions in the RF field. Distortions resulting from the conductive materials in the PET gantry outside of the RF coil still lead to degradation in final image quality, but their effect is not nearly as deleterious as if they had been between the RF coil and the object. Proper tuning of the RF coil can help alleviate some of the detuning that results from the presence of the PET components (Wehrl et al., 2009).

1.6.3 Eddy currents in components of the PET system

Eddy currents can cause electric potentials that can lead to distortions in both MRI and PET images. Eddy currents are caused by the fast switching of the MRI magnetic field. They can occur in any conductive material including the shielding, electronics, the APDs, or the SiPMs in the PET insert system. Eddy currents can also occur in conductive material as a result of the RF

field. Such eddy currents pose the risk of heating in the material. They may also lead to image artefacts in the MRI scans (Strul et al., 2003).

The risk of eddy currents being induced is higher if larger conductive materials are present or if fast imaging sequences are being used. Conductors can also affect the quality factor by altering the coil resonance frequency resulting in degradation of image quality. If the change in frequency exceeds the tuning capabilities of the coil, proper tuning may no longer be possible.

1.6.4 PET attenuation correction

A mechanism of correcting for photon energy attenuation is needed to achieve quantitatively accurate PET images. The number of incident photons is reduced as a result of interaction with body matter. Furthermore, some photons are scattered outside of the field of view of PET detectors. In the case of PET/CT, attenuation information is obtained from CT images; However, MRI does not directly provide information on the attenuation properties of materials in the field of view. Several approaches have been proposed to obtain PET attenuation maps such as using a normalized atlas or template. Attenuation correction methods solely based on PET have also been used such as image-processing algorithms to find edges and boundaries in the image (Lee & Kang, 2008).

1.6.5 Temperature drifts

Another source of interference between the PET and MRI systems is drifts in temperature that can be caused by changes in temperature in the PET electronics or by eddy currents in the PET system. These temperature drifts can lead to quality degradation in both PET and MRI images. In case temporal imaging techniques such as fMRI are used, temperature drifts can cause gradual increase of noise in the MRI or PET signals and lead to loss of quality as the imaging sequence progresses.

1.6.6 Properties of SiPMs

1.6.6.1 Dark Current

Besides incident light, thermal excitation also can cause the release of electrons from microcells leading to a false signal and the release of a leakage current known as dark current. The number of thermally activated microcells per second is defined as the dark current rate in SiPMs and is reported as a measure of noise. Dark current rate is also affected by the sensitive surface area of the SiPM (larger surface area leads to a higher dark rate) and its bias voltage (Vandenbroucke, McLaughlin, & Levin, 2012).

1.6.6.2 Gain

The gain of a SiPM is defined as the electric charge that is created when a single photoelectron is created in a microcell in the SiPM. The gain of the SiPM is one of the factors that determine the amplitude of the response of the SiPM as shown in Equation 1-1. In this equation, $N_{ph.e.}$ represents the number of photoelectrons generated in the crystal, G is the gain of the SiPM and A is the amplitude of the response of the SiPM.

$$\boldsymbol{A \sim N_{ph.e.} . G} \quad \text{Equation 1-1}$$

Microcells in SiPMs operate in Geiger mode with large gain values only when biased above the breakdown voltage. As the bias voltage exceeds the breakdown value, the gain quickly increases. The SiPM gain in Geiger mode has a linear relationship with bias voltage (Marrocchesi et al., 2009). Figure 1-12 demonstrates the relationship between gain and bias voltage of a Hamamtsu SiPM in Geiger mode from a study in 2009.

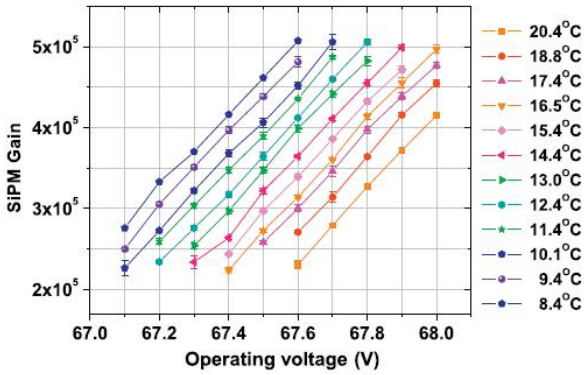

Figure 1-12. SiPM gain as a function of bias voltage at different temperatures (Marrocchesi et al., 2009). Reprinted with permission from Elsevier.

In order to measure the breakdown voltage of the SiPM, leakage current out of the SiPM is measured for different bias voltages while the SiPM is kept in a light tight environment and at a fixed temperature. When the bias voltage is below the breakdown voltage, the current is constant and its value depends on the readout circuits. For voltages above the breakdown value, the current is dependent on the rate of dark current as well as correlated avalanches caused by cross talk between adjacent cells in the SiPM matrix, as depicted in Equation 1-2. Because correlated avalanches can themselves lead to subsequent correlated avalanches, they follow a Borel distribution and their expected value is equal to the middle term in Equation 1-2 (Vinogradov, 2012). The three terms in Equation 1-2 depend on overvoltage as detailed in Equations 1-3 through 1-5. Substituting these into Equation 1-2 yields the relationship between current and voltage shown in Equation 1-6. A curve fitting function can be created to find the value of the breakdown voltage based on the data points of the I-V curve (Amaudruz et al., 2014). Figure 1-13 shows I-V curve of a SiPM recorded at different temperatures without any external light.

$$\boldsymbol{I = (Dark\ Current\ Rate)\left(\frac{1}{1-average\ number\ of\ correlated\ avalanches}\right).Gain} \qquad \textbf{Equation 1-2}$$

$$\boldsymbol{Dark\ Current\ Rate = D.(V_{bias} - V_{breakdown})} \qquad \textbf{Equation 1-3}$$

where D is a temperature-dependent parameter

$$\boldsymbol{Gain = C.(V_{bias} - V_{breakdown})} \qquad \textbf{Equation 1-4}$$

where C is the capacitance of a microcell

$$\textbf{average number of correlated avalanches} = N_{ca}.(V_{bias} - V_{breakdown})^2$$ **Equation 1-5**

where N_{ca} is a temperature-dependent parameter

$$\begin{cases} I = DC\left(\frac{1}{1 - N_{ca}.(V_{bias} - V_{breakdown})^2}\right)(V_{bias} - V_{breakdown})^2 + \beta & (\text{when Vbias} > Vbreakdow) \\ I = \beta & (\text{when Vbias} < Vbreakdown) \end{cases}$$

Equation 1-6

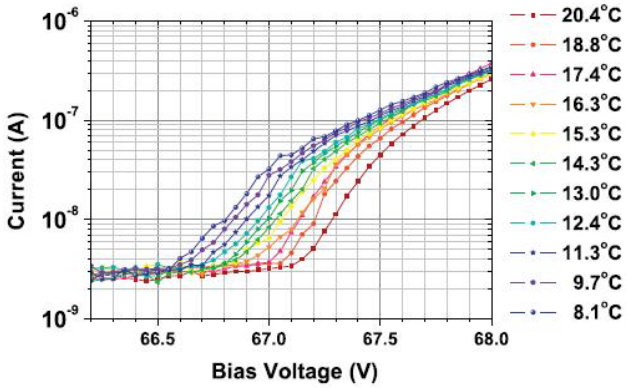

Figure 1-13. Current versus bias voltage of a Hamamatsu Multipixel Photon Counter. (Marrocchesi et al., 2009). Reprinted with permission from Elsevier.

The breakdown voltage of SiPMs changes linearly with temperature (Petasecca et al., 2008). As the temperature rises, a higher bias voltage is required to ensure that the SiPMs microcells are operating in Geiger mode. The difference between the bias voltage of the SiPM and its breakdown voltage is defined as the overvoltage (OV). Figure 1-14 plots the changes in breakdown voltage with temperature for two different types of SiPMs. In order to achieve the same gain level with increasing temperature, the bias voltage has to increase so that OV stays the same (Marrocchesi et al., 2009; Petasecca et al., 2008; Ramilli, 2008). Figure 1-15 show plots of gain versus OV for different types of SiPMs in two different studies.

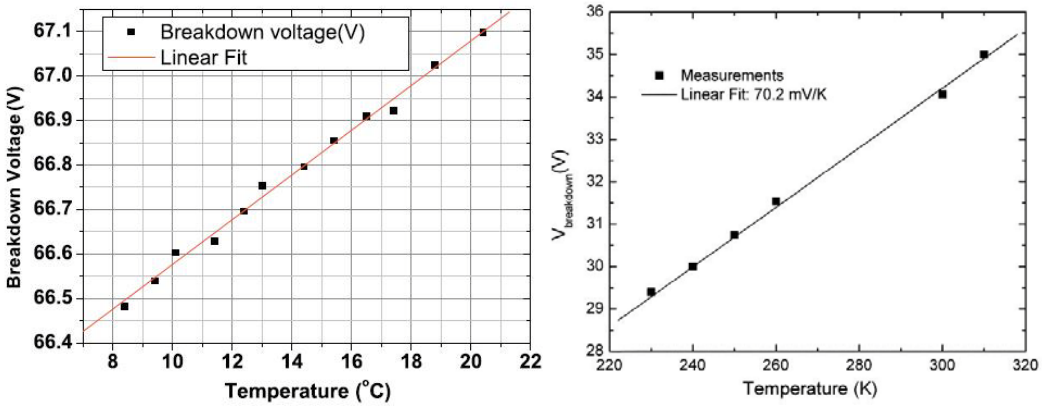

Figure 1-14. Changes in breakdown voltage with temperature for a Hamamatsu MPPC-S10362-33-050C SiPM (left) (Marrocchesi et al., 2009) and a SiPM manufactured by FBK-irst (right) (Petasecca et al., 2008). ©2008 IEEE.

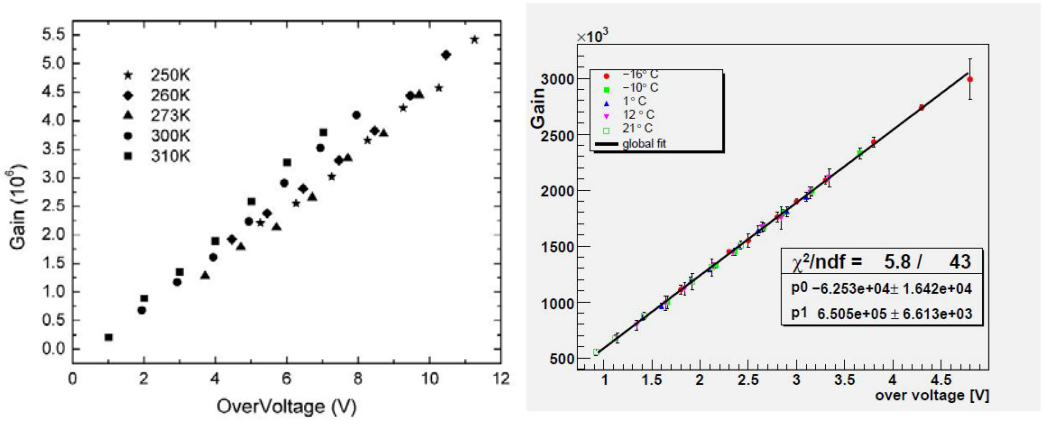

Figure 1-15. Changes in gain with OV for two different types of SiPMs; left: a SiPM manufactured by FBK-irst. Right: a SiPM manufactured by SensL (Petasecca et al., 2008) (Ramilli, 2008). ©2008 IEEE.

1.6.6.3 Photon Detection Efficiency (PDE)

Besides gain, which determines the magnitude of the response from a single microcell, the response amplitude of a SiPM also depends on the number of photoelectrons generated. The number of photoelectrons depends on two key characteristics: the photon detection efficiency (PDE) of the matrix and its optical interpixel crosstalk. The former is a product of $PDE_{geo,}$ the geometric photon detection efficiency, which depends on the sensitive area, PDE_{qua}, the quantum photon detection efficiency, which describes the probability of the absorption of a photon in the depletion region of the microcell and PDE_{Geiger}, the Geiger photon detection efficiency, which is the probability for an electron/hole pair to generate electric discharge from the microcell.

Interpixel crosstalk is a measure of how likely it is for an avalanche in one microcell to lead to a spontaneous avalanche in a neighboring microcell not hit by an optical photon. Higher temperatures degrade the PDE and increase optical cross talk in the SiPM. Equation 1-7 describes how $N_{ph.e.}$ is related to the number of optical photons ($N_{optical}$). In this equation, PDE is represented by ε and k is the interpixel crosstalk.

$$N_{ph.e.} = N_{optical}.\varepsilon.(1+k) \qquad \text{Equation 1-7}$$

1.6.6.4 Saturation Properties

Equation 1-7 is a simplistic model of the operation of a SiPM, because it assumes that a photoelectron will cause a cell to fire only once. In other words, this equation assumes that the number of firing pixels is equal to the number of photoelectrons created. This assumption is not realistic as the recovery time of a microcell is not infinite. A microcell may fire more than once in response to optical photons of the same scintillation event because its recovery time has elapsed, or it may not fire at all because it has saturated. The effective number of microcells (denoted by N_{eff}) depends on microcell recovery time and illumination properties of the incident light. Some microcells may not fire at all, or they might recover and fire more than once. Furthermore, the pulse width of incident light might not be sufficient to illuminate the entire surface of the SiPM. N_{eff} could therefore be more or less than the total physical number of microcells in the matrix. The relationship between the total number of firing microcells and the number of photoelectrons created is given by Equation 1-8 (Kaplan, 2009).

$$\boldsymbol{N_{firing} = N_{eff}.(1 - e^{-\frac{Nph.e.}{N_{eff}}})} \qquad \text{Equation 1-8}$$

1.6.7 Correction of SiPM temperature dependencies

Researchers working on building calorimeters, which are devices used to measure the energy of charged particles in high energy physics experiments such as the Large Hadron Collider, have done significant work on correcting for SiPM temperature dependencies. It is important for calorimeters using SiPMs to extrapolate the number of optical photons from the signal amplitude assuming known SiPM properties such as gain and PDE. The system has to have a means of accounting for the change in SiPM properties with changes in temperature. A simple solution is to introduce a linear correction mechanism to calculate the change in signal amplitude or gain as the temperature changes. Frequent temperature measurements are necessary in this approach to ensure accuracy (Kaplan, 2009).

If the particular application in which the SiPMs are used permits it, it is also possible to re-determine the parameters with changes in temperature (Feege, 2008; Kaplan, 2009). In the case of calorimeters, such calculations are possible but time-consuming. For a PET insert system, it is not possible to determine the gain, PDE or dark rate while the system is in operation.

Instead of frequently re-determining the parameters, it is easier to have a means of calculating the parameters based on temperature and voltage values. This approach uses prior measurements of temperature and voltage dependencies of SiPMs and relies on frequent measurements of temperature and voltage during operation. The parameters are indirectly determined in this method and are prone to measurement errors and temporal changes in SiPM properties (Feege, 2008).

When it comes to temperature dependence of SiPM properties, the aim in a PET insert system is to ensure that the parameters (e.g. gain, PDE and dark rate) stay constant with respect to a reference operational condition. Unlike a calorimeter, the objective in a PET system is to locate

annihilation events by detecting optical photons on a pixel on the SiPM. A direct determination of SiPM properties is therefore not necessary in the case of PET systems. It is rather more important to ensure that the SiPM properties remain constant with changes in temperature.

One approach to keep these parameters constant is to make changes to bias voltage as the temperature changes, since the SiPM properties depend on bias voltage as well as temperature. In this approach, temperature correction is equivalent to a simple linear feedback control system, where frequent measurements of temperature are taken and a new bias voltage is applied to the SiPM to ensure stability of parameters. The bias voltage values are based on previous bench top measurements where SiPM parameters are evaluated at different temperature points.

Feedback loop control systems that rely on bias voltage as a tool to stabilize the gain of SiPMs have been implemented for different applications including PET systems. A research group in Italy has reported a gain stabilization of within ±1% across a temperature range of 10 degrees Celsius with Hamamatsu MPPC-S10362-33-050C SiPMs (Marrocchesi et al., 2009). Another study concerning SiPM-based Chernekov telescopes has reported gain stabilization to within 5%. In this study, instead of using a lookup table that would be populated with previous benchtop measurements, an active monitoring system is employed to calculate the bias voltage based on the output of the SiPM (Anderhub et al., 2011). Both of these studies have benefitted from the ability to determine the SiPM gain directly.

Instead of feedback control systems that operate by adjusting the bias voltage, a feed-forward control system can be used to adjust the amplification factor of the SiPM output based on temperature. Prior measurements of energy photopeak at different temperatures are required to come up with a compensation factor that is fed into the amplifiers preparing the signal for use in

the data acquisition system (Seiichi Yamamoto et al., 2011). Figure 1-16 depicts the schematics of the system constructed by Yamamoto et al. Their system is reported to have succeeded in decreasing the change in count rate from 10% to within 3.7% with a 1.5°C change in temperature.

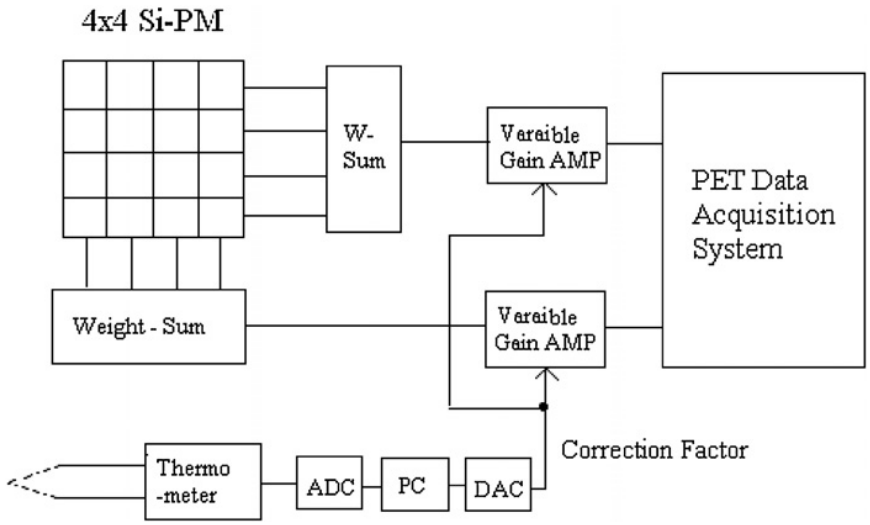

Figure 1-16. A feed-forward control system for temperature correction of SiPM operation in a PET insert system (Seiichi Yamamoto et al., 2011). Reprinted with permission from IOP Publishing.

1.7 The need for a slow control system

When using SiPM's for PET imaging, special attention has to be devoted to the changes in their breakdown voltage with changes in temperature. Changes in breakdown voltage affect the gain and the PDE of the device. Inside the MR magnet eddy currents could cause local changes in temperature. A system has to be devised to monitor temperature changes in the PET system and apply thermal control to keep the temperature from deviating outside of the acceptable range. Adjustment to the bias voltage might be necessary to ensure the gain and PDE of the detectors remain within predefined constraints. Furthermore, calibration and testing of the detectors is necessary for their operation in the temperature range inside the MR magnet.

Chapter 2

Data collection and analysis methods

2.1 Overview

This chapter describes the components and setup used to acquire data from detectors in the PET insert system on the bench top. All experiments in this thesis project used this setup to acquire and analyze data. It is envisioned that parts of the present setup will be replaced by the OpenPET system as it becomes available.

Figure 2-1 shows an overview of the data acquisition process. On the detector module, the output of SiPMs is multiplexed from 32 down to 4 channels. Differential amplifiers in the detector module convert the raw single-ended signals into differential signals for better noise tolerance. The detector module is equipped with a temperature sensor as well. The output signals as well as the temperature signal are carried through HDMI cables to a detector interface board (DIB). The differential signals are converted to single-ended signals on the DIB. Details on the DIBs and the electronic components used can be found in Section 2.3. The current version of the DIB provides both the 68-pin OpenPET-compatible output for these signals as well as SMA connectors to enable data acquisition without the OpenPET readout electronics. The bias voltage supplied to each detector is controlled by a software program running on the onboard computer on the DIB through a Digital to Analog Controller (DAC). Power to differential amplifiers in each detector is supplied by voltage regulators on the DIB which produce +2.8V and -2.8V. Signals are routed to the data acquisition electronics cabinet where a series of electronic components generates the trigger and samples the signals. A digital data acquisition card digitizes the samples and stores them on the data acquisition PC connected to the electronics cabinet.

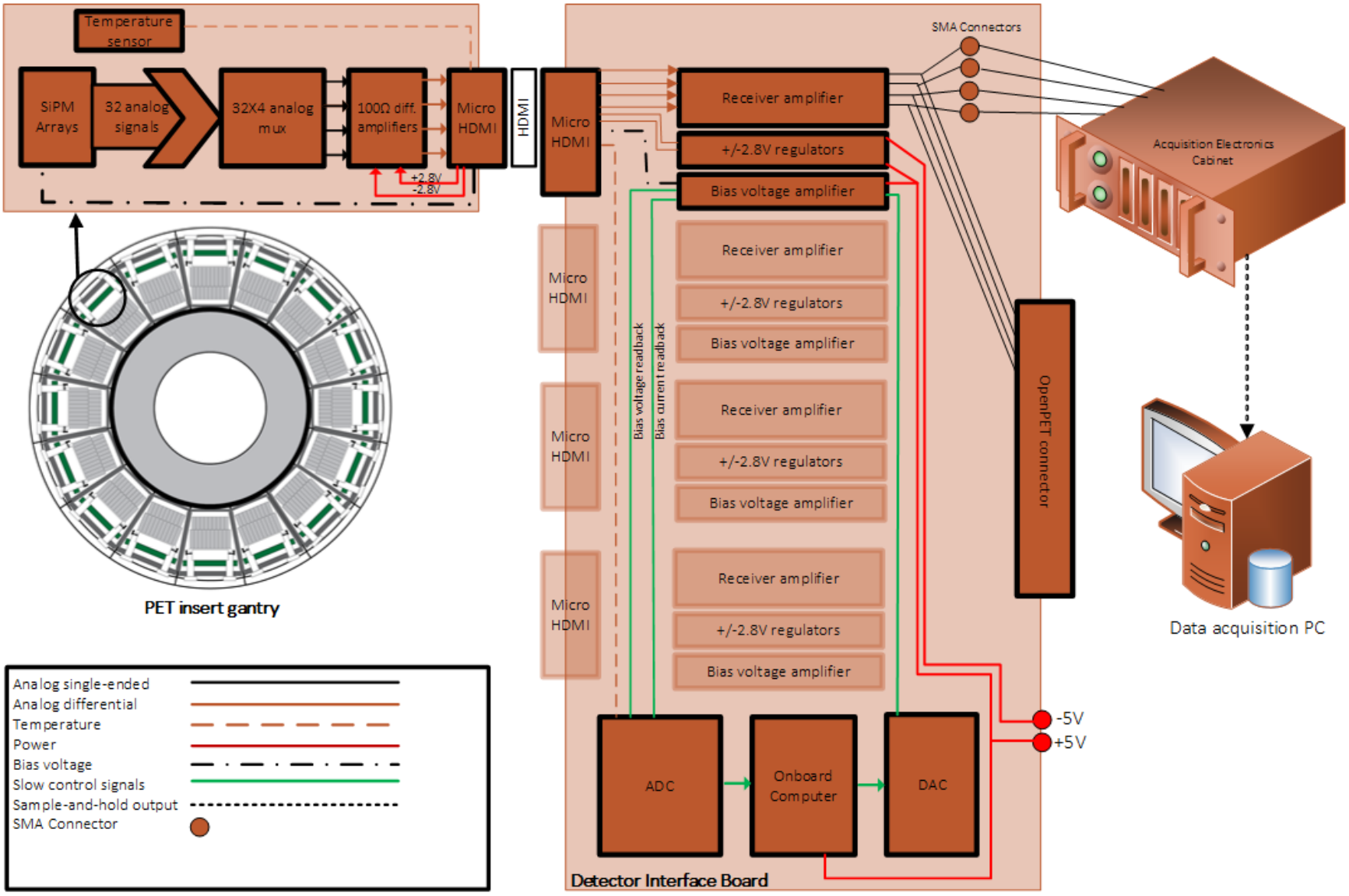

Figure 2-1. An overview of how data is acquired from a detector module and is subsequently sampled and digitized.

2.2 The detector module

Each detector module used in the PET insert system comprises two SensL 16-pixel ArraySB-4 SiPM arrays coupled to dual layer offset Cerium-doped Lutetium Yttrium Orthosilicate (LYSO) crystal arrays. The crystal array comprises 409 crystals organized into two layers (22×10 crystals in the bottom layer and 21×9 in the top layer). The dimensions are 1.2×1.2×4 (top) / 6 (bottom) mm^3. The SiPM and crystal arrays are placed on a board referred to as the transmitter board. The transmitter board multiplexes the outputs of the SiPM arrays from 32 channels for the two SiPMs down to 4 channels by using a network of resistors[1]. The amplifiers on the transmitter board convert the output signals to differential signals for better noise tolerance. Figure 2-2 shows the schematic of a PET detector module in the PET insert system.

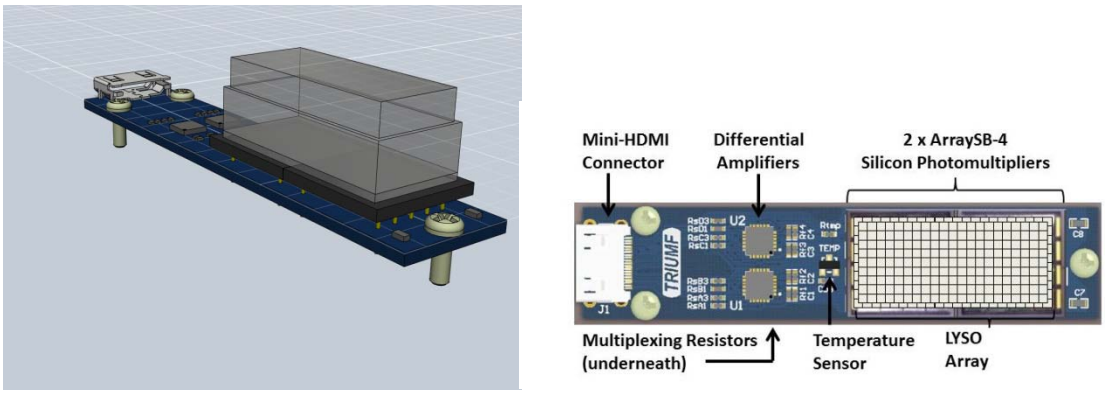

Figure 2-2. The detector module comprising the transmitter board, the SiPMs and the dual layer LYSO crystal (right) is shown next to the schematics of the transmitter board (left).

The signals from each detector module are carried to the PET system acquisition electronics cabinet by HDMI cables. These HDMI cables also provide signal lines for bias voltage for the SiPMs, low voltage power for amplifiers on the transmitter boards, and the voltage signal from a temperature sensor on each transmitter board (Goertzen et al., 2012). Figure 2-3 shows the PET insert with some of the detectors assembled. The position of HDMI cables in the gantry can be seen in this image.

[1] The theory behind the resistive network and how multiplexing is achieved in described in detail in Chapter 3.

The output signal of the detector modules in the PET insert system is dependent on characteristics of the scintillating crystals and the SiPMs. In experiments described in chapter 3, these characteristics have been studied to obtain an understanding of how the detector modules would behave at different temperatures and bias voltage values.

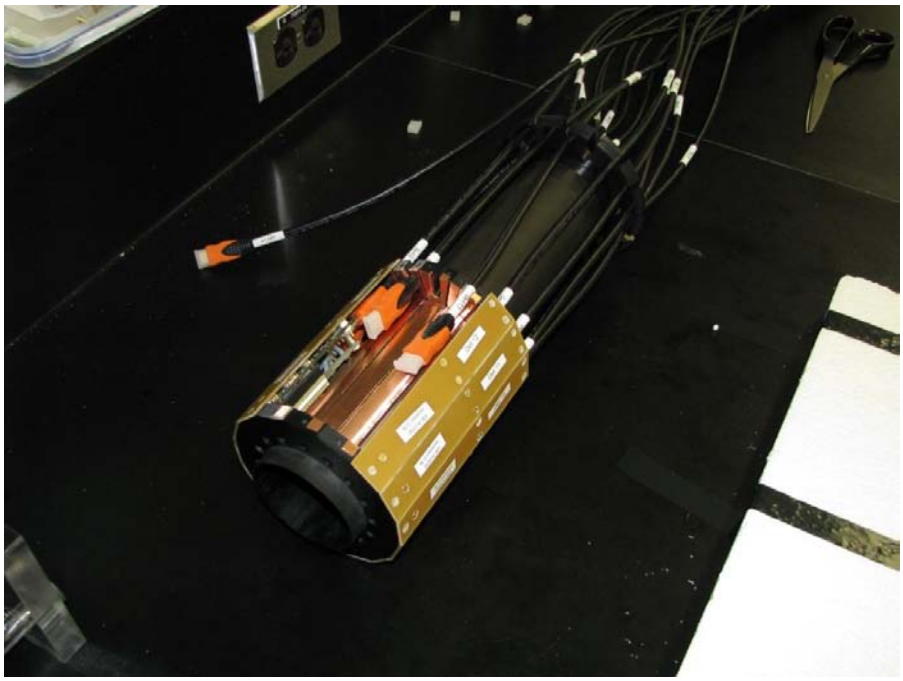

Figure 2-3. The PET insert system with some of the detectors assembled. The HDMI cables can be seen extending from the detector modules.

2.3 The Detector Interface Board (DIB) and signal conditioning

The detector interface board (DIB) is an intermediary component between the detector modules and the readout electronics. It provides the detector modules with bias voltage for the SiPMs and low voltage power for the onboard amplifiers. It also receives four pairs of differential output signals from each detector module as well as the temperature readback signal. The DIB includes firmware and electronics to enable monitoring of bias voltage, current and temperature for each detector module connected to it.

In the current version, each DIB is connected to four detector modules. The signals are received from the detector modules as 100Ω differential signals. The DIB converts the signals to 50Ω single-ended signals. Each DIB provides a 16-channel output through either a 68-pin connector (intended for compatibility with the OpenPET system) or 16 coaxial SubMiniature version A (SMA) outputs intended for use in tests on the bench top (Shams et al., 2013).

The DIB can act as part of a slow control system if it is equipped with the necessary control software. To this end, a Raspberry Pi® computer is connected to each DIB in the current version by a pinpad connector and sits at a distance of 1.5cm parallel to the DIB. Through its General Purpose Input-Output (GPIO) pins, the Raspberry Pi® computer is connected to the key electronic components on the board so that it can control and monitor the operating parameters of the PET detectors. Figure 2-4 shows an image of the DIB with the Raspberry Pi® computer attached to it.

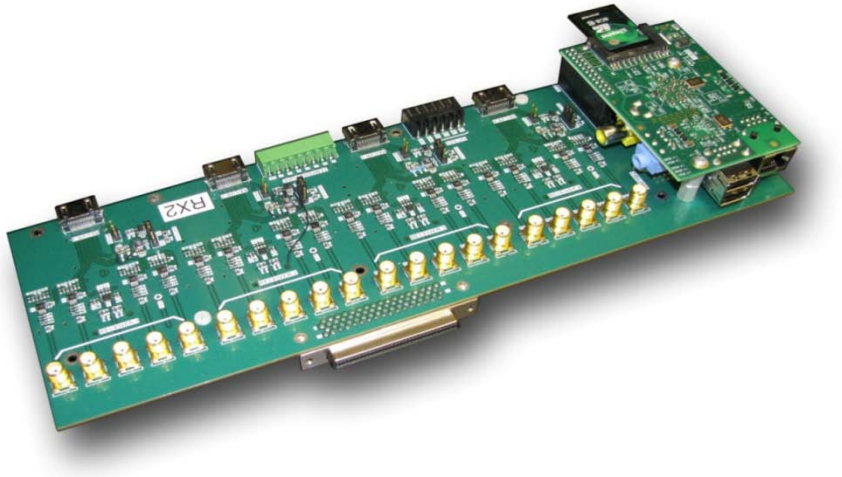

Figure 2-4. The current version of the DIB with the Raspberry Pi® computer attached.

The DIB includes a set of amplifiers, an Analog to Digital Converter (ADC), a Digital to Analog Converter (DAC), voltage regulators to provide bias voltage for the amplifiers on the detector modules, operational amplifiers to provide the bias voltage to the SiPM sensors in the detector

modules, and a 68-pin VHDCI port for connection to the OpenPET system. Figure 2-5 presents a functional diagram of the current version of the DIB and shows the interconnections of the components. The following list provides more details on these components.

1. Four differential receiver amplifiers (Analog Devices AD8130): Four sets of analog differential signals are received from each detector module via the HDMI cables. These signals are received as 100Ω differential signals and are converted to 50Ω single-ended signals by the differential receiver amplifiers to match the input requirements of the data acquisition system. There is one such amplifier on the DIB for each detector module connection.
2. Analog to Digital Converter (ADC) (Linear Technologies LTC2499UHF): The ADC is used to monitor the bias voltage supplied to each detector module, the electrical current the detector is drawing, and the temperature of each detector module. The ADC module can convert one analog input channel at a time with a conversion time of 85ms. The 12 input channels (bias voltage, current and temperature for each detector) can thus be digitized in sequence in 1.02s. The ADC is accessed via the I^2C bus by the Raspberry Pi® computer.
3. Four op-amps (Texas Instruments OPA237NA/250): The bias voltage supplied to each detector is provided by one of these op-amps. This particular op-amp was chosen because of its low offset voltage (750μV maximum), low bias current (8.5nA), and small size. Also, the output range of this op-amp is between 2.7V to 36V which makes it ideal to provide the range of bias voltages needed for the SiPMs.
4. Digital to Analog Converter (DAC) (Linear Technologies LTC2619CGN): The exact amount of bias voltage for each detector is controlled by the DAC which is connected to

the op-amp. Four output channels of the DAC are connected to the four op-amps that provide bias voltage to the four detectors connected to the DIB. The DAC is also connected to the Raspberry Pi® via the I^2C bus to provide control over the exact amount of bias voltage supplied to each detector.

The design of the DIB printed circuit board was conducted in the Altium® software package. The schematics of the functional diagram depicted in Figure 2-5 was drawn. The schematic was then compiled into PCB view through the use of device libraries. The final step involved routing the circuit and troubleshooting.

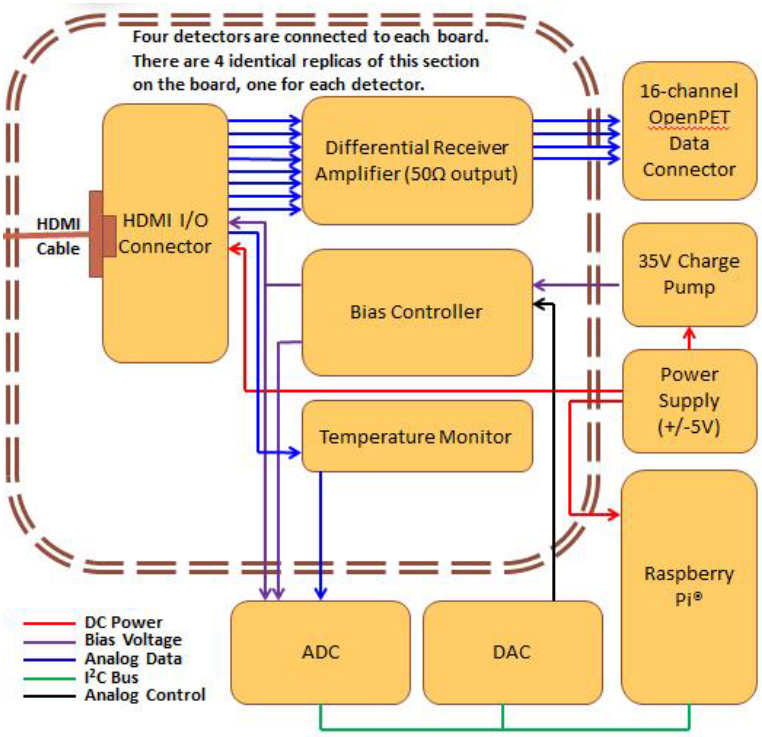

Figure 2-5. Functional diagram of the current version of the DIB.

The Raspberry Pi® was selected as a simple means of onboard control for the DIB. The Raspberry Pi® is a single-board computer developed by the Raspberry Pi® Foundation. It has an ARM processor and relies on an SD Card for booting the OS and persistent storage. The operating system provided for use on the Raspberry Pi® is a variant of Debian Linux with tools

for programming in Python. The Raspberry Pi® enjoys a wide developer community providing support in numerous forums online. It is extensively used in both educational and industrial applications.

A control program was developed on the Raspberry Pi® computer to manage the operations of the DIB as well as report to and receive control commands from a central control server managing all DIBs in the system. The on-board DIB control software has the necessary means at its disposal to adjust operating voltage, and monitor the temperature and current of the PET detectors. The central control server enables visual reports to be presented to a human operator as well as system-level control of the operation of the detectors.

An understanding of the temperature dependencies of the operation of PET detectors was needed for the implementation of this control system. The next chapter presents the results of a study performed as part of this thesis project to model the behavior of the PET detectors with the change in their operating parameters such as temperature. The results from this study were subsequently used in the implementation of the slow control software.

2.4 Signal sampling and digitization

The HDMI cable carries the 4 detector output signals to the DIB. After conversion to single-ended signals, these outputs are accessible through either the SMA connectors or the 68-pin connector on the DIB. The 68-pin output will be used by the OpenPET system. All signal acquisition in experiments described in this thesis is performed with signals taken from the SMA outputs.

The four SMA outputs are connected to the components in the data acquisition electronics cabinet for signal acquisition and sampling in the lab. The four signals are first connected to a

Phillips Scientific NIM Model 778 variable gain preamplifier. This module is used to split each signal into two identical signals, one of which is used to generate the trigger. One output from each Model 778 channel is connected to one of the channels of a Phillips Scientific NIM Model 740 linear logic fan in/out. The sum output of this channel is connected to one of the channels of a Phillips Scientific NIM Model 715 Constant Fraction Timing Discriminator (CFD) to generate the threshold for the trigger signal. The trigger is generated by using the output from the CFD as the input to one of the channels of a Phillips Scientific NIM Model 794 Gate/Delay generator. The trigger signal is used to trigger a sample-and-hold device which produces a signal with the same amplitude as its inputs at each trigger and hold the same amplitude until the next trigger. The four signals from NIM 778 are connected to a shaping amplifier (Mesytec MSCF-16) prior to being connected to the custom eight-channel sample-and-hold. The output of the sample-and-hold is connected to a National Instruments PCI-6143 data acquisition card mounted in a PC running Microsoft Windows for digitization and storage on the computer by the data acquisition software program developed in the Labwindows/CVI® environment.

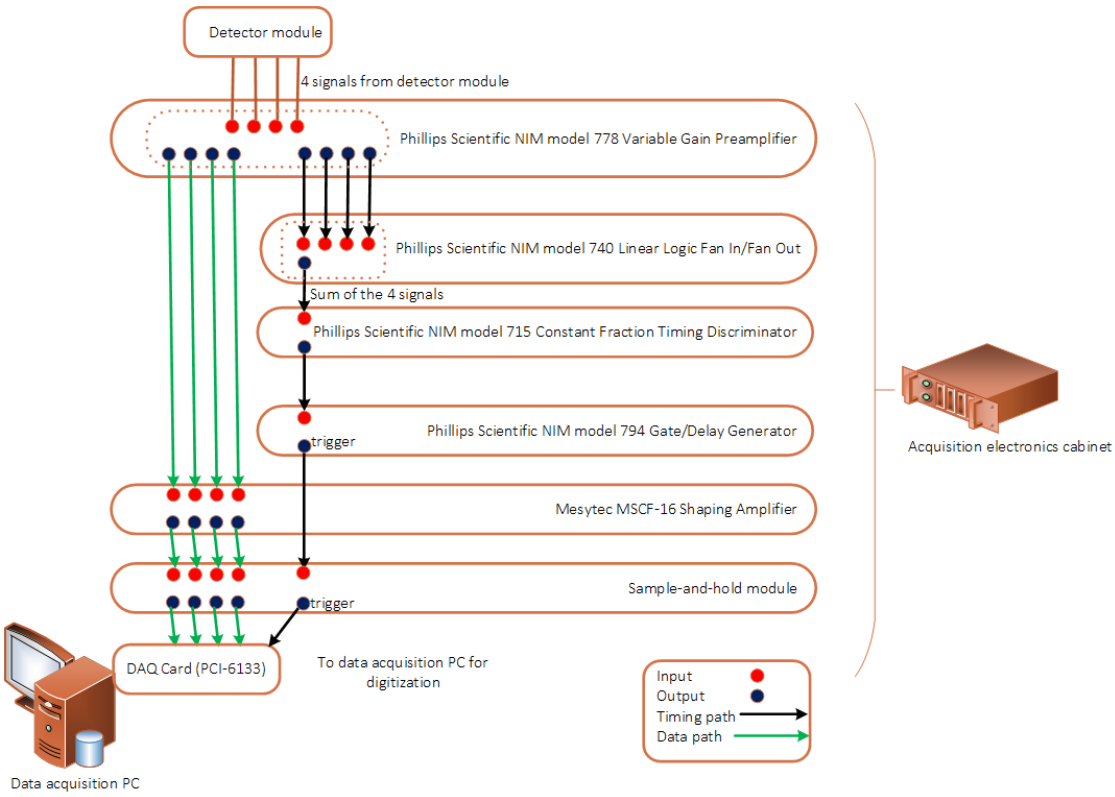

Figure 2-6. Modules and interconnections in the electronics cabinet.

2.5 Data analysis

Accurate identification of 511keV gamma rays is vital to the operation of a PET system. The 32 signals from the two SiPMs on each detector module of the PET insert system are multiplexed down to 4 signals by using a resistive charge division network. The result is four signals representing the four corners of the rectangle encompassing the SiPMs. The sum of these four signals is proportional to the energy of the event that triggered the signal. The PET system uses these signals (known as A,B,C and D) to decide which signals represent an annihilation event.

After the A,B,C and D signals from the four corners of the resistive network in a detector module of the PET insert system are sampled and digitized, the results are saved in a comma-separated text file with each line containing the four values from a triggered event. This is known as the

raw data file which comprises sampled voltage values reported by the ADC. Figure 2-7 shows a sample of a raw data file.

The sum of the voltage values for each event corresponds to the energy of the incident photon. The four voltage values are also used to infer the location where the incident photon has hit the crystal block. This method of inference, referred to Anger logic, is described in a landmark paper from 1958 by Hal O. Anger and gives the X,Y location of the incidence crystal based on the A,B,C and D values as depicted in Figure 2-8 (Anger, 1958).

```
0.607147,1.142426,0.743103,0.486908,
1.802521,0.303192,0.180969,0.862885,
0.499573,0.549316,0.808716,0.852051,
1.105804,0.480042,0.327454,0.791779,
0.119629,0.960693,1.510162,0.200958,
0.999298,0.240479,0.279846,1.349182,
0.234528,0.890198,1.292572,0.372620,
0.436859,0.290833,0.541534,1.124268,
0.332336,1.196442,0.965271,0.329437,
1.215973,0.507050,0.457458,1.162262,
1.742859,0.778961,0.463715,0.991364,
1.417236,0.190735,0.192261,1.651611,
1.299438,0.260925,0.156403,0.636292,
0.546265,1.174927,0.580139,0.362701,
0.249329,1.437225,1.007996,0.252838,
0.178528,1.441956,0.842590,0.175629,
1.116180,0.325165,0.343170,1.389313,
0.059357,1.610565,1.104279,0.066833,
0.956268,0.236816,0.272064,1.357117,
0.487976,0.251312,0.438080,1.342926,
```

Figure 2-7. A sample of the contents of the raw data file which contains the four signals coming from the corners of the resistive sheet in the detector module.

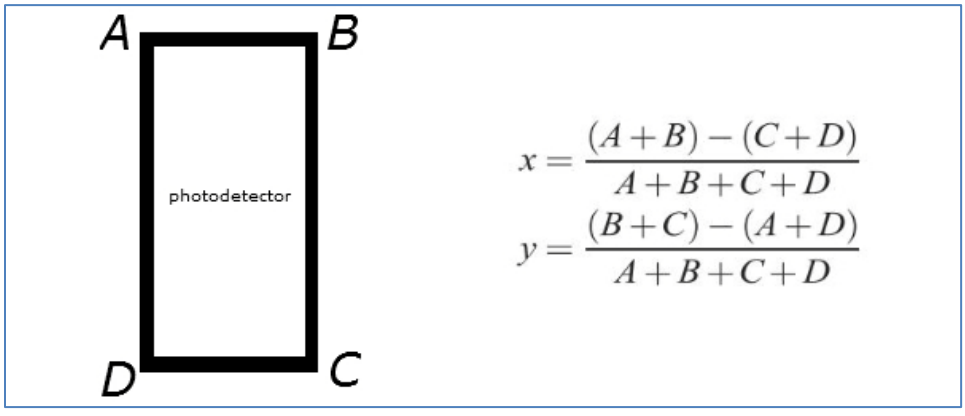

Figure 2-8. The x,y coordinates of the scintillation events are calculated based on the value of the signals from the corners of the resistive sheet in the detector module.

To infer location data from the raw data file as described above, the file is fed into a Matlab application program called the Block Detector Analysis program (BDA) developed in our lab. For each event, the BDA calculates the X and Y coordinates and projects that location onto an image of 512×512 pixels. For each event, the color intensity of the pixel corresponding to the location of that event is incremented by one. Once this has been done for all events in the raw data file, an image is produced displaying the recorded events as pixels along with a color scale which depicts the range of pixel count values. The image is known as a histogram image. If the data has been acquired by uniformly irradiating the surface of the detector with a radioactive source, such as a rod Ge-68 source as used in the experiments in this thesis project, the image is called a flood histogram. The energy values at this point are ADC voltage values. Figure 2-9(a) shows a flood histogram acquired from one of the detector modules in the PET insert system.

Since the crystal block consists of many small crystals (409 in two layers as previously described), the events depicted in a histogram image group around individual crystal centers. The flood image can thus be used to construct a map of crystal locations known as the Crystal Lookup Table (CLUT). In the BDA program, this is implemented as a manual process in which the user simply clicks on crystal centre locations and the BDA program draws a region of pre-set diameter around the centre location. This yields the CLUT as a 512×512 matrix of numbers assigning each cell in the histogram image to one crystal within the scintillation crystal block. Figure 2-9 (b) shows a flood histogram with the CLUT applied.

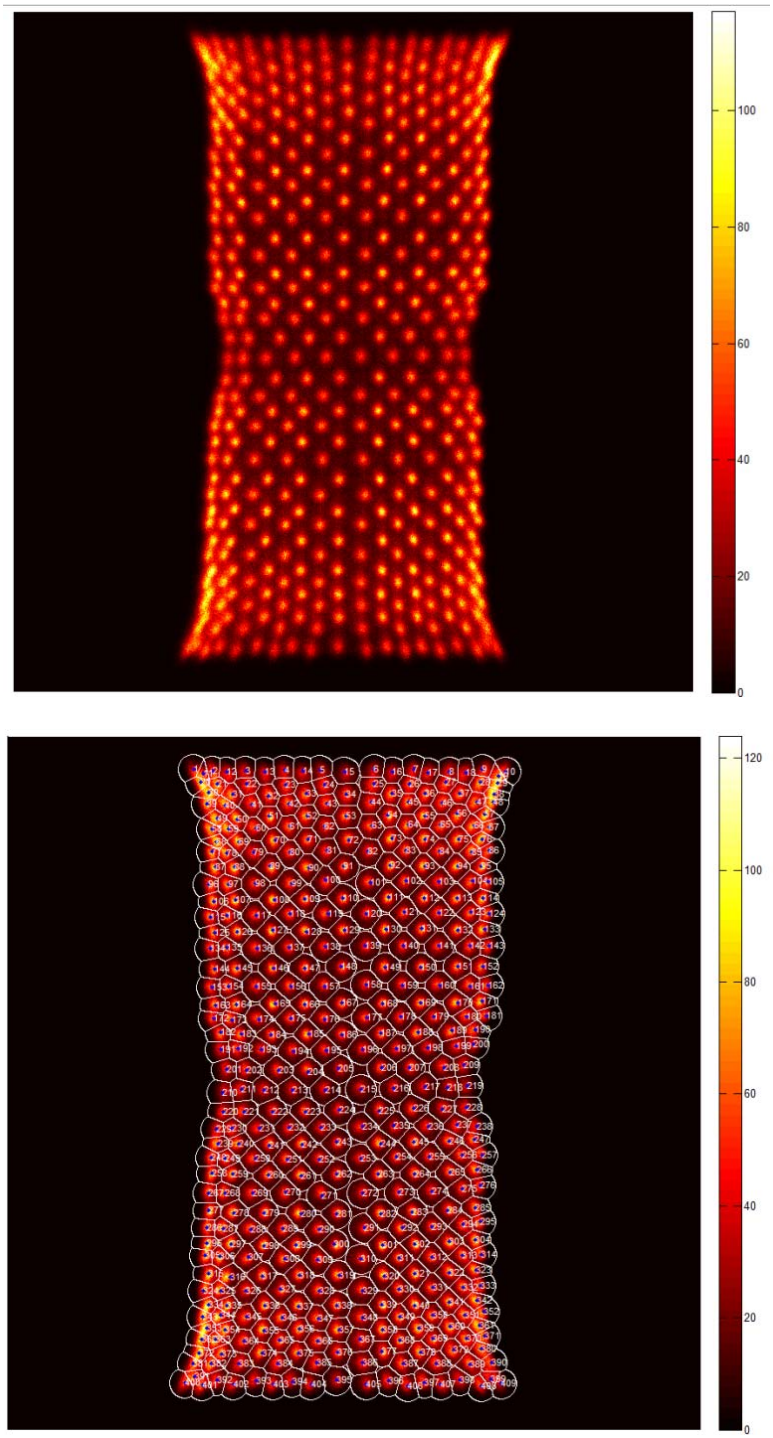

Figure 2-9. (a) Flood histogram produced by the BDA program of a detector module in the PET insert system. (b) the same flood histogram with the Crystal Lookup Table (CLUT) applied.

For each crystal in the block, an energy histogram is generated by putting the events into one of 256 bins based on the value of their energy. The range of energies in the acquired data is divided

into 256 bins to make it easier to analyze data. After binning the events for each crystal, it is possible to draw a histogram of events for each crystal based on the number of events in each energy bin. This histogram is known as the energy histogram of the crystal. It shows the energy bins on the horizontal axis and the number of counts on the vertical, as depicted in Figure 2-10(a). An energy histogram clearly demonstrates the existence of a 511keV photopeak which is of interest for the PET system. To find the exact position of the photopeak, a Gaussian plus line function curve is fit to the photopeak in the BDA program, and the value of the energy bin corresponding to the centre of the photopeak as well as the Full Width at Half Maximum (FWHM) value of the Gaussian curve expressed as a percentage value are recorded. The photopeak voltage is defined as the voltage value of the bin where the peak is located. The FWHM percentage value is referred to as energy resolution and is a measure of how precisely the energy of an event can be measured. A lower value of energy resolution corresponds to a more accurate detector. The position of the photopeak for each crystal within the block is saved in a matrix with as many elements as the crystals and is referred to as the Energy Lookup Table (ELUT). Figure 2-10 (b) shows the histogram in which the position of the photopeak and the energy resolution have been derived by fitting a Gaussian plus line curve.

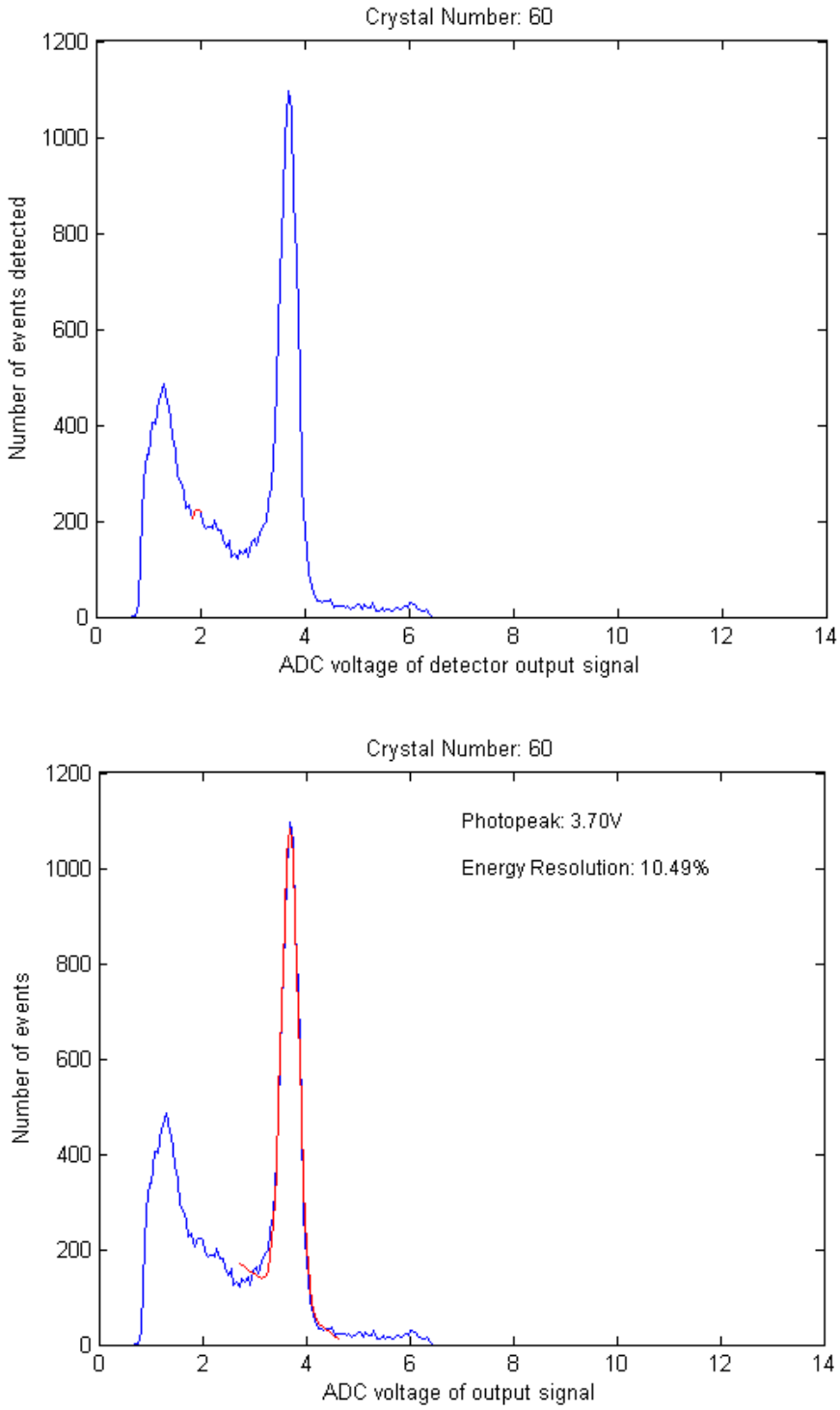

Figure 2-10. (a) Energy histogram for a crystal element. (b) The same energy histogram with a Gaussian fit and the position of the photopeak identified.

The crystal block contains two interleaving layers of crystals as previously described in this chapter. The analysis programs follow the same naming convention for the individual crystals as shown in Figure 2-11. Numbering starts from the left top corner of the flood image. This facilitates comparison of data from different flood images. For each crystal element identified in the CLUT, several parameters of interest are saved in a matrix in the BDA program. These parameters include the position of the photopeak, the energy resolution, and the number of events recorded in an energy window.

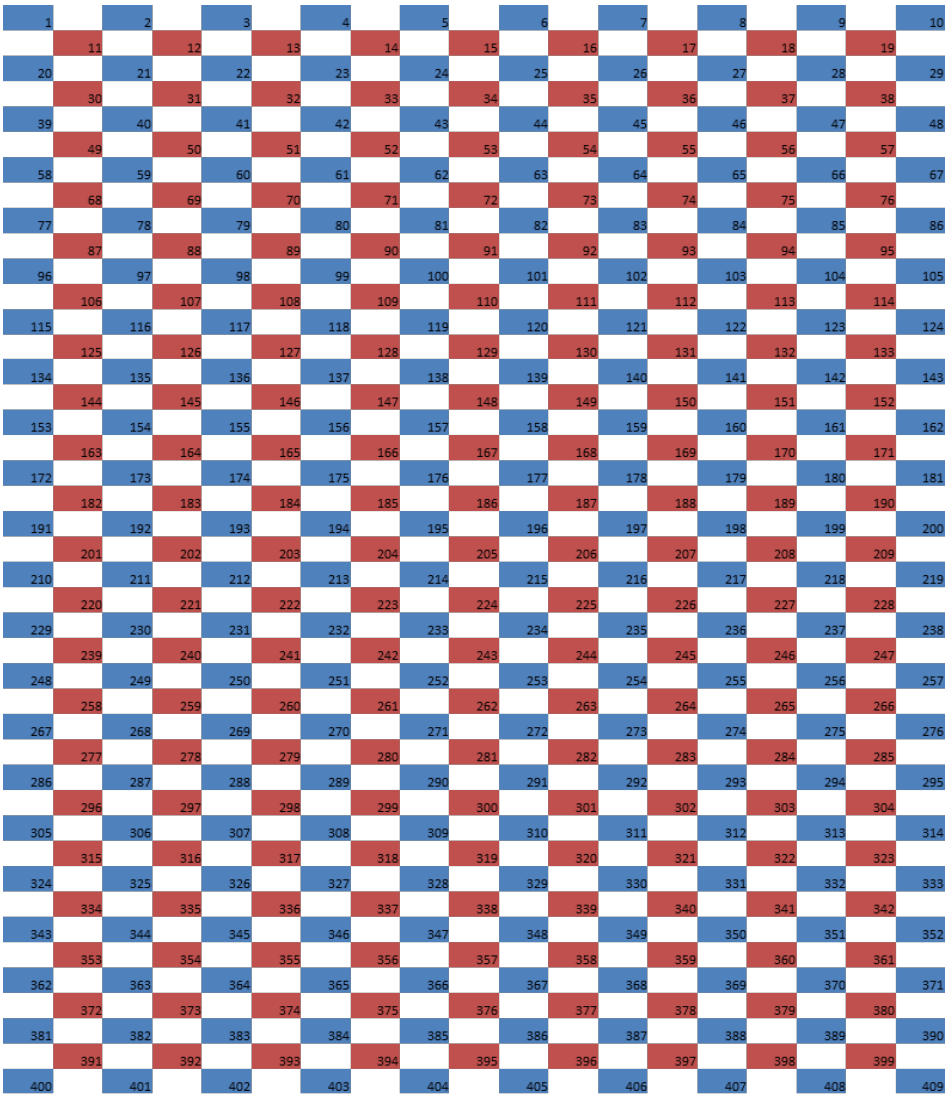

Figure 2-11. The individual crystals in the scintillation block used in the detector modules are numbered by the analysis program. In this picture, crystals colored red belong to the top layer.

Chapter 3

A slow control system for an MR-compatible PET Insert

3.1 The slow control system

It is necessary to have a means of controlling and monitoring the operation of the detector modules in the PET insert system. The output of the block detectors depends on bias voltage and temperature. Both of these parameters can be monitored to ascertain that the detectors are within their acceptable mode of operation. Furthermore, dynamic compensation can be initiated by the control system should the detectors report fluctuations in temperature. Emergency measures can be taken in case the detectors deviate from the acceptable range of operational parameters (e.g. temperature, bias current) to prevent damage to detectors or recording of useless data.

It is assumed that there are no stringent timing requirements on the control system. It is considered sufficient for the system to continuously monitor the operating parameters of the detectors and adopt appropriate measures as long as the latencies do not prevent the normal and safe operation of the PET insert system. The control system described in this section is therefore a “slow” control system.

3.1.1 Objectives

The following objectives are to be achieved by the slow control system for our PET insert system:

1. Scalability: The PET insert system has 16 detectors in the prototype phase. The control system must be able to seamlessly accommodate the increase in the number of detectors without losing effectiveness and efficiency.

2. Operational control and stabilization: The control system must continuously monitor operational parameters and apply adjustments of bias voltage to compensate for possible changes in temperature. See the following chapter for an in-depth analysis of the dependence of the output of the detector modules on temperature and bias voltage as the basis for such adjustment.
3. User interface: The operator of the PET system must be presented with a panel where he/she can monitor the control system and apply commands if necessary.
4. Distributed control: For the SiPMs to operate in Geiger mode, but still remain within a safe operational range, it is vital that the bias voltage not exceed safe values but be above the value of breakdown voltage. Similarly, monitoring of temperature must ensure that extreme temperature conditions are responded to regardless of whether a human operator is present or not. It is important that vital control responsibilities be placed as close to the detectors as possible so that they are not disrupted by loss of connectivity to the control server or absence of a human operator. This speaks to the importance of implementing a distributed control system where responsibilities are divided among a hierarchy of components.

3.1.2 Architecture

The implemented slow control system is a distributed networked system comprising a central "host PC" connected to each DIB (of which there are four units in the PET insert prototype) on a switched Ethernet-based TCP/IP network. The "client" control program on each DIB monitors the operational parameters of the connected detector modules (namely bias voltage, bias current and temperature) and contains the necessary logic to apply emergency control measures should these parameters fall outside safe operating conditions. The clients and the host PC exchange

text-based messages over the network. The content of these messages include the operational parameters reported by each client, client status messages, server commands, time synchronization packages and heartbeat signals to keep track of network connectivity. Figure 3-1 shows a diagram of the control system for the PET insert prototype.

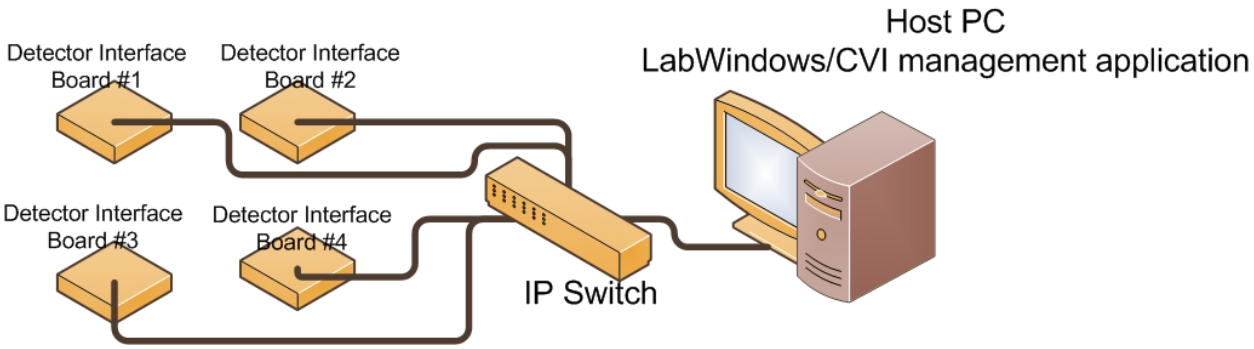

Figure 3-1. The slow control system relies on a TCP/IP network to distribute control tasks and present a seamless view to the user.

3.1.3 The DIB client control program

The DIB client control program is executed on the Raspberry Pi computer on each DIB. This program is implemented in the Python programming language. It uses the "Asyncore" class in Python to implement a TCP/IP client that continuously sends a text-based message to the server. In each iteration through a loop, the program polls the ADC on the DIB to read the temperature, bias voltage and bias current values from each detector. If a command has been received from a server to update bias voltage for any detector(s), the desired value is written to the digital to analog converter (DAC) in the same loop. This loop is executed in a separate thread of execution than the main program. The main program keeps track of the network connection and carries out hand-shaking with the server. Should the network connection be lost for any reason, the program tries to re-establish the connection indefinitely. The DIB client control program does not present a user interface and is automatically started when the DIB is powered up. All troubleshooting,

configuration and monitoring is done through the server program which runs on the host PC. The client program has the following features:

1. Use of multithreading: A separate thread executes the main loop which runs indefinitely and polls the ADC as well as writes to the DAC. This is different from the thread that monitors the status of the network. This allows the control loop to run without interference.
2. Logging: The Python Logging class is used to log events to a text file with four significance levels of information, warning, error and critical error. A rotating log file scheme is used to start a new log file for output once the maximum size is reached. Both the number of log files and the maximum size are configurable.
3. Separate configuration file: In order to communicate with hardware components such as the ADC and the DAC, the DIB client program relies on addresses on the I2C bus. There are also other parameters such as the conversion delay time of the ADC. Such parameters are kept in a text file with the format defined by Python's "Configparser" class. The contents of the config file are read when the client program is started at powerup. The following section explains how these parameters can be changed by the Host PC control program.
4. Exception handling: Python's exception classes are used to handle exceptions by taking appropriate actions. All exceptions are logged and the server is notified. Some exceptions such as a hardware access error lead to the control loop being stopped and the server being asked to double check the hardware addresses in the configuration file.

3.1.4 The host PC control program

The host PC control server is implemented using the NI LabWindows/CVI 2013 software environment and runs on a PC running Microsoft Windows. In order to simultaneously and seamlessly serve all DIBs in the PET insert system, the host PC program relies on the multithreading capabilities of the C programming language to create a separate thread of execution for each Raspberry Pi computer once connection is established. The program presents a graphical user interface in which messages received from each client program are displayed as temperature, voltage and current readings. The user can choose to run the program in automatic mode where the internal logic of the program is employed to control bias voltage so that a stable detector output is achieved or to run it in manual mode with the possibility of overriding program settings for detector bias voltage. The host PC control program has the following features:

1. Use of multithreading: Communication, message parsing and user interface are all managed by a separate thread of execution for each connected DIB. This ensures immediate processing of client messages and an uninterrupted user experience.
2. Remote management of client configuration files: Configuration files that define hardware addresses and other settings for communication of the client program with the DIB electronic components can be modified on the server side via the graphical user interface. Configuration files can also be backed up to the local disk on the host PC for future reference or disaster recovery.
3. Ability to view, back up and purge client log files: the contents of the client log files can be viewed on the host PC or saved to its local disk. To free up space on the Raspberry Pi computers when necessary, the contents of the log files can be deleted.

3.1.5 Main functions of the slow control system

The DIB client and the host PC control programs collaborate to implement the slow control system. A detailed description of the slow control system software is included in appendix A. Some major functions of the slow control system are listed below.

1. Supply of bias voltage to detectors

   The DIB client program uses the I2C bus to communicate with the DAC on the DIB. Inputs to the DAC control the bias voltage to the detector modules. Messages exchanged between the client program and the host PC control program report the amount of supplied voltage or set it to a desired value.

2. Monitoring

   Through messages exchanged between the two pieces of the slow control system (i.e. the DIB client and the host PC control program), the values for temperature, bias voltage and bias current read back from each detector module by the ADC are reported, logged and displayed. Figure 3-2 shows a screen capture from the host PC control program.

3. Characterization of detector modules

   Breakdown voltage is the most important value that characterizes a detector module and determines the appropriate level of bias voltage for its optimal operation. The host PC control program directs the DIB client through a series of messages to gradually increase bias voltage to a detector module in certain increments and record the bias current. The voltage-current value pairs are then used by the host PC control program to derive the value of breakdown voltage by

a process described in chapter 1. Figure 3-3 shows how this process is presented to the human operator by the host PC control program.

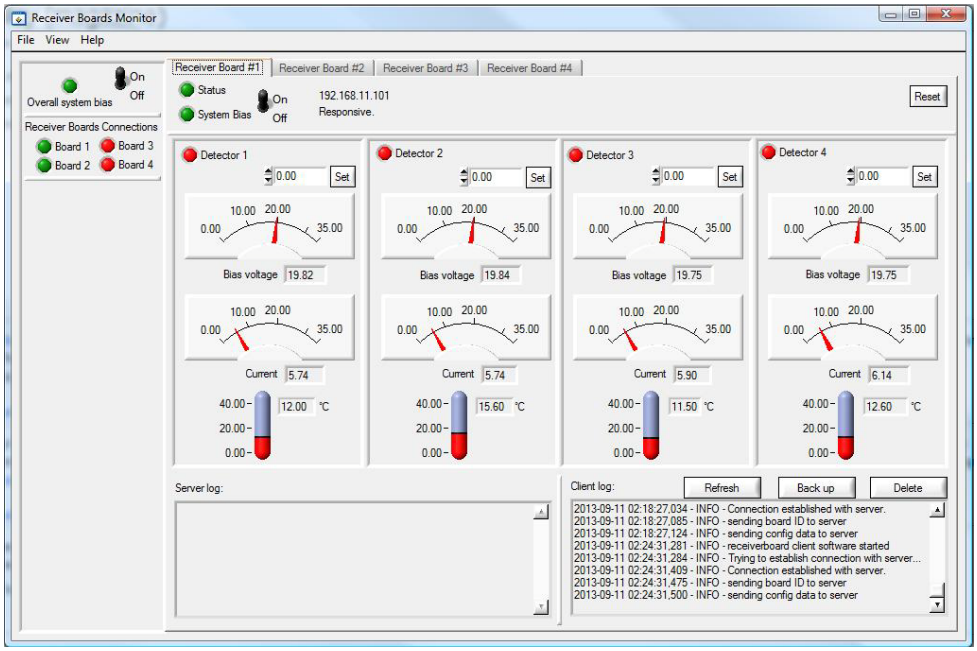

Figure 3-2. Operating conditions of detectors are continuously monitored by the slow control system.

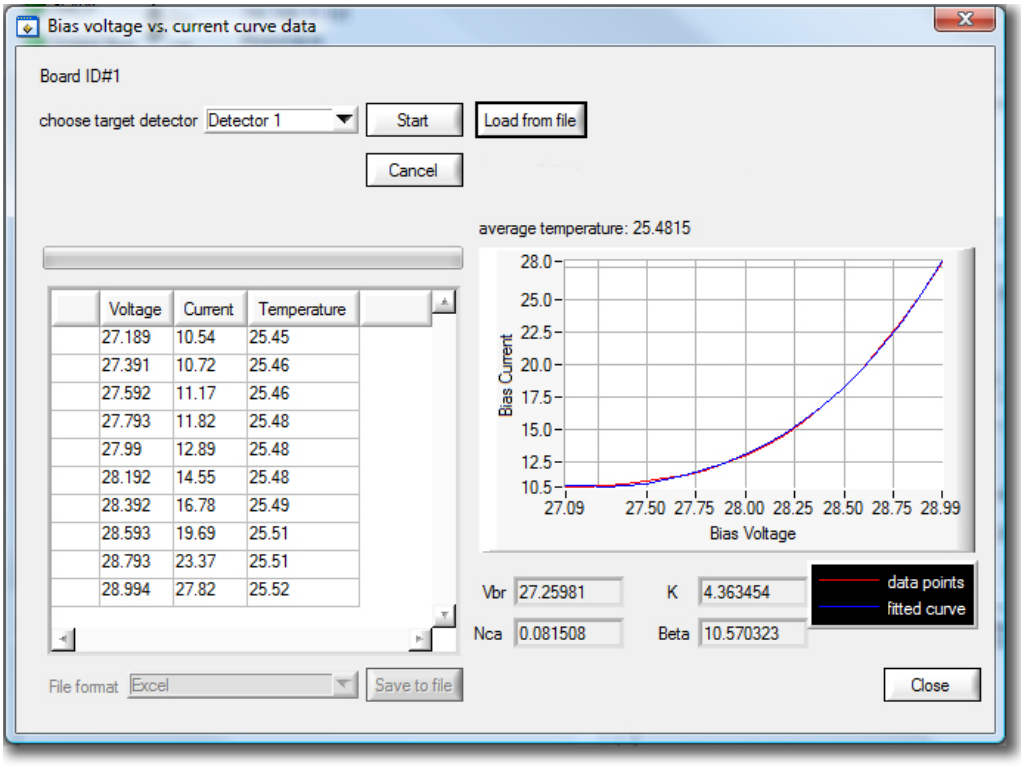

Figure 3-3. The slow control system derives the breakdown voltage value for detectors.

It is essential for the slow control system to have a characterization of detector output across the range of temperatures in which stabilization is to be achieved. The detector module in the PET insert system comprises two components whose output changes with temperature and bias voltage, namely the crystal block and the SiPMs. Characterization of detector output needs to take place as a calibration step to ensure a stabilized output, as it is not possible for the system to dynamically calculate detector characteristics such as breakdown voltage during image acquisition.

Once detector behaviour is characterized with respect to temperature and bias voltage, it will become clear whether the gantry needs to be air-cooled or if adjustments to bias voltage are sufficient to stabilize detector output. Results from the MR compatibility test reveal the range across which the temperature inside the gantry might vary, but more information is required as to how effective it would be to rely on bias voltage as the sole means of achieving a relatively stable output.

The next chapter details the bench top experiments performed to stabilize the output of one detector module. The results of this experiment will be implemented in the next revision of the slow control system as a calibration step that could be executed periodically or upon replacement of one or more detector modules.

Chapter 4

Stabilization of detector output

This chapter is divided into two sections. Section 4.1 describes the results of testing the PET insert prototype for MR compatibility and characterization of detector modules. Results from these studies shed light on the properties of the PET insert and the temperatures inside the gantry during operation. Section 4.2 describes studies aimed at achieving a stable detector output despite potential drifts in temperature.

4.1 Detector characterization and prototype testing

The breakdown voltage is the most important metric that determines the supply voltage to the detector modules. To gain an understanding of the range of breakdown voltages, all SiPMs used in the system were tested to determine their breakdown voltage. The PET insert prototype was also tested in the MR system. Various tests were performed in this process, but this thesis project mainly concerns the results obtained from monitoring temperatures in the gantry.

4.1.1 Characterization of SiPMs on the bench top

In order to construct the PET insert prototype, 36 B-series SensL SiPMs were obtained. As each detector module in this system uses two SiPMs, this quantity of SiPMs would yield two redundant items for use in tests and also as backup. The SiPMs were tested to characterize their breakdown voltage at 25°C.

To facilitate the study of the properties of each SiPM, an earlier version of the transmitter board (Referred to as revision 2) was used that would house only one SiPM module. A 4X4 LYSO crystal array was put on the SiPM for the characterization study. A programmable power supply (Agilent N6700B) was used to provide power to the differential amplifiers (which require +2.8V

and -2.8V to operate) and the SiPMs on the transmitter board. A software program was developed in NI CVI/LabWindows using the driver software provided by the power supply vendor to control the power supply. This control software was also able to read and record bias current through a digital multimeter (Agilent 34410A).

A Peltier cooler/heater in combination with a temperature controller (Laird Technologies PR-59) was used to control the temperature inside a box. The box (shown in Figure 4-1) was made light tight by lining the inside with a layer of Styrofoam painted flat black on the inner surface. The temperature controller included software that communicated with it through the RS-232 serial interface. Once the detector module was placed firmly inside the box, the box would be sealed and the desirable temperature would be set in software. The study would proceed for each SiPM once the inside temperature had stabilized to within 0.1°C of target temperature.

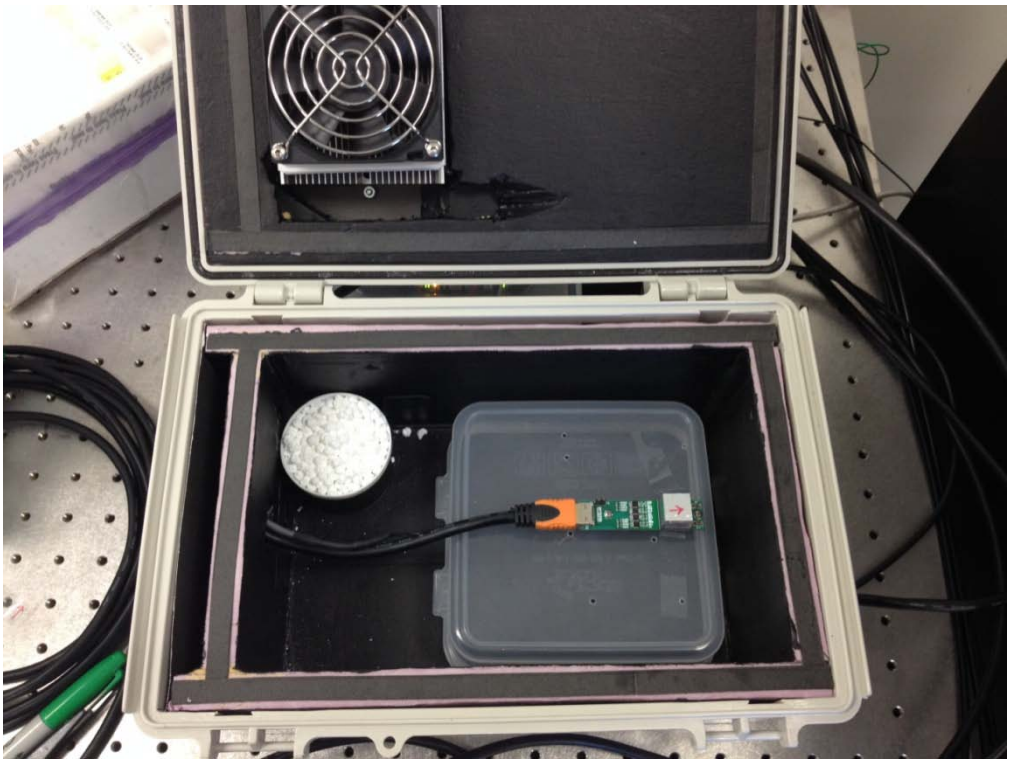

Figure 4-1. The temperature control box used to stablizie ambient temperature.

In order to measure the breakdown voltage, the supplied voltage to each SiPM was stepped up in increments of 0.1V in the range of 22V to 28V. The voltage/current value pairs were saved to a CSV file by the power control program. The CSV file was then processed by a Matlab script to find the voltage point where the current-voltage curve would break into an exponential as described in the previous chapter. Breakdown voltage for the SiPMs at 25°C was consistent among all SiPMs. The mean value of breakdown voltage was found to be 24.54V with a standard deviation of 0.04V. Figure 4-2 shows values of bias current against bias voltage for all tested SiPMs. This result demonstrates that the SiPMs are very uniform in their operating parameters and careful matching of SiPM modules to be paired into the same detector module is not required. Breakdown voltages for each SiPM as well as values obtained for other fit parameters are included in Appendix B.

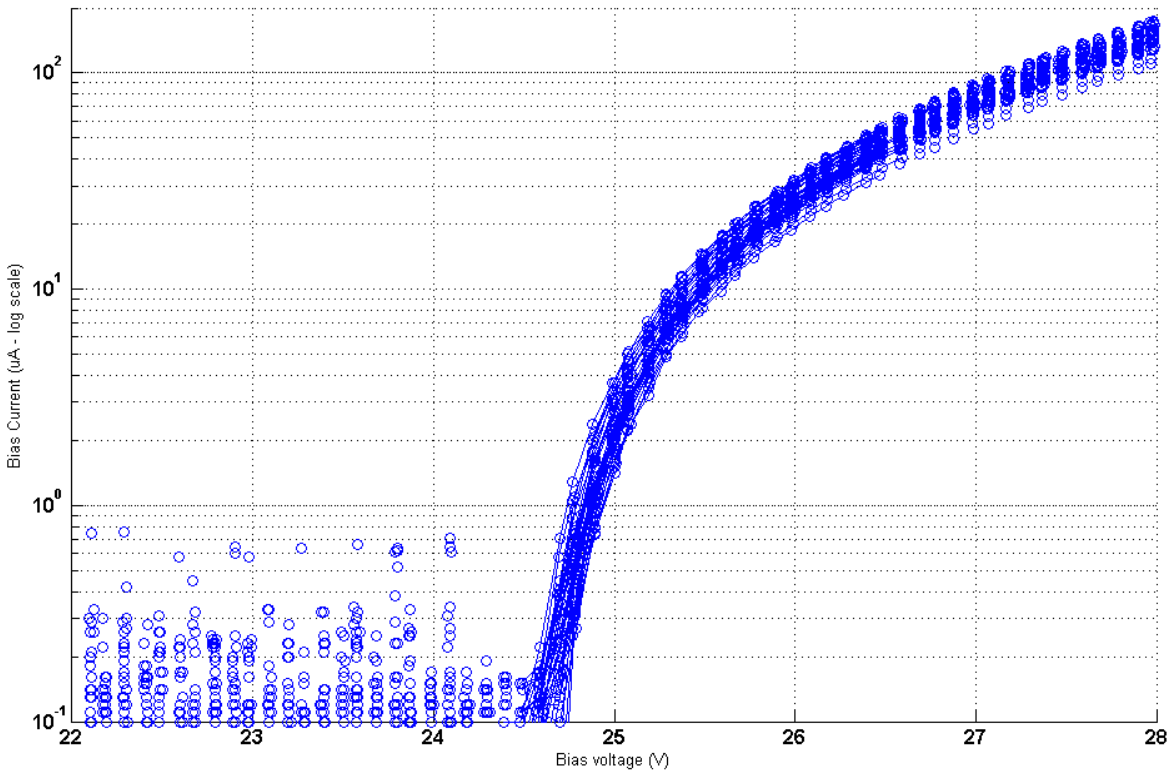

Figure 4-2. Bias current vs. bias voltage with fit lines for all 36 SiPMs (the vertical axis depicting bias current is displayed in a log scale).

4.1.2 MR-Compatibility testing of the PET insert prototype

The PET insert prototype was tested for MR compatibility in May, 2014. Flood images[2] were acquired from several detector modules with and without MR sequences running. Flood images were also acquired from two detector modules in coincidence mode simultaneously with various MR sequences and without any MR sequences being run. HDMI cables carrying signals from the PET insert were routed out of the MR room through an opening in the top of the MR shielding, and connected to electronics sitting close to but outside the shielded MR room. No interference was observed from the MR system in the flood images obtained from detectors.

4.1.2.5 The Power Distribution Board

Successful MR compatibility testing of the prototype necessitated that all 16 detector modules receive power. In addition to looking for possible interference between the PET and MR imaging modalities, the goal of the compatibility test was to gain an understanding of power consumption and temperature of detector modules. Specifically, the possible formation of a temperature gradient in different directions was to be investigated while all detector modules were powered.

The SiPMs used in building the detector modules were the B-Series SiPMs manufactured by SensL. These SiPMs require a negative bias voltage to operate; however, the current revision of the DIB does not provide negative bias voltage to detectors as it was designed to work with the SensL M-Series SiPMs. However, the DIB does have an external bias line for each connected detector module that can be used to supply bias voltage with any polarity independently of the electronic components on the DIB.

A Power Distribution Board (henceforth referred to as PDB) was designed and manufactured to enable the supply of bias voltage to all 16 detectors at the same time. This board has a connector

[2] The concept of flood images is discussed in detail in Chapter 3.

head that receives the desirable SiPM bias voltage, amplifier supply voltage, and ground from an external power supply and routes these lines to 16 HDMI connectors. One temperature readback line is also routed from each HDMI connector to a 68-pin connector head. The pinout of this connector head was chosen to match a commercially available USB DAQ system manufactured by National Instruments.

It was envisioned that the PDB would provide the capability to run all 16 detector modules during the compatibility testing, monitor the amount of consumed power by the gantry, and also gain an understanding of the temperature reported by the sensor on each detector module. In total the sixteen detector modules pulled 0.6A at +2.8V and 0.6A at -2.8V. This means that the power consumption is 0.21W for each detector module or, 3.36W for the entire gantry.

At the time of the MR compatibility test, efforts to acquire temperature data by using the PDB yielded inaccurate results due to a malfunction in the USB DAQ module. It was then decided that a DIB would be used to read temperature data from four detector modules at a time. By choosing these four detector modules in the four quarters of the gantry, an better understanding of the temperature variations could be gained.

4.1.2.6 The temperature gradient

The following results were obtained after monitoring the temperature reported by the sensor on the detector modules for several detectors modules:

1. Regardless of location of the detector module, the temperature reported by a detector module would increase logarithmically before stabilizing at an equilibrium value. With all 16 detector modules running, the amount of time to reach equilibrium conditions was almost 2 hours. Figure 4-3 shows the temperature reported by the onboard temperature

sensor by detectors 0(sitting at the top of gantry in the 12 o'clock position) and 8(sitting at the bottom of the gantry in the 6 o'clock position).

2. The temperature reported by the detector module sitting on top of the gantry (detector 0) was consistently close to 2°C higher than that reported by the detector module sitting at the bottom (see Figure 4-3).

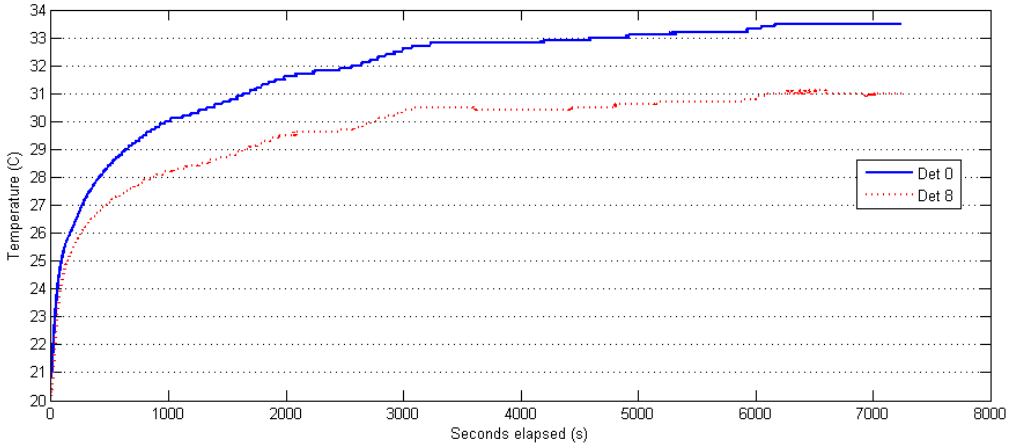

Figure 4-3. The ambient temperature as reported by the onboard temperature sensor of the detector module for detectors 0 and 8 obtained while running various MR sequences.

3. The rest of the detector modules reported temperatures ranging in value between what was reported by the top and bottom modules, with the two side modules reporting values with a difference of almost one degree to the top and bottom.
4. Running MR sequences had no effect on the rate of temperature increase or the equilibrium value of temperature.
5. The most important source of heat in the detector modules was found to be the two amplifiers on the transmitter board. Starting or stopping bias voltage to the SiPM did not affect the rate of temperature increase or its final value.

The SiPMs in each detector module do not experience the same temperature reported by the temperature sensor. The temperature sensor on the transmitter board sits very close to the

amplifiers which are the major source of heat. Investigation of a possible axial temperature gradient in the gantry was deemed necessary.

The temperature controller, previously used to characterize SiPM modules, was used for this test as it could connect to up to three thermistors. Two thermistors were inserted into detector module 0 through the hole used to route the HDMI cable. One of the thermistors (T1) was positioned above the SiPM attached to the top surface of the crystal array. The other thermistor (T2) was placed directly above the onboard temperature sensor in a way that it did not come in contact with the onboard temperature sensor. Both T1 and T2 were calibrated prior to the test to ensure accurate temperature readings. The temperature controller program supplied by Laird Technologies was used to log readings from T1 and T2 in the form of a text file. The gantry was placed on the bench top and all 16 modules were powered using the PDB. The following results were obtained from this experiment:

1. The two-degree temperature difference exists between the top and bottom modules of the gantry when the two sensors are placed in identical locations inside the detector modules.
2. The temperature reported by the onboard sensor could be up to four degrees higher than the temperature reported by the thermistor placed adjacent to the SiPMs. This confirms that there is an axial temperature gradient in the gantry.
3. The equilibrium value of temperature was the same when the measurements were repeated on the bench top outside of the MR magnet.

4.2 Achieving a temperature invariant detector output

An important step in calibrating the PET insert gantry for image acquisition is obtaining the ELUT for each crystal in the system. The system would subsequently rely on the ELUT to filter out events that do not fall within a predefined energy window around the photopeak position. Derivation of the ELUT is a lengthy process that requires time and computing power to find the curve that best fits the energy histogram. It also sometimes entails a process of trial and error to find parameters that would yield the best fit. To this end, a separate Matlab application has been developed as part of this thesis work to, among other functionalities, assist in obtaining a better ELUT. This package, called SpectraAnalyzer, has been used in analyzing the data obtained for the experiments described in this chapter.

The photopeak position does not remain constant with changes in ambient temperature and/or bias voltage. This is due both to the properties of the SiPM and the scintillation crystal (see chapter 1 for a detailed discussion of these properties). A changing photopeak position means that the number of detected acceptable events (henceforth referred to as the number of count) would not remain constant. Figure 4-4 illustrates this concept by showing three energy histograms on the same axes. If the PET system is relying on calibration data gathered at T=30°C as depicted by the solid line, the photopeak position is inaccurate for an acquisition at T=36°C or T=26°C where the photopeak position is different. Consequently, the system will wind up accepting events that are not centred around the photopeak at these temperatures.

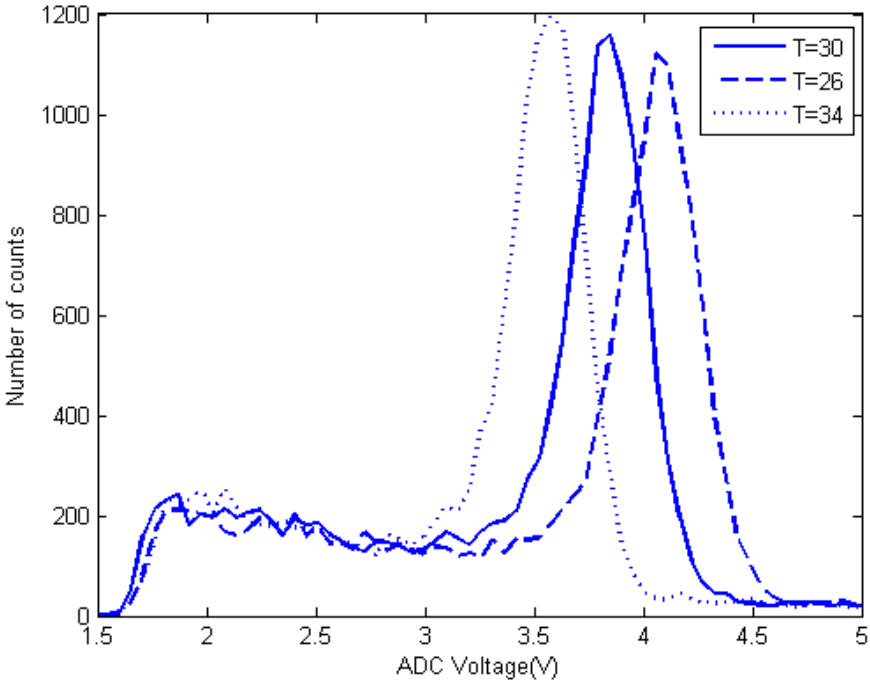

Figure 4-4. The change in photopeak position as a result of changes in temperature could lead to the PET system accepting low energy events because it relies on calibration data obtained at a different temperature.

One solution to the problem of a changing photopeak position could be keeping a lookup table of photopeak positions for each temperature. This is not an ideal solution for several reasons. The large number of crystals in the system would make the production of such a lookup table time-consuming considering that this lookup table needs to be prepared as a calibration step. Also, producing such a lookup table necessitates that the calibration process now take place in a laboratory where ambient temperature can be reliably controlled and kept constant for the duration of flood image acquisition. Should one of the detector modules need to be replaced, the calibration process would be complicated, time-consuming and prone to error. Furthermore, changes in temperature lead to changes in the photon detection efficiency of the detector and might manifest themselves as noise in the image leading to loss of resolution. For these reasons, it is important to take measures to stabilize detector output.

4.2.1 The hypotheses

The objective of the studies detailed in this chapter is to evaluate the effectiveness of using bias voltage adjustment to stabilize detector output in the PET insert system. The position of the photopeak, energy resolution and the number of incident photons that are accepted by the system as 511keV photons are taken as indicators of stability. It is desirable to achieve a constant photopeak position and energy resolution across a range of temperatures. This will guarantee a stable detector output.

Since bias voltage affects the gain of the SiPMs used in our detector modules, adjustments of bias voltage could be used to compensate for changes in output caused by temperature in both the SiPM and the scintillator block. Previous research, referred to in chapter 1, demonstrates that there is a linear relationship between overvoltage (OV) and the gain of a microcell in the SiPM, and that this linear relationship is independent of ambient temperature. Therefore, we hypothesize that maintaining a fixed overvoltage across a range of temperatures would lead to a markedly more stable detector output than when bias voltage is not adjusted to provide a fixed overvoltage. Testing this hypothesis is the first step outlined in this chapter in section 4.2.2.

Compensation for the effect of changes in temperature on detector output by maintaining a fixed overvoltage will likely not help compensate the effect of temperature changes on crystal light output. It is expected that results obtained with a fixed overvoltage might still show changes in our stability indicators which possibly arise from the scintillation crystal. Sections 4.2.3 and 4.2.4 describe two studies to fully compensate for such changes and achieve a relatively more stable detector output.

4.2.2 Output stabilization by maintaining a fixed overvoltage

4.2.2.7 Materials and Methods

The experiment was performed in the biomedical imaging laboratory of the University of Manitoba at John Buhler Research Centre in Winnipeg. Detector module 0 was taken from the PET insert gantry and placed in the box described below. Figure 4-5 shows a schematic representation of the experimental setup. The different components of this setup are described below.

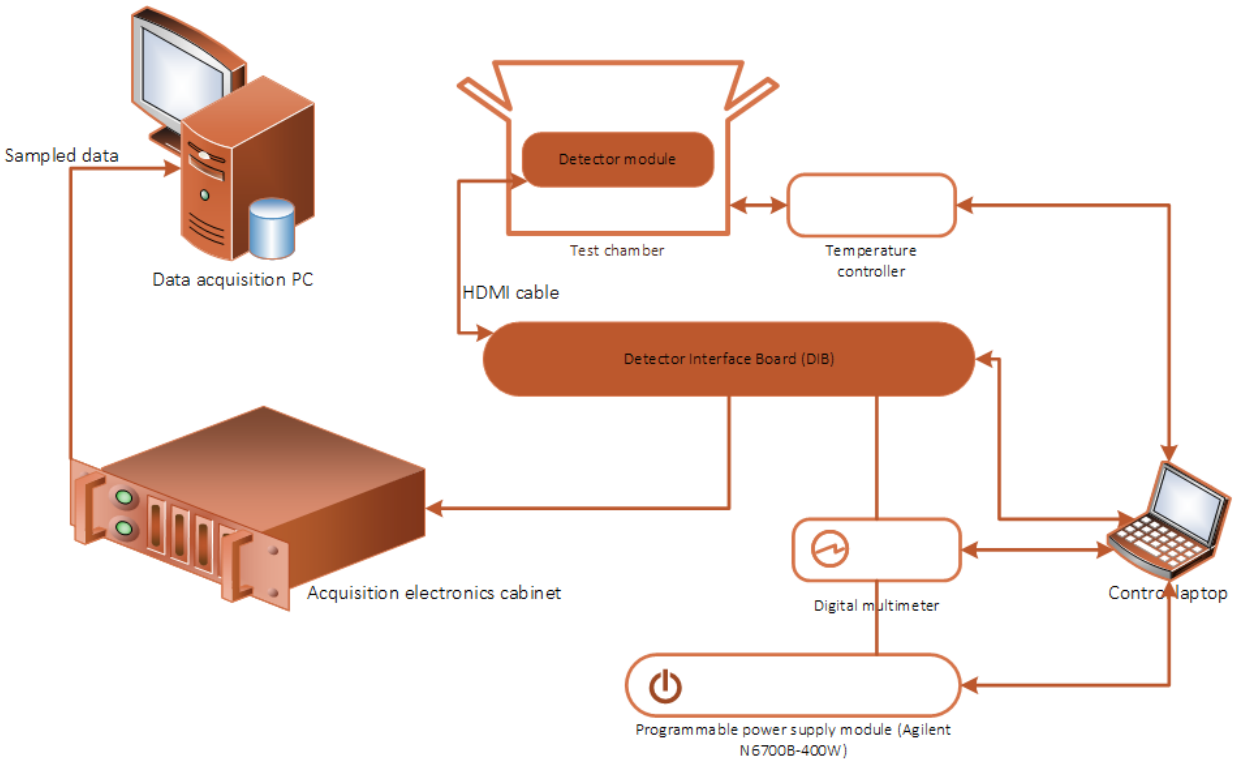

Figure 4-5. The experimental setup used in the experiments in this chapter.

- **Radioactive source and detector module**

To irradiate the detector and obtain a flood image for analysis, a Ge-68 line source was used. This source was manufactured by Eckert and Ziegler. The activity listed by the manufacturer was 37MBq and the reference date listed with the product was March, 2012. The activity was

calculated to be approximately 3.3MBq at the time of the experiment. The line source was taped to the outside of the lid of the test chamber so it could not move during the course of the experiments.

- **Power supply and control**

A N6700B-400Watt programmable power supply by Agilent Technologies was used to provide power to the detector module. This power supply is a four-channel power supply. A Labwindows/CVI control program was developed using drivers supplied by the manufacturers to control the supplied power.

A digital multimeter (Agilent 34410A) was connected serially with the bias voltage to the SiPM to enable monitoring of bias current. Although the DIB is equipped with electronics and software to this end, use of the external bias lines of the DIB to provide a negative bias voltage renders the DIB bias current and voltage read-backs unusable since they were designed for a positive bias voltage. Manufacturer software drivers of the digital multimeter were used to incorporate it into the Labwindows/CVI power supply control program to monitor bias current. This control program could also log bias voltage/current pairs when bias voltage was increased in predefined steps to measure the breakdown voltage of the detector module. Figure 4-6 shows a screen capture of the power supply control program.

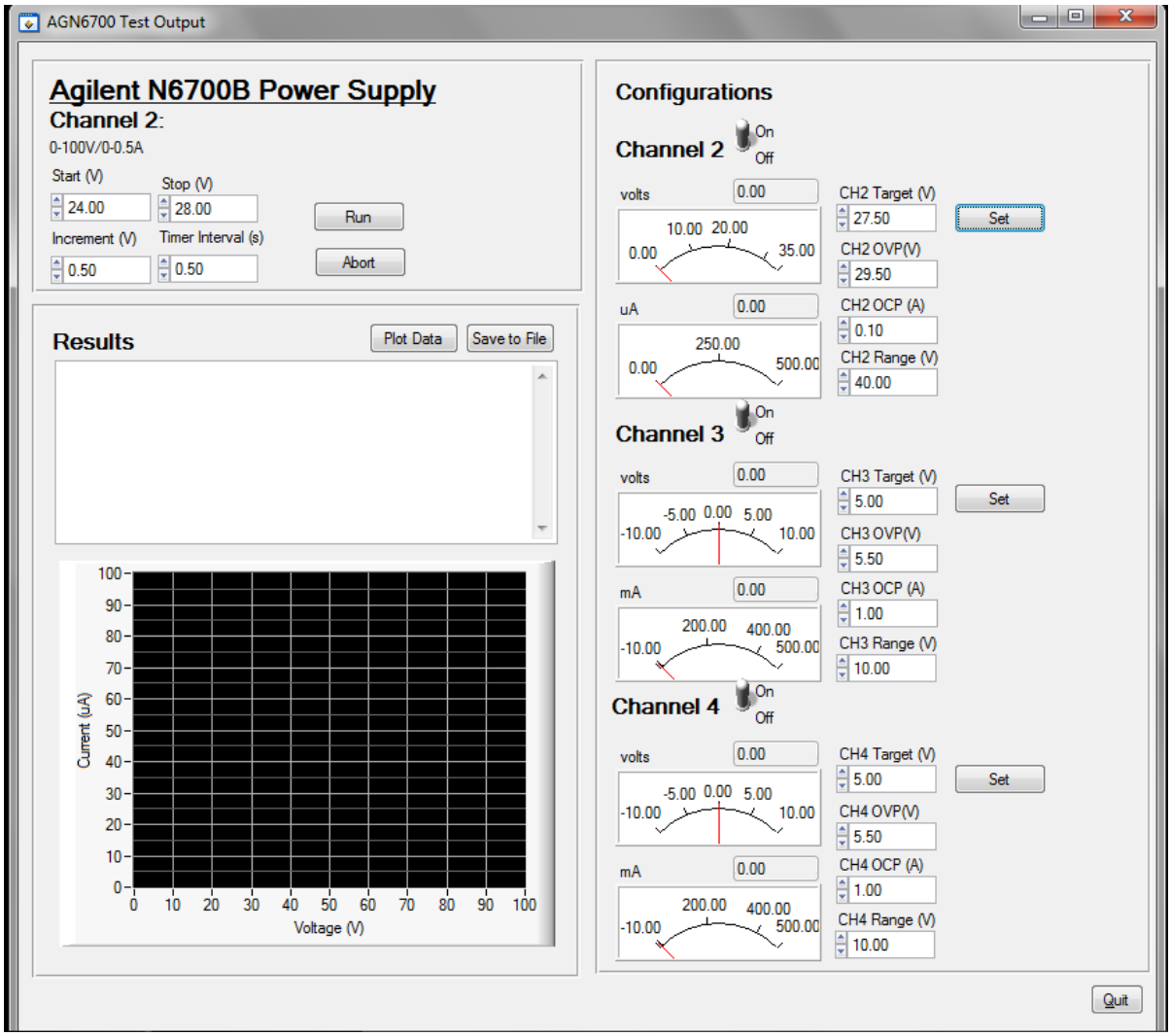

Figure 4-6. The Power control program is equipped to control the output of the power supply module as well as record bias current and voltage and plot the values.

- **Temperature controller and test chamber**

The test chamber used in this experiment consists of three components:

- Thermoelectric assembly manufactured by Laird Technologies which included a Peltier cooler/heater with fan (Model Number: AA-034-12-22): This unit is capable of acting as cooler or a heater depending on the polarity of the bias voltage and is equipped with a fan for better ventilation of the chamber.

- Temperature controller manufactured by Laird Technologies designed for cooling/heating of thermoelectric assemblies with two fan outputs, three thermistor inputs and an RS-232 interface to read and control parameters and settings in real time (Model Number: TC-XX-PR-59).
- Light tight box (11.81"×7.87"×6.29") the inside of which was covered with one layer of Styrofoam painted flat black. A hole was made in the lid for the thermoelectric assembly to be mounted. Another hole was made in the side of the box close to the bottom for the HDMI cable and the thermistors to be routed through. The cables were routed to the inside of the Styrofoam sheet through a different side of the box so that light could not enter. Refer to chapter 2 for an image of the light tight box.

- **Signal sampling and digitization**

The data acquisition electronics cabinet and the data acquisition PC previously described in chapter 2 have been used to acquire data for the experiments in this chapter.

- **Flood image segmentation and analysis**

The BDA and SpectraAnalyzer software programs were used for analysis of acquired data. The CLUT and energy histograms were made with the BDA and the resulting histograms were used in SpectraAnalyzer to derive photopeak position, energy resolution and the number of events within a predefined energy window for each crystal. The CLUT of reference was that made using data acquired at a baseline temperature of T=30°C.

- **Baseline temperature and bias voltage**

Based on results from chapter 2, we expect the temperature inside the gantry to stabilize around 34°C during operation. Similar results obtained on the bench top indicate a temperature difference of 4 degrees between the SiPMs and the temperature sensor on the detector. It seems plausible to assume that the SiPMs experience an ambient temperature close to 30°C during their operation. This temperature was adopted as the baseline temperature in the experiments in this section. Changes in stability indicators are evaluated at different temperatures and compared with values obtained at this baseline temperature.

Although results obtained with a specific overvoltage will likely apply to the use of any other overvoltage level, it was important to ascertain that flood images obtained at different temperatures in this experiment will be sufficiently free of noise and artefacts so that they would be analyzable and comparable with data obtained at the baseline temperature. To this end, some flood images were obtained at different OVs at the baseline temperature as depicted in Figure 4-7. The best quality flood was obtained using an OV of 2.5V.

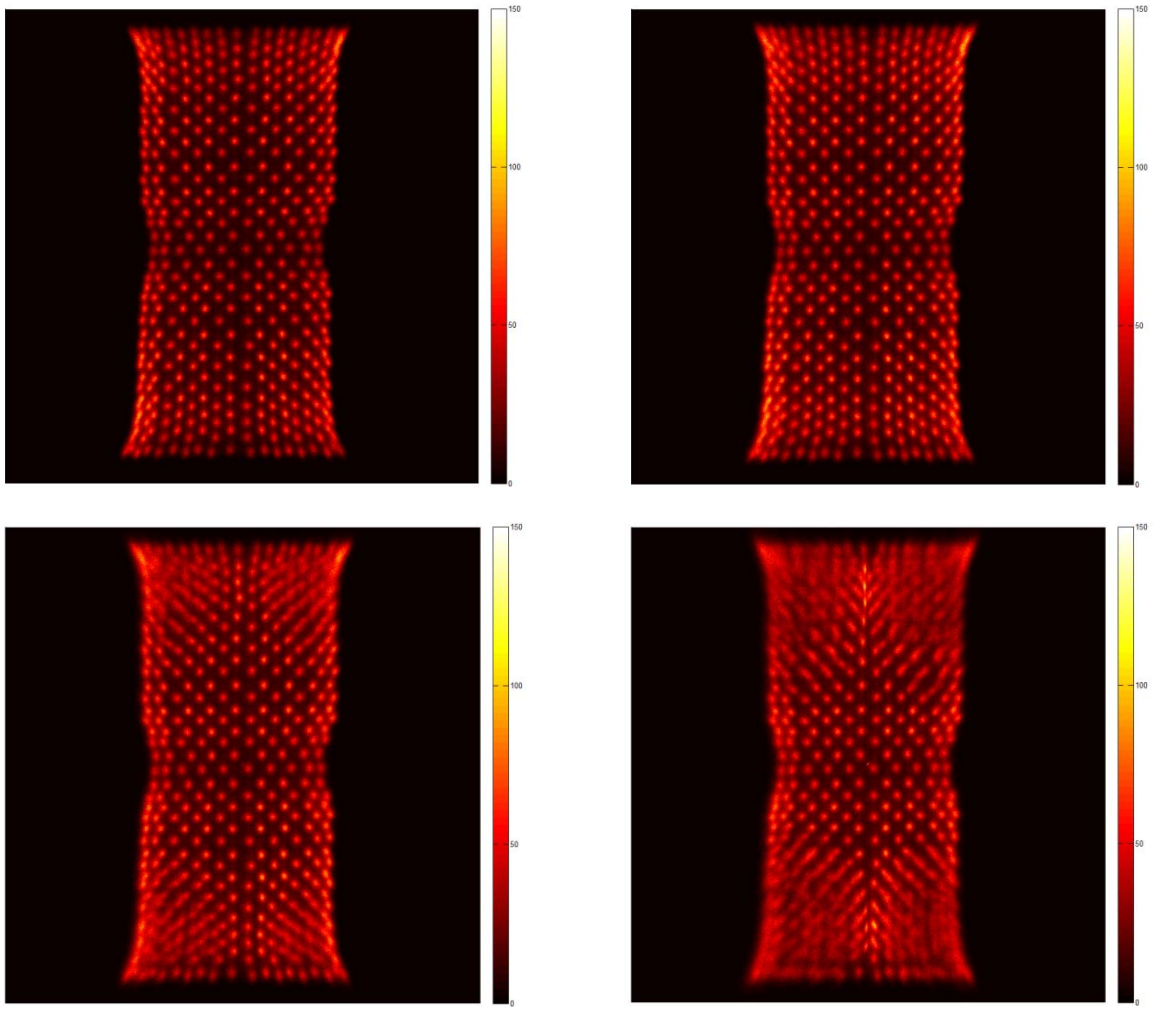

Figure 4-7. Flood images obtained with OVs of 2.5V(top left), 3.0V(top right), 3.5V(bottom left) and 4.0V(bottom right) at T=30°C.

- **The experimental procedure**

The baseline temperature was chosen to be 30°C. At each temperature point, enough time was allowed for the temperature to stabilize to within 0.1 degree of the target temperature. The range of temperatures tested was between 20°C and 40°C (inclusive) in increments of two degrees. The following steps were followed in this experiment:

1. The temperature was set to 30°C. Breakdown voltage was calculated. A flood image was acquired for t=600s at OV=2.5V (equal to 27.20V).

2. At each temperature between 20 and 40°C (except 30°C): Breakdown voltage was calculated. One flood image was acquired at OV=2.5V and another one with the bias voltage set to 27.20V (equal to OV of 2.5 at 30°C) for t=600s.

Equal acquisition times were used, making it possible to capture the change in the number of events detected with the change in temperature. The choice of bias voltages helps implement two control scenarios:

a) When a fixed bias voltage is used equal to an overvoltage of 2.5V at the baseline temperature (T=30°C).
b) When a fixed OV of 2.5V is used (i.e. bias voltage is adjusted with changes in temperature so that an overvoltage of 2.5V is maintained).

4.2.2.8 Results

Breakdown voltage increases linearly with ambient temperature. Figure 4-8 shows the value of breakdown voltage for each temperature along with a line fit to this data. The slope of the line is 16.5mV for each degree change in temperature.

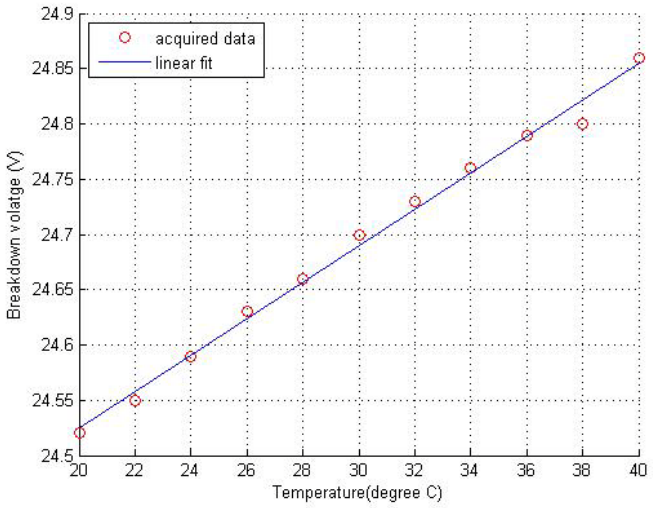

Figure 4-8. Breakdown voltage measured by using the dark current method outlined in chapter 1 at different temperatures for detector module 0 of the PET insert prototype.

With a fixed bias voltage, the position of the photopeak decreases in value as the temperature increases. In such a case, a decrease in temperature will lead to a rise in the value of the photopeak position. Taking 30°C as the reference temperature, the photopeak position of an individual crystal could increase in value by as much as 19% at 20°C when the bias voltage is kept constant. The photopeak position of an individual crystal could decrease by as much as 28% when the temperature rises to 40°C. When a fixed OV is maintained by adjusting bias voltage the corresponding change at 20°C and 40°C is equivalent to 6% and 15%. Figure 4-9 depicts this change in a color-coded representation of the crystal block for the top and bottom layers. The first two rows show the top and bottom layers colored according to the percent change in the position of the photopeak compared to the baseline temperature of 30°C. The bottom two rows show the layers in the same order when a fixed overvoltage is applied.

The number of acceptable events around the photopeak was found for the energy window spanning 350keV to 750keV. Color-coded maps depicting the change with respect to the baseline temperature are shown in Figure 4-10 for both cases of using a fixed bias voltage and adjusting

bias voltage at each temperature to maintain a fixed OV. In order to compare the number of events for each crystal at each temperature with that of the baseline temperature, the limits of the energy window at the baseline temperature were saved as a reference ELUT. Figure 4-11 shows an example of how this is done for a crystal. As the diagram shows, the photopeak for crystal #93 is found at the baseline temperature as well as at 26°C and 40°C. Solid black lines mark the photopeak positions at these temperatures. The voltage values corresponding to 350keV and 750keV are calculated at 30°C. These two limits are shown in the figure with dotted black lines. The position of these dotted black lines is saved as a reference ELUT and is used to count the number of events between these two limits at all other temperatures. Using this method, we have a reference energy window to compare the number of events between different temperatures. This process is repeated for all crystals at all temperatures. The SpectraAnalyzer software program, developed as part of this thesis, has the features necessary to derive this reference ELUT and to use it to count the number of events for other datasets obtained at other temperatures. In Figure 4-13, a reference energy window has been created at 30°C, and the average number of events falling within this energy window at different temperature points has been presented in this figure. The average is calculated across all 40 crystal elements. As the figure demonstrates, the average number of events is more stable when a fixed overvoltage is used. Figure 4-14 shows the value of energy resolution averaged across all 409 crystal elements at different tested temperatures for a fixed bias voltage and a fixed OV.

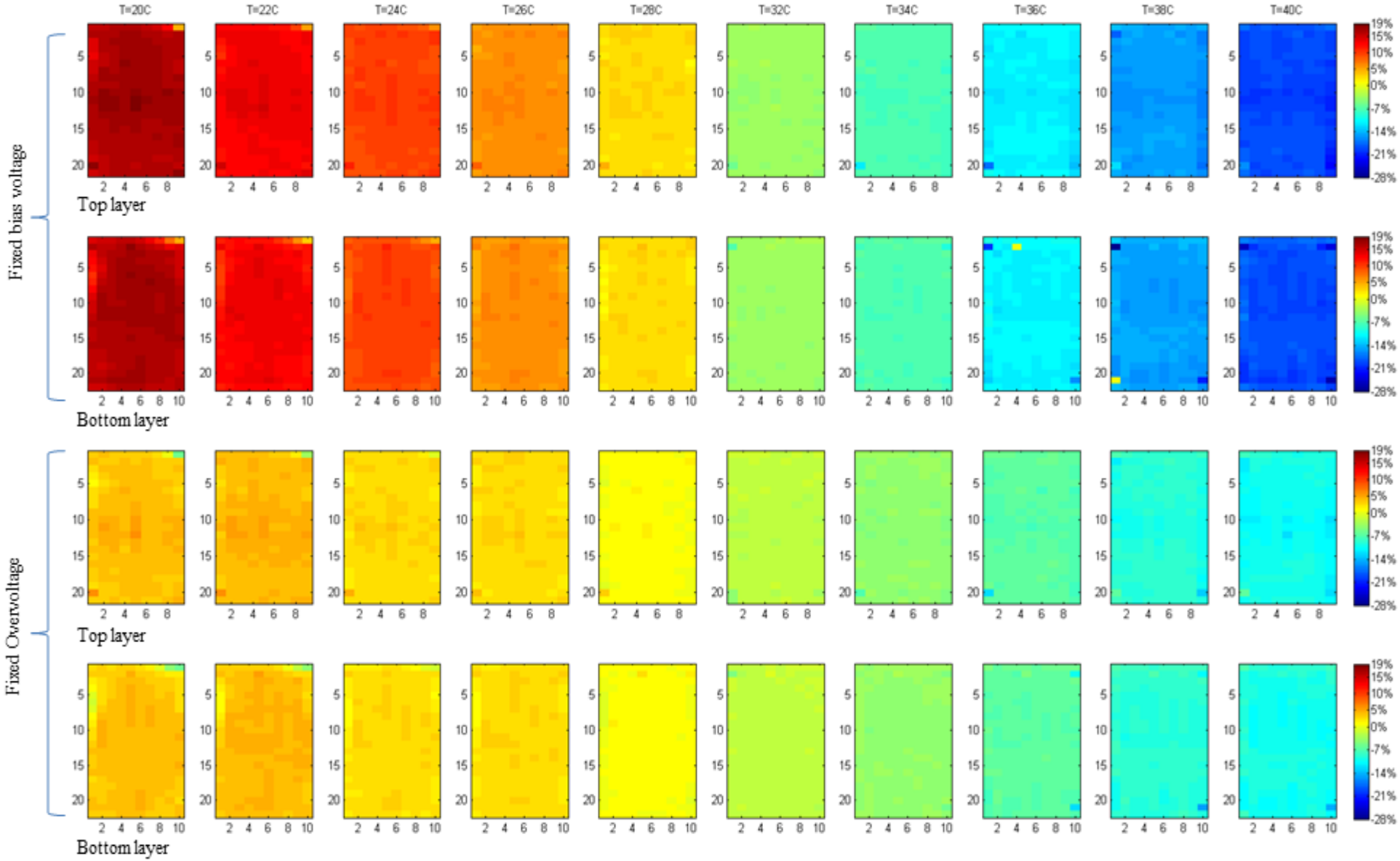

Figure 4-9.Percent change in the value of photopeak position compared to 30°C.

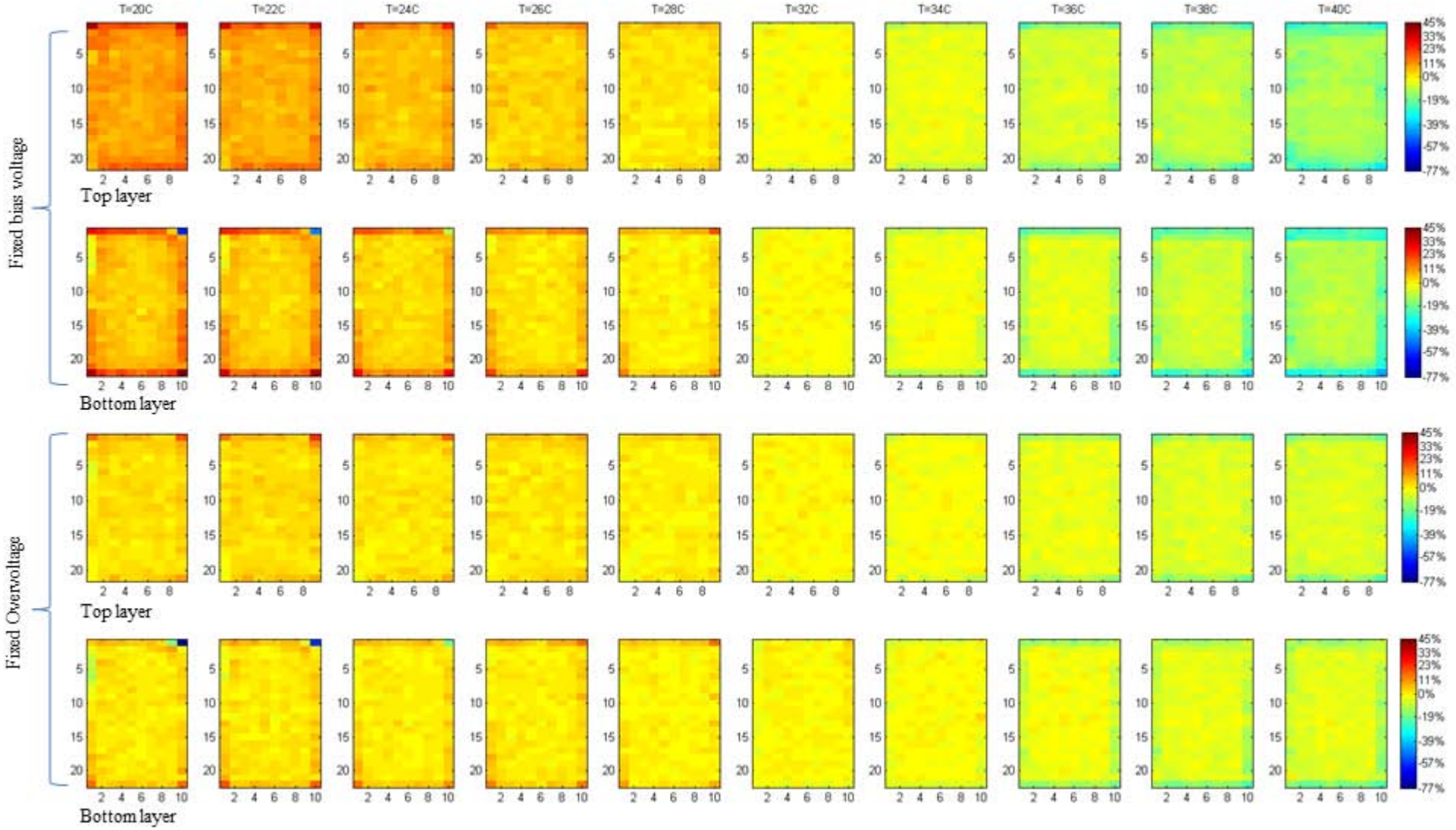

Figure 4-10. Percent change in the number of events in the reference energy window compared to 30°C.

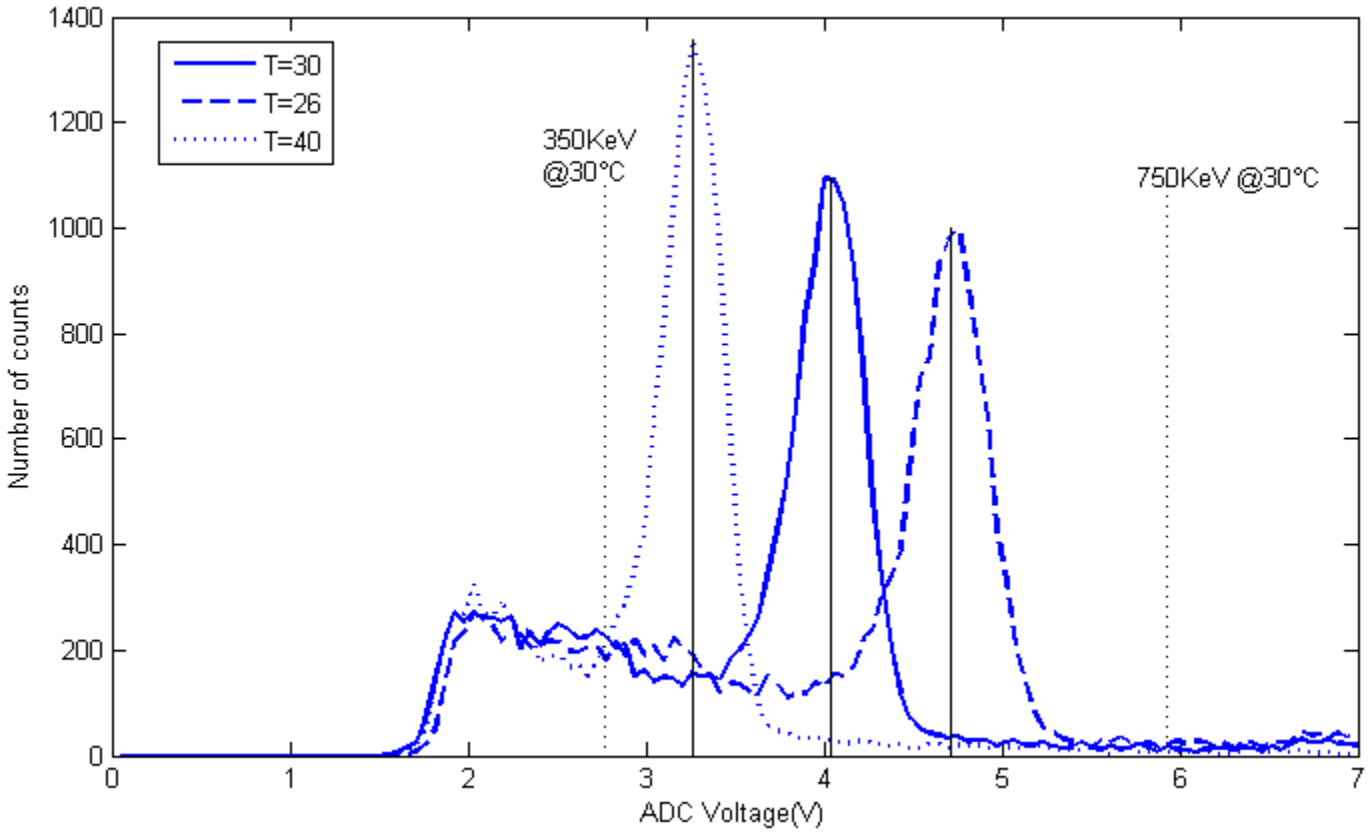

Figure 4-11. The energy histogram, position of the photopeaks at 26, 30 and 40°C for crystal #93; The voltages corresponding to 350keV and 750keV have been extrapolated based on the value of the 511keV photopeak voltage for 30°C.

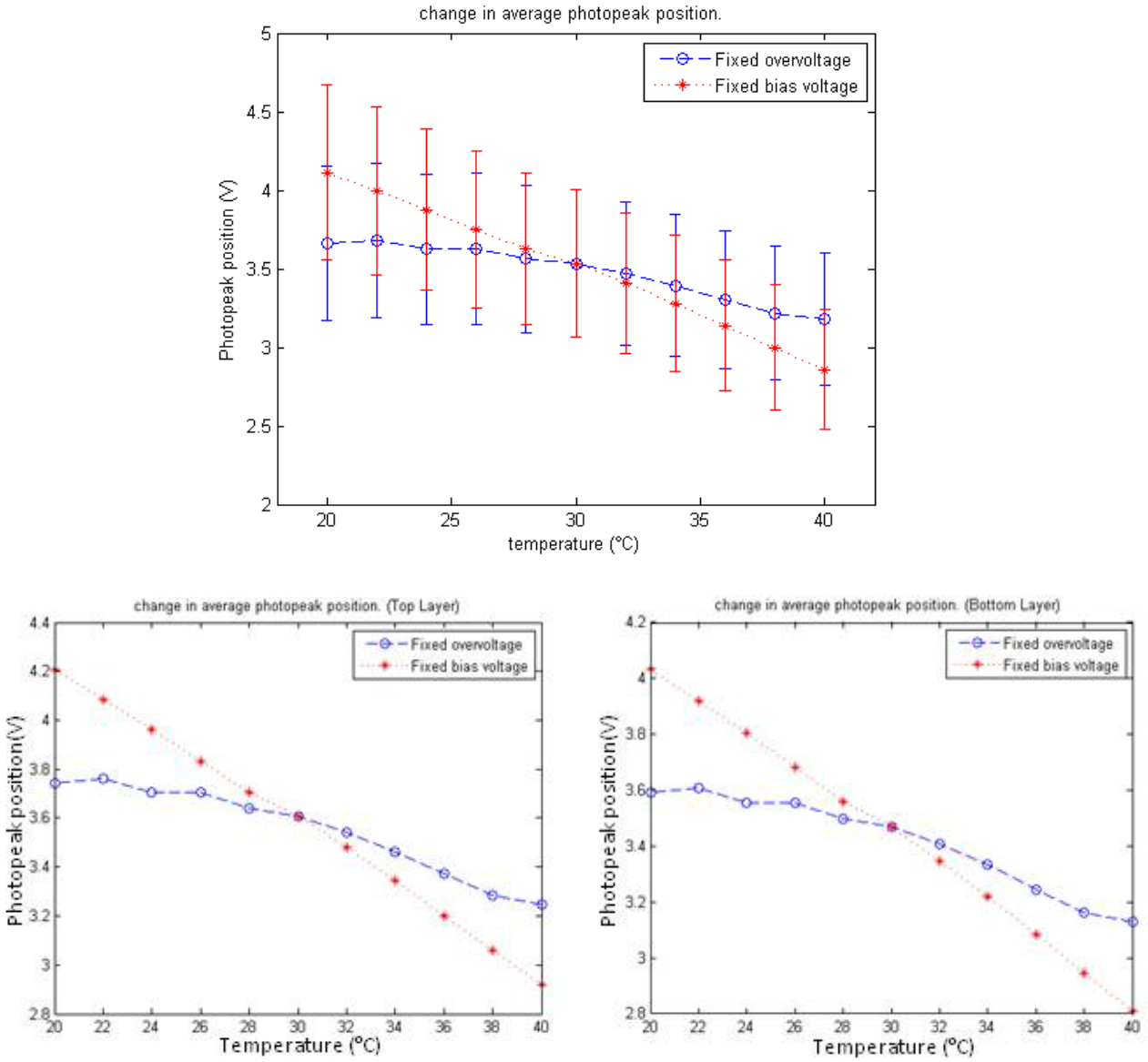

Figure 4-12. The average value of the photopeak voltage for the entire block (top), only the top layer (bottom left) and only the bottom layer (bottom right) at different temperatures.

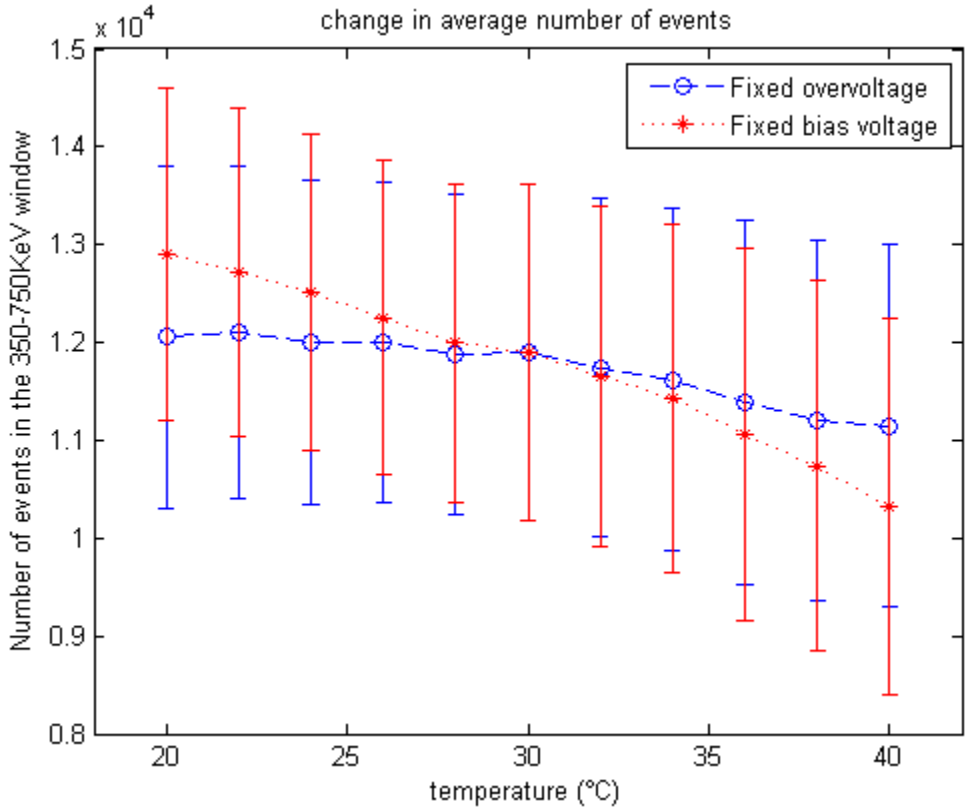

Figure 4-13. The average number of events in the reference energy window for different temperatures when a fixed overvoltage and a fixed bias voltage are applied.

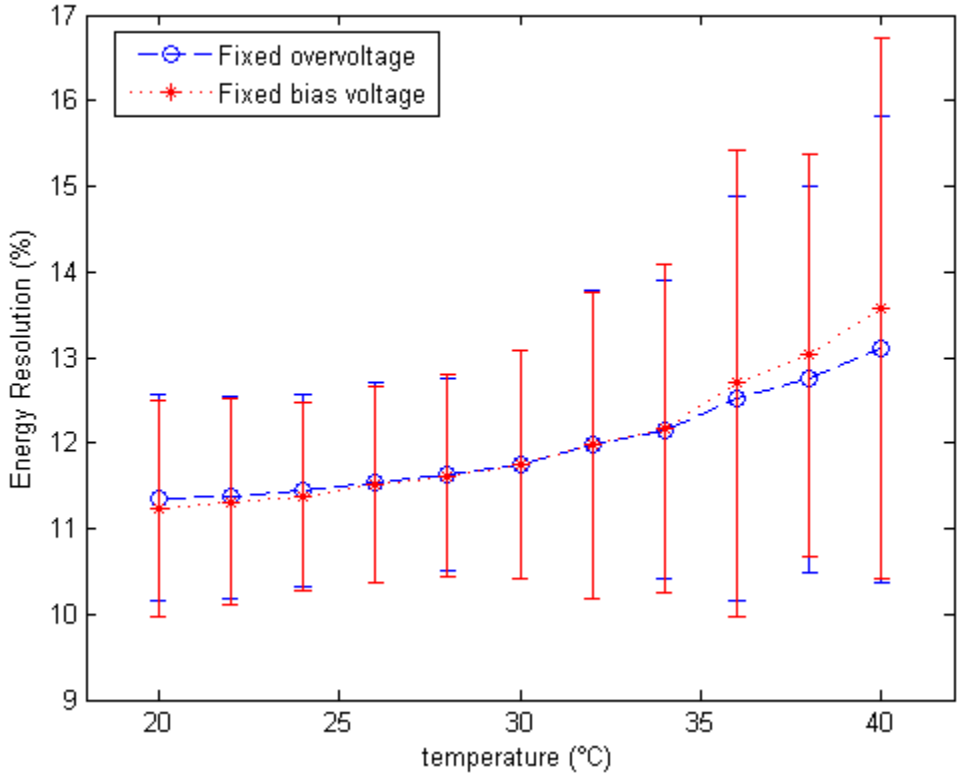

Figure 4-14. Average energy resolution at different temperatures when a fixed bias voltage and a fixed overvoltage are applied.

4.2.2.9 Discussion

Maintaining a fixed OV is effective in mitigating the shift in the photopeak position as a result of changes in temperature. The effect of maintaining a fixed OV can also be seen in maintaining a stable number of events across a range of temperatures. As depicted in Figure 4-11, the 350keV and 750keV markers at 30°C encompass most of the content of the energy histogram at 26°C and 40°C except for the Compton scattered photons. It is therefore plausible to assume that the shift in photopeak will not have as drastic an effect on the number of events within this window as on a narrower energy window.

The SiPM is not the only component in the detector module whose output is susceptible to changes in temperature and bias voltage. Variations in output might stem from other components such as the crystal block and electronics. The luminescence intensity of the crystals affects the output signal of the detector module. This intensity can be modeled by equation 4-1 where ΔE denotes activation energy and k the Boltzmann constant (Chen, Liu, Shi, Ren, & Zimmerer, 2005). Figure 4-15 shows the photopeak position data fit by a curve conforming to equation 4-1. It can be inferred from Figure 4-15 that the data support the conjecture that the variation in detector output despite a fixed overvoltage might be due to variations in the intensity of light output from the crystal block. Although the curve seems to be an acceptable model to describe the output of the detector module with a fixed OV, it is also possible to approximate the data by a line as depicted in Figure 4-15. The slope of this line was found to be 0.0261V for each degree of change in temperature.

$$I(T) = \frac{I(0)}{1 + A exp(-\frac{\Delta E}{kT})} \qquad \textbf{Equation 4-1}$$

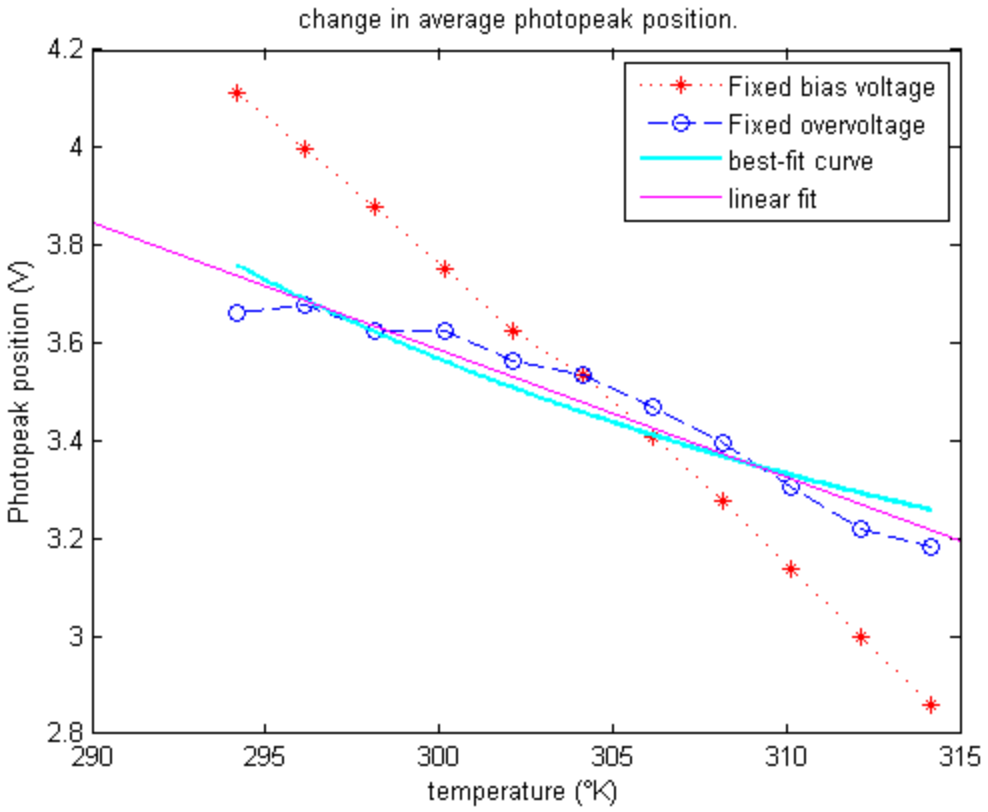

Figure 4-15. The change in average photopeak position is reduced by maintaining a fixed overvoltage. A curve fit to data demonstrates that the instability observed might be due to the effect of the scintillation block. This curve can be reasonably approximated by a line.

It is desirable to stabilize the output of the detector module so that the blue circles in Figure 4-15 line up along a flat horizontal line. If the dependence of the photopeak position is known on OV, it seems possible to adjust bias voltage with changes in temperature to achieve a fully stable photopeak position beyond what has now been achieved with maintaining a fixed OV. To this end, the dependence of photopeak position on OV must be studied for the detector module. The next section describes the results of such a study.

4.2.3 The Effect of overvoltage on detector output

This experiment aimed to characterize the dependence of average photopeak position for the crystal block on overvoltage. Based on the literature reviewed in chapter 1, it is fair to assume that this dependence will remain unchanged at other temperature points. The temperature point chosen to conduct the experiment was 30°C. This temperature has been shown in our study of the gantry's temperature profile to be close to the equilibrium operating temperature of a detector module inside the MR system.

The materials used in this experiment are identical to those of section 3.4. Data were acquired while the thermistor in the chamber reported a temperature within 0.1°C of the target temperature. At 30°C, data were acquired after setting the bias voltage to a value corresponding with OVs between 2.1V and 3.5V in increments of 0.1V. Data were acquired for 600s at each voltage and the DC offset in the signal was adjusted prior to each acquisition using the NIM 778 and NIM 740 offset adjustment screws. The level of the DC offset changes with temperature because it is dependent on the rate of dark current and also crosstalk between SiPM microcells, both of which are dependent on temperature.

The same steps as described in the previous section were followed to analyze each flood acquisition. The BDA and SpectraAnalyzer programs were used and the photopeak position was found by fitting a Gaussian curve to the energy histograms for each crystal.

4.2.3.10 Results

Figure 4-16 shows the average photopeak position for the crystal block at each OV along with its standard deviation. The dotted line is the average of all linear fits to individual crystal data. The slope of the line is 2.25±0.34V volts of change in photopeak position per 1V change in OV.

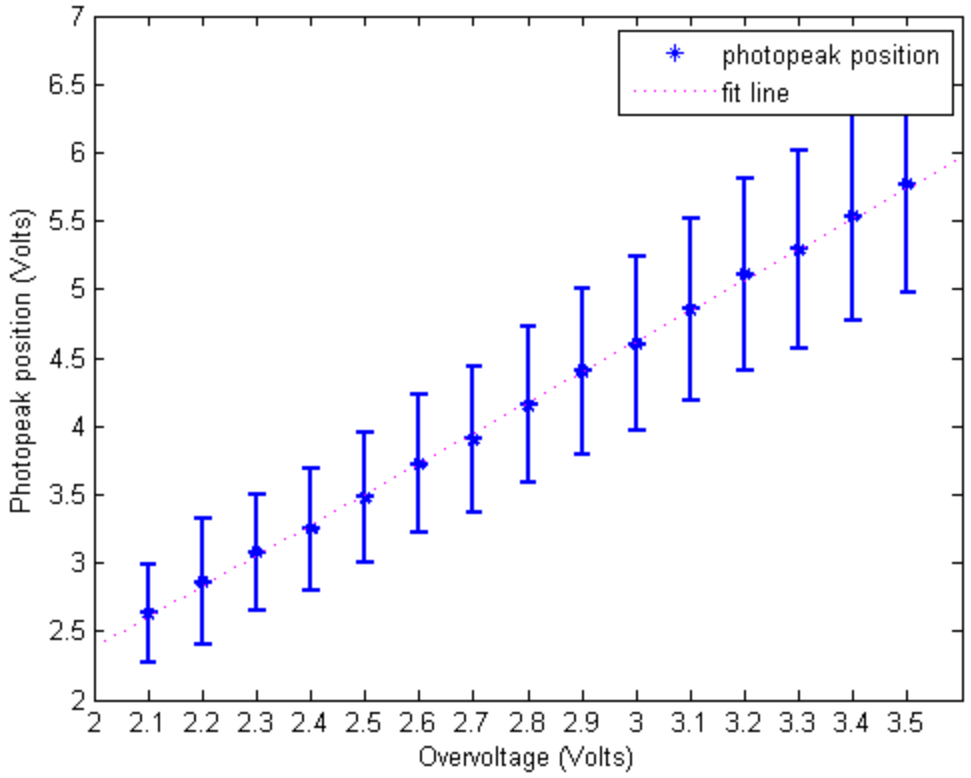

Figure 4-16. Average photopeak position at different overvoltage points at 30C.

4.2.3.11 Discussion

The results in this section corroborate the results from literature, discussed in chapter 1, that the gain of a SiPM changes linearly with bias voltage at a fixed temperature. Based on results from the literature, it is conjectured that the change in the average photopeak position for a fixed change in OV is independent of temperature. With this assumption, the results from this section could be used to stabilize detector output beyond what was done in section 4.2.2.

4.2.4 Output stabilization by adjustment of overvoltage

Maintaining a fixed OV is not sufficient to stabilize detector output because the output is also affected by other components, most prominent of which is the crystal block. However, at a given temperature, the SiPM bias voltage could be adjusted so that the output of the detector module is closer to what is desired for stable operation of the PET system. The goal of this experiment is to evaluate if it is feasible to maintain stable detector output (the indicators of which are taken to be photopeak position, energy resolution and the number of events within a reference window) by adjusting the bias voltage at each temperature. Adjustment of bias voltage in this experiment is not done to achieve a fixed OV, but to achieve the same output properties as those of the baseline temperature by using results from section 4.2.3.

4.2.4.12 Methods

The baseline temperature was chosen to be 30°C similar to previous experiments in this chapter. Four other temperature points were selected at 20, 25, 35 and 40°C. Data was acquired at the baseline temperature first with an OV of 2.5V. Then the temperature was set to 20°C and data was acquired at this and other temperature points in the order mentioned above for 600s and when the temperature sensor reported temperatures within 0.1°C of the target temperature. The DC offset was also removed prior to each acquisition. Data acquisition methods and materials were identical to what was described in section 4.2.2.

To determine the bias voltage at each temperature other than the baseline temperature, results from sections 4.2.2 and 4.2.3 were used together. First, at each temperature point the results from section 4.2.2 were used to determine the expected value of the mean photopeak position at that temperature (this value was known for 20°C and 40°C, but had to be interpolated for 35°C and 25°C by consulting the linear fit depicted in Figure 4-15). Once the value of the expected

photopeak position was known, the difference between this value and the mean photopeak position at the baseline temperature was determined. This difference is the amount by which the output has to be adjusted to remain stable. To compensate for this difference, the OV has to be adjusted. The amount of this adjustment was inferred from the data from section 4.2.3 which associates a change of 225mV in photopeak position for a change of 0.1V in OV. For example, for T=25°C, the change in photopeak position compared to that at 30°C is equal to 0.1305V because each degree Celsius decrease in temperature would increase the photopeak position by 0.0261V. To decrease the photopeak position by 0.1305V by changing the value of the OV, it would suffice to decrease OV by 0.06V since each 0.1V decrease in OV would lead to a decrease of 224mV in photopeak position. Table 4-1 lists the adjustment required at each temperature derived with the same method for all temperatures tested in this experiment.

Temperatue (°C)	**Expected change in photopeak position(V) @ OV=2.5V compared to baseline temperature**	**Adjustment in OV required to remove difference**
20	0.2610	-0.12V
25	0.1305	-0.06V
35	-0.1305	0.06V
40	-0.2610	0.12V

Table 4-1. The lookup table representing required change in the fixed overvoltage to achieve a stable detector output.

Data were also acquired at each temperature when the bias voltage was set to an overvoltage of 2.5V at that temperature, and to a value equal to an OV of 2.5V at the baseline temperature (27.20V).

4.2.4.13 Results

Figure 4-18 shows the percentage value of the difference between the photopeak position at each temperature and 30°C on a color-coded scale for each individual crystal and each layer. Figure

4-19 and Figure 4-20 show the value of the photopeak positions for the crystal block for the top and bottom layers respectively. Figure 4-17 depicts the average photopeak position value for the entire block at all tested temperatures with its standard deviation.

Using the method described in section 4.2.2 to calculate the number of events within the 350keV-750keV reference window defined at the baseline temperature, Figure 4-21 was obtained showing the change in the average number of counts for each block.

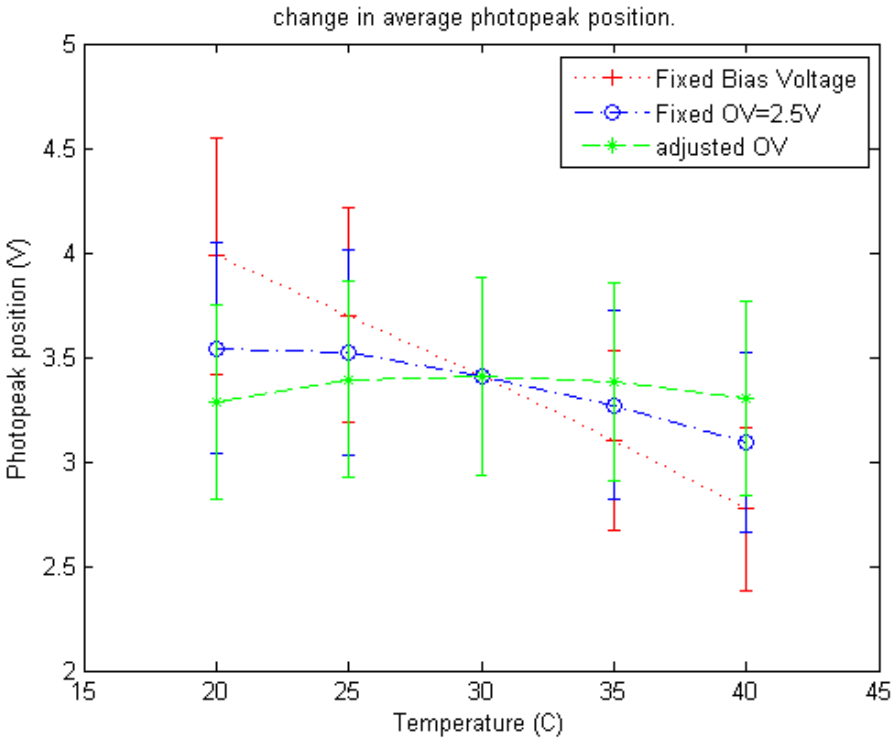

Figure 4-17. Average photopeak position plotted at different temperatures for three cases: fixed bias voltage, fixed overvoltage, and adjusted overvoltage.

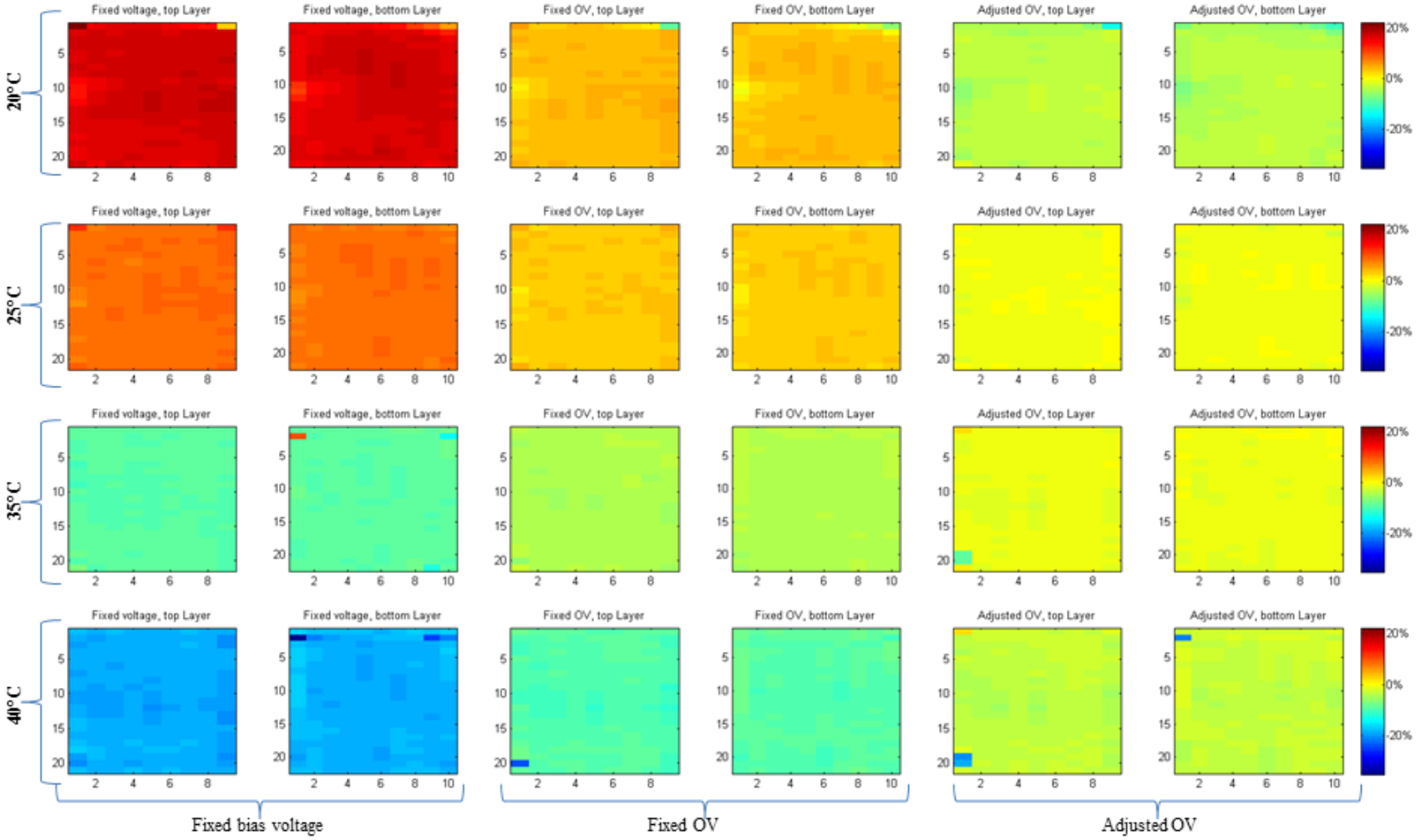

Figure 4-18. Change in the value of photopeak position compared to 30C when dynamic bias adjustment is applied.

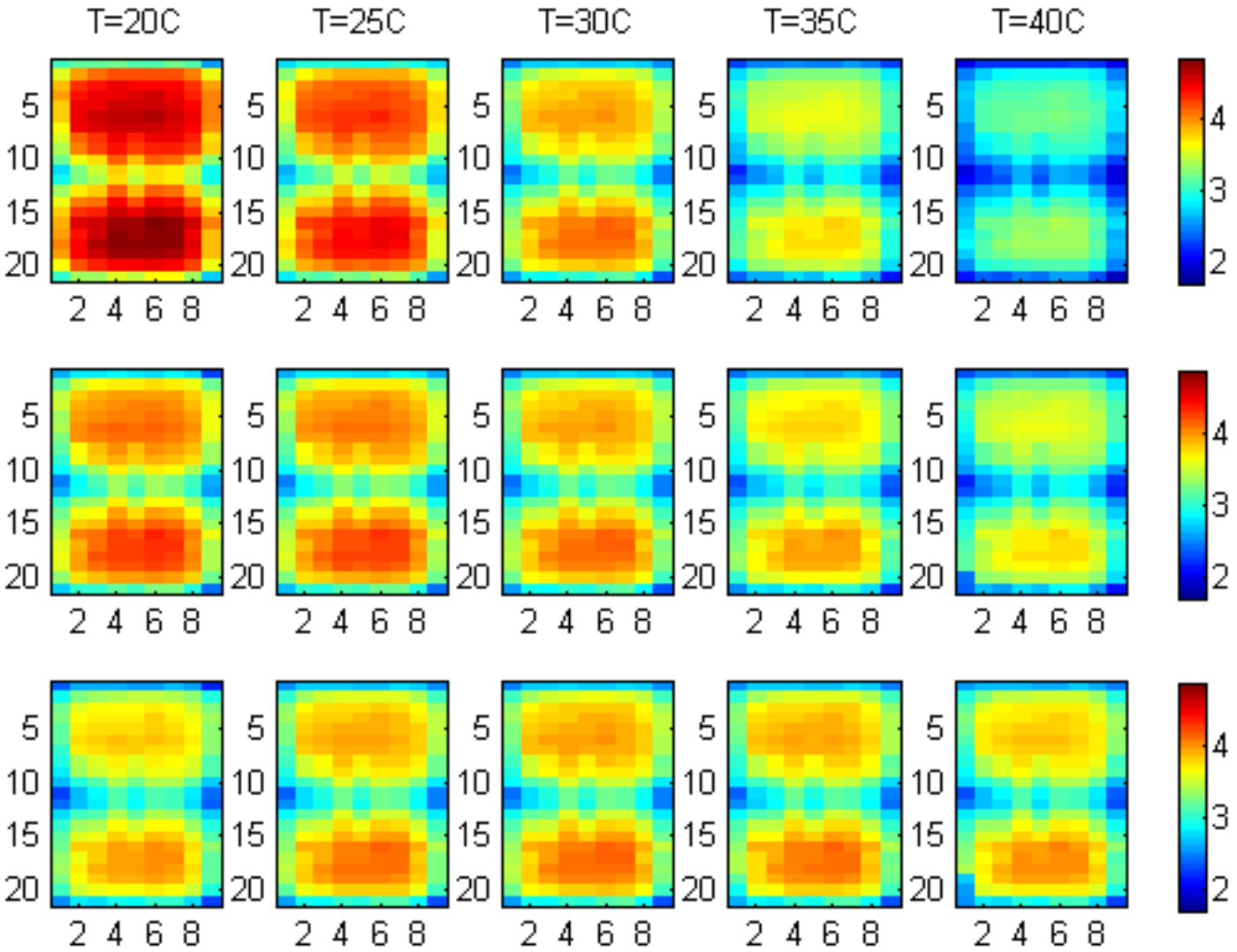

Figure 4-19. The absolute position of the photopeak for the top layer for three different cases. Top row: fixed bias voltage, middle row: fixed overvoltage, bottom row: dynamically adjusted bias voltage based on the lookup table.

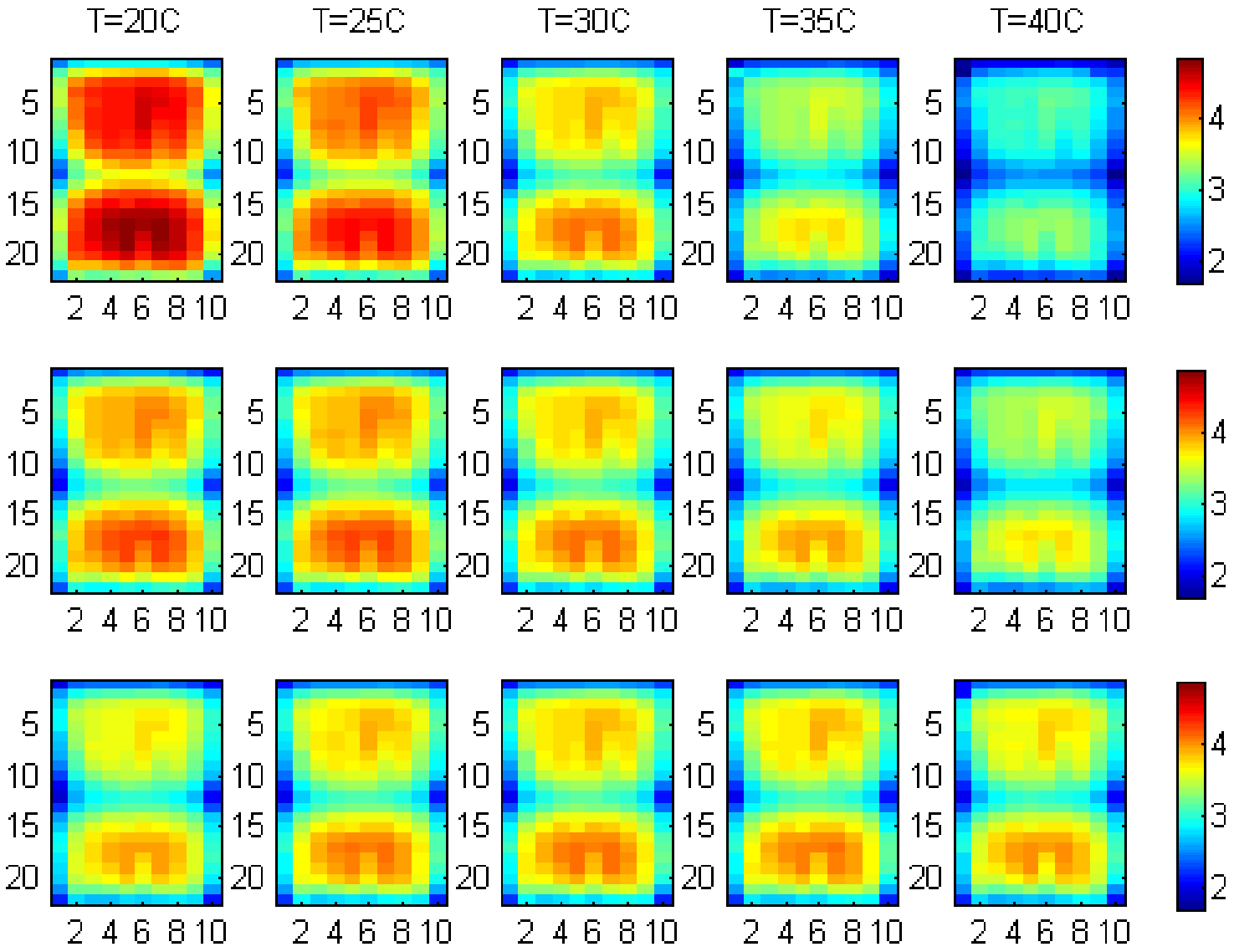

Figure 4-20. The absolute position of the photopeak for the bottom layer for three different cases. Top row: fixed bias voltage, middle row: fixed overvoltage, bottom row: dynamically adjusted bias voltage based on the lookup table.

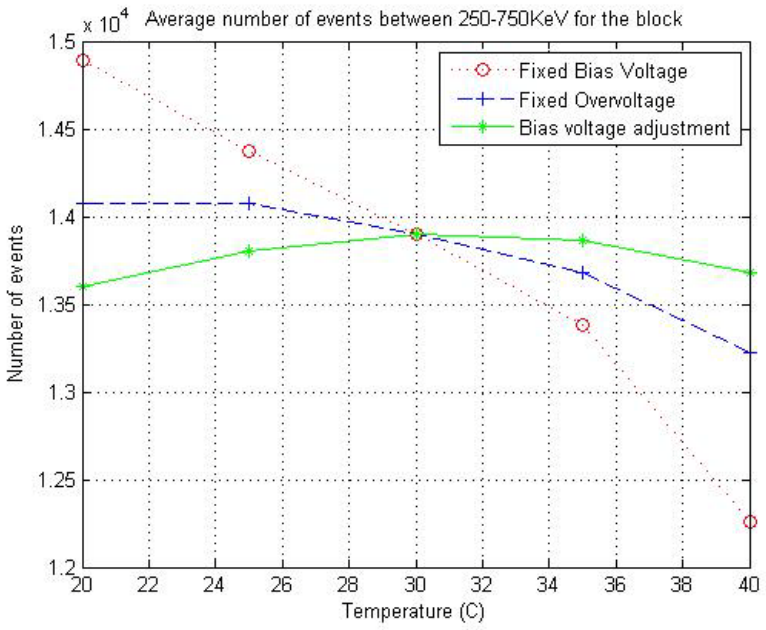

Figure 4-21. The number of events within the reference energy window for three different cases of a fixed bias voltage, fixed overvoltage and dynamically adjusted bias voltage based on the lookup table.

4.2.4.14 Discussion

Comparison of photopeak positions for individual crystals reveals that when the method in this section is employed to compensate for changes in temperature, the detector output is the most stable in terms of its photopeak position and signal shape (as indicated by the FWHM of the signal or its energy resolution). This stability is evident in the similarity of the photopeak maps in Figure 4-19 and Figure 4-20. Also the photopeak maps representing the percentage value of shift in photopeak position show that this change is closest to zero value when this method of compensation is applied.

The stability of the photopeak position leads to a stable number of events being detected in the reference energy window. This stability is most evident at temperatures closest to the baseline temperature. Experiments described in chapter 2 provide evidence that the operating temperature will most likely not fluctuate widely beyond the equilibrium value. Results from this section lend credence to the compensation method described to stabilize the output of the detector modules.

Chapter 5

Summary and the outlook for future work

5.1 Summary

The slow control system developed as part of this thesis project enables the remote monitoring and control of detectors in a PET insert system by providing a scalable platform. Use of a TCP/IP network for communication between components in this system makes configuration and troubleshooting easier.

Because calibration data are only gathered at a baseline temperature, it is important for the PET system to have a strategy to deal with temperature fluctuations. Tests performed in this project revealed that the extent of such fluctuations is not very wide, but that they would nonetheless affect the reliability of the PET system. The PET system relies on the position of the photopeak to define the window of energies within which events are accepted.

The strategy adopted and studied in this project was to use the detector's bias voltage to compensate for the shift in photopeak caused by a change in temperature. Tests revealed that the ambient temperature experienced by the detector module was close to 30°C. A wide array of temperatures was selected to study the efficacy of the adopted strategy. The ideal bias voltage at the baseline temperature was selected so that changes of as much as 10 degrees Celsius in temperature would not render the resulting flood image too noisy for processing. The position of the photopeak, energy resolution and the number of events falling within a reference window defined at the baseline temperatures were chosen as indicators of output stability.

Maintaining a fixed overvoltage helped stabilize the output of the detector, but it was not sufficient to compensate for the temperature-dependent properties of the crystal block and

components other than the SiPM. It was conjectured that dynamic adjustment of bias voltage would help with better stabilization of the output.

To achieve better stability, the effect of overvoltage at a fixed temperature on photopeak position was studied. A simple linear relationship was observed between overvoltage and photopeak position. The literature also corroborated this linear relationship. Based on the literature, it was assumed that the linear relationship would remain unchanged at any temperature. A lookup table was constructed to yield the value of bias voltage based on temperature. A baseline temperature (30°C) as well as four other temperature points were selected to test the hypothesis that dynamic adjustment of bias voltage based on the lookup table would be more effective at stabilizing detector output.

Dynamic adjustment of overvoltage achieved better stabilization of detector output than maintaining a fixed overvoltage. Results obtained by using this method kept the photopeak position almost fixed for temperatures that were as much as 5 degrees apart from the baseline. The results were always better than maintaining a fixed overvoltage.

5.2 Future Work

The number of detectors in the PET insert system is projected to increase from the current 16 in the prototype to as many as 128 detectors. The increase in the number of detectors might lead to a higher equilibrium temperature around the gantry. It therefore may be necessary for the slow control system to actively cool the gantry in order to keep the operating temperature within acceptable levels. Air cooling of the gantry seems to be the most plausible method.

The slow control system must be equipped to calibrate the detector modules to adjust parameters such as breakdown voltage. The calibration of detector modules in the prototype has been

performed on the bench top. However, changes in one or more detector modules would necessitate re-calibration which must be a feature of the slow control system. Re-calibration should lead to subsequent changes in the lookup table used for temperature compensation.

A more reliable sensor position unaffected by the immediate effects of heat sources on the detector module is required to get readings of ambient temperature. Tests in this thesis project revealed that the current temperature sensor on the detector module is placed too close to amplifiers and is affected by their heat. Placing the temperature sensors closer to the far edge of SiPMs is more conducive to obtaining an accurate measurement of ambient temperature.

The current DIB has to be modified to accommodate the transmission of bias voltage with a negative polarity to the detector modules based on B-Series SiPMs as described in chapter 2. A number of other modifications are also required to achieve an integral slow control system, such as:

- Housing the DIBs in a rack-mountable enclosure
- Incorporating a mechanism on the DIB enclosures for safe power-down and reboot of DIBs and embedded computers
- Providing a small display screen on the enclosure to indicate emergencies and messages

The slow control system is envisioned to integrate into a complete user interface for data acquisition and system control. It would benefit from modular development, distributed architecture and removal of single points of failure.

References

Amaudruz, P., Bishop, D., Gilhully, C., Goertzen, A., James, L., Kozlowski, P., … Thompson, C. J. (2014). Pixelated Geiger-Mode Avalanche Photo-Diode Characterization Through Dark Current Measurement. *IEEE Transactions on Nuclear Science*, *61*(3), 1369–1375.

Anderhub, H., Backes, M., Biland, a., Boller, a., Braun, I., Bretz, T., … Weitzel, Q. (2011). A G-APD based Camera for Imaging Atmospheric Cherenkov Telescopes. *Nuclear Instruments and Methods in Physics Research Section A: Accelerators, Spectrometers, Detectors and Associated Equipment*, *628*(1), 107–110.

Anger, H. O. (1958). Scintillation Camera. *Review of Scientific Instruments*, *29*(1), 27.

Basu, S., Kwee, T. C., Surti, S., Akin, E. a, Yoo, D., & Alavi, A. (2011). Fundamentals of PET and PET/CT imaging. *Annals of the New York Academy of Sciences*, *1228*, 1–18.

Beyer, T., Czernin, J., & Freudenberg, L. S. (2011). Variations in Clinical PET/CT Operations: Results of an International Survey of Active PET/CT Users. *Journal of Nuclear Medicine* , *52* (2), 303–310.

Catana, C., Wu, Y., Judenhofer, M. S., Qi, J., Pichler, B. J., & Cherry, S. R. (2006). Simultaneous Acquisition of Multislice PET and MR Images: Initial Results with a MR-Compatible PET Scanner. *Journal of Nuclear Medicine* , *47* (12), 1968–1976.

Chatziioannou, A. F. (2002). Molecular imaging of small animals with dedicated PET tomographs. *European Journal of Nuclear Medicine and Molecular Imaging*, *29*(1), 98–114.

Chen, Y., Liu, B., Shi, C., Ren, G., & Zimmerer, G. (2005). The temperature effect of Lu2SiO5:Ce3+ luminescence. *Nuclear Instruments and Methods in Physics Research Section A: Accelerators, Spectrometers, Detectors and Associated Equipment*, *537*(1-2), 31–35.

Delso, G., & Ziegler, S. (2009). PET/MRI system design. *European Journal of Nuclear Medicine and Molecular Imaging*, *36 Suppl 1*(December 2008), S86–92.

Feege, N. (2008). *Silicon Photomultipliers: properties and applications in a highly granular calorimeter (Master of Science thesis).* Universitat Hamburg.

Goertzen, A. L., Thiessen, J. D., Zhang, X., Liu, C.-Y., Berg, E., Bishop, D., … Thompson, C. J. (2012). Application of HDMI® cables as an MRI compatible single cable solution for Readout and power supply of SiPM based PET detectors. In *2012 IEEE Nuclear Science Symposium and Medical Imaging Conference Record (NSS/MIC)* (pp. 3184–3188). IEEE.

Hamamtsu Photonics. (2007). *Photomultiplier tubes, basics and applications*.accessed at *https://www.**hamamatsu**.com/resources/pdf/.../**PMT**_handbook_v3aE.pdf (October, 2014).*

Handler, W. B., Gilbert, K. M., Peng, H., & Chronik, B. a. (2006). Simulation of scattering and attenuation of 511 keV photons in a combined PET/field-cycled MRI system. *Physics in Medicine and Biology*, *51*(10), 2479–91.

Holl, I., Lorenz, E., Natkaniez, S., Renked, D., & Schmelz, C. (1995). Some Studies of Avalanche Photodiode Readout of Fast Scintillators, *42*(4).

Hong, S. J., Kang, H. G., Ko, G. B., Song, I. C., Rhee, J.-T., & Lee, J. S. (2012). SiPM-PET with a short optical fiber bundle for simultaneous PET-MR imaging. *Physics in Medicine and Biology*, *57*(12), 3869–83.

Judenhofer, M. S., Siegel, S. B., Cherry, S. R., Claussen, C. D., & Pichler, B. J. (2007). PET / MR Images Acquired with a Detector in a 7-T Magnet 1 Purpose : Methods : Results : Conclusion :, *244*(3), 807–814.

Judenhofer, M. S., Wehrl, H. F., Newport, D. F., Catana, C., Siegel, S. B., Becker, M., … Pichler, B. J. (2008). Simultaneous PET-MRI: a new approach for functional and morphological imaging. *Nature Medicine*, *14*(4), 459–65.

Kaplan, a. (2009). Correction of SiPM temperature dependencies. *Nuclear Instruments and Methods in Physics Research Section A: Accelerators, Spectrometers, Detectors and Associated Equipment*, *610*(1), 114–117.

Lee, J. S., & Kang, K. W. (2008). Clinical PET and PET/CT. In E. E. Kim, M.-C. Lee, T. Inoue, & W.-H. Wong (Eds.), *Clinical PET and PET/CT* (pp. 373–390). New York, NY: Springer New York.

Lewis, J. S., Achilefu, S., Garbow, J. R., Laforest, R., & Welch, M. J. (2002). Small animal imaging. current technology and perspectives for oncological imaging. *European Journal of Cancer (Oxford, England : 1990)*, *38*(16), 2173–88.

Lucas, a J., Hawkes, R. C., Ansorge, R. E., Williams, G. B., Nutt, R. E., Clark, J. C., … Carpenter, T. a. (2006). Development of a combined microPET-MR system. *Technology in Cancer Research & Treatment*, *5*(4), 337–41.

Marrocchesi, P. S., Bagliesi, M. G., Batkov, K., Bigongiari, G., Kim, M. Y., Lomtadze, T., … Zei, R. (2009). Active control of the gain of a Silicon PhotoMultiplier. *Nuclear Instruments and Methods in Physics Research Section A: Accelerators, Spectrometers, Detectors and Associated Equipment*, *602*(2), 391–395.

Muehllehner, G., & Karp, J. S. (2006). Positron emission tomography. *Physics in Medicine and Biology*, *51*(13), R117–37.

Petasecca, M., Alpat, B., Ambrosi, G., Azzarello, P., Battiston, R., Ionica, M., … Haino, S. (2008). Thermal and Electrical Characterization of Silicon Photomultiplier. *IEEE Transactions on Nuclear Science*, *55*(3), 1686–1690.

Phelps, M. E. (2000). PET: The Merging of Biology and Imaging into Molecular Imaging. *Journal of Nuclear Medicine , 41* (4), 661–681.

Pichler, B. J., Wehrl, H. F., Kolb, A., & Judenhofer, M. S. (2008). Positron emission tomography/magnetic resonance imaging: the next generation of multimodality imaging? *Seminars in Nuclear Medicine*, *38*(3), 199–208.

Ramilli, M. (2008). Characterization of SiPM: temperature dependencies. … *Symposium Conference Record, 2008. NSS'08. …*, 4–7.

Ravindranath, B., Junnarkar, S. S., Purschke, M. L., Maramraju, S. H., Hong, X., Tomasi, D., … Schlyer, D. J. (2009). Results from prototype II of the BNL simultaneous PET-MRI dedicated breast scanner. *2009 IEEE Nuclear Science Symposium Conference Record (NSS/MIC)*, 3315–3317.

Raylman, R. R., Majewski, S., Lemieux, S. K., Velan, S. S., Kross, B., Popov, V., … Marano, G. D. (2006). Simultaneous MRI and PET imaging of a rat brain. *Physics in Medicine and Biology*, *51*(24), 6371–9.

Shah, K. S., Farrell, R., Grazioso, R., Myers, R., & Cirignano, L. (2001). Large-area APDs and monolithic APD arrays. *IEEE Transactions on Nuclear Science*, *48*(6), 2352–2356.

Shams, E., Thiessen, J., Bishop, D., Kozlowski, P., Retiere, F., Sossi, V., … Goertzen, A. (2013). A PET detector interface board and slow control system based on the raspberry Pi®. In *IEEE Nuclear Science Symposium and medical Imaging Conference (NSS/MIC)*.

Shao, Y., Cherry, S. R., Farahani, K., Slates, R., Silverman, R. W., Meadors, K., … Garlick, P. B. (1997). Development of a PET detector system compatible with MRI/NMR systems. *IEEE Transactions on Nuclear Science*, *44*(3), 1167–1171.

Strul, D., Cash, D., Keevil, S. F., Halsted, P., Williams, S. C. R., & Marsden, P. K. (2003). Gamma shielding materials for MR-compatible PET. *IEEE Transactions on Nuclear Science*, *50*(1), 60–69.

Vandenbroucke, a, McLaughlin, T. J., & Levin, C. S. (2012). Influence of temperature and bias voltage on the performance of a high resolution PET detector built with position sensitive avalanche photodiodes. *Journal of Instrumentation*, *7*(08), P08001–P08001.

Vinogradov, S. (2012). Analytical models of probability distribution and excess noise factor of solid state photomultiplier signals with crosstalk. *Nuclear Instruments and Methods in Physics Research Section A: Accelerators, Spectrometers, Detectors and Associated Equipment*, *695*, 247–251.

Wehrl, H. F., Judenhofer, M. S., Wiehr, S., & Pichler, B. J. (2009). Pre-clinical PET/MR: technological advances and new perspectives in biomedical research. *European Journal of Nuclear Medicine and Molecular Imaging*, *36 Suppl 1*, S56–68.

Yamamoto, S., Hatazawa, J., Imaizumi, M., Shimosegawa, E., Aoki, M., Sugiyama, E., … Detectors, A. D. O. I. B. (2009). A Multi-Slice Dual Layer MR-Compatible Animal PET System, *56*(5), 2706–2713.

Yamamoto, S., Satomi, J., Watabe, T., Watabe, H., Kanai, Y., Imaizumi, M., … Hatazawa, J. (2011). A temperature-dependent gain control system for improving the stability of Si-PM-based PET systems. *Physics in Medicine and Biology*, *56*(9), 2873–82.

Zaidi, H., Ojha, N., Morich, M., Griesmer, J., Hu, Z., Maniawski, P., … Shao, L. (2011). Design and performance evaluation of a whole-body Ingenuity TF PET-MRI system. *Physics in Medicine and Biology*, *56*(10), 3091–106.

Appendices

Appendix A: The slow control software system, architecture and functionality

A.1) The DIB client program

The DIB client program is developed in the Python programming language. Its main objective is to interact with the electronic components on the DIB such as the DAC and the ADC and to report values of operational parameters to the host PC control program. It also implements low level control of the detector modules to prevent damage and deal with emergencies in cases where the network connection might be broken. It relies on a TCP/IP socket to communicate with the host PC control program.

Classes and Methods

The following list describes the classes, what classes they inherit from, and their methods along with a brief decription.

- The DETClient class
  - Inherits from: asyncore.dispatcher
  - Description: This is an asyncore client that handles the connection to the host PC. More information regarding asyncore can be found in the documentation for the Python programming language.
  - Members:
    - Private members:
      - Buffer: implements the buffer interface to communicate messages to the server and holds server commands.
      - t: this is the thread that is tarted inside of the client to access board hardware.
      - Log_file_name: the name of the log file stored on the client.
      - _connection_established: This is a Boolean variable whose value indicates whether or not the connection has been established.
  - Methods:
    - Private methods:
      - Handle_connect: This is an event handler called when connection is established.

- Handle_write_event: This is an event handler which overrides the same method in asyncore. This methods first instantiates a ReceiverBoard module and assigns that instance to the t variable. It is then assigned to a separate thread of execution.
- Restart_monitor_thread: restarted the thread running the receiverboard module by calling its start() method again.
- sendCommand: sends a command to the host PC program.
- handle_error
- handle_close: event handler called when connection is terminated.
- handle_read: event handler called to read data from the receive buffer.
- report_my_ID
- shutdown_pi
- handle_write: this is an event handler called when the buffer member has data that need to be sent to the server
- parse_config_command: This method parses a command sent by server containing changes to the config settings.

  - Public methods:
    - sendErrorMessageToServer
    - initiateConnectionWithServer

- The I2CBus class
  - Description: This class is a wrapper around the quick2wire.i2c class developed by Quick2Wire (www.quick2wire.com) and published under the terms of the GNU Lesser General Public License (LGPL) Version 3. The existence of a wrapper class makes it easier to use the quick2wire.i2c class for the specific purpose of communicating with the ADC and the DAC on the DIB.
  - Members:
    - Private members:
      - I2C_sleep_time: time to wait between ADC accesses. This is equivalent to ADC conversion time according to the datasheet.
      - ADC_addr: Hardware address of the ADC on the I2C bus.
      - ADC_config: Setting or command value to write to the ADC.
      - DAC_addr: address of the DAC on the I2C bus
    - Public members: This class does not provide any public members.
  - Methods:
    - Private methods:
      - __init__: constructor method; instantiates a new object of the quick2wire.i2c class and makes it the bus master (note that the Raspberry Pi is considered the I2C bus master)
    - Public methods:
      - configure_bus_params: assigns values to the four private members of the class. This method could be called externally to change the value of the private members, or by the constructor method upon instantiation.

- read_target_value: Reads the digitized value corresponding to the I2C device (ADC)and channel
    - Arguments:
      target_channel: the input channel of the ADC to convert
      The first byte written to the ADC (target_channel) contains the input channel address that will be
      converted on the next cycle, and the second one (ADC_config) contains ADC
      description, refer to the LTC2499 datasheet.

- write_value_to_DAC: writes the DAC_taregt_value to the channel of the DAC specified by DAC_target_channel
    - Arguments:
      DAC_target_channel: The channel of the DAC the value should be
      written to DAC_target_value: Value to be written to DAC output

- The ReceiverBoard class
    - Inherits from: threading.Thread
    - Description: ReceiverBoard inherits from the threading.Thread class and can be run in an execution thread when its run() method is invoked by start(). The start() method is called by the DetClient class when a connection is established
      with server.
    - Members
        - Private members:
            - Config_file_name: This is a string holding the name of the configuration file.
            - Config: the configparser object to parse the config file and manage reading and writing from it. Refer to documentation of the Python configparser class for more information.
            - Bus: an instance of the I2C bus class.
            - Client: an instance of the DETClient class.
        - Public members:
          This class has many private members most of whom deal with the various settings in the configuration file. Variable names and the comments in the code make these members self-explanatory.
    - Methods
        - Private methods
            - __init__: constructor method that parses the config file and loads its settings into memory, initializes the I2C bus based on settings, and instantiates a new object of the class.
            - __convert_ADC_value_to_voltage: This is a protected method invoked from within the ReceiverBoard class to convert the value read from the digital output of the ADC to a voltage value based on the maximum value that the ADC can produce and the maximum voltage of the ADC.

- __process_channel_X: This is a protected method invoked from within the ReceiverBoard class to convert the value read from the output of the ADC to a bias voltage/current or temperature value (the coefficient that corresponds to the input of the ADC). The slope values are all calculated by multimeter measurements on the receiverboard in this version. The suffix _X in the name of this method is employed to make it easier to invoke the method based on the remainder of the division of the ADC channel number by the number 3. Refer to the documentation for the method monitor_ADC_channels_send_data_block
- __process_sys_bias: This method is invoked from within the ReceiverBoard class to convert the system bias current readback of the ADC to a current value.
-
-

- Public methods
  - Read_config_data: this method uses the configparser object to read the config file specified by config_file_name and assign values to class-wide private members. The config file follows the conventional section/option/value format of Python (for details refer to Python documentation).
  - Reconfigure_bus: In case the settings used to access the I2C bus are changed, these changes need to be immediately reflected to the I2C object. This method is called in case of such changes, and updates the members of the I2C bus object instantiated inside the ReceiverBoard class.
  - Run: Because the ReceiverBoard class is a threading class, any calls to its start() method will invoke the run() method to be executed un a separate thread of execution. The run method starts by setting the system bias to high and then enters a loop in which the following operations are serially performed: 1) all inputs of the ADC are queried and reported to the host PC control program by a call to the monitor_ADC_channels_send_data_block() method. 2) a check is made to see if any server commands have been received from the host PC control program that need processing.
  - monitor_ADC_channels_send_data_block
  - enable_sys_bias
  - disable_sys_bias
  - handle_det_bias_command: Processes a bias command received from the host PC to set the bias voltage for one or all detectors to a particular value.
  - power_down_all_det_biases
  - set_all_detector_biases
  - power_down_detector_bias
  - set_detector_bias: writes the value specified by target to the output of the DAC specified by det_number.

- report_det_bias_curve: This method responds to a “CURVE” server command. It starts by setting the detector voltage to the value specified by report_bias_curve_startV. It then gradually increases the bias voltage to the value specified by report_bias_curve_stopV, in increments of report_bias_curve_step_size, and reports the corresponding voltage, current and temperature measurements for the detector to the server in each step.
- update_config_entry: This method takes the section of the config file where the entry referred to by “key” is located and updates its value.
- write_back_config_file: opens the config file in write mode and writes the config object to file. This creates a text file from scratch that contains all config entries.
- send_config_values_to_server: sends all the data in config object to the host PC control program. Data is sent with each section/option/value string on one line.

A.2) The host PC control program

The host PC control program is developed in the LabWindows/CVI environment and exploits multithreading to process incoming connections from all DIBs simultaneously. The program does this by maintaining a list of connected clients (gClientList). A TCPServer object is instantiated and event handlers are defined to respond to events associated with this object. Some of the most important event handlers are as follows:

- ServerTCPCB: This is the TCP server's TCP callback. This function will receive event notification, similar to a UI callback, whenever a TCP event occurs. The program responds to CONNECT and DISCONNECT messages and indicate to the user when a client connects to or disconnects. When a client is connected, The program would respond to the DATAREADY event and read in the available data from the client and display it.
  - DisconnectClient: Disconnects a client from the server and removes it from the clients list
  - ConnectClient: Adds the client requesting the connection to the clients list

- DefferedSend & DeferredReceive: These two methods respectively send and receive messages from and to clients without interfering with the GUI. They are called by the PostDeferredCallToThread available in LabWindows.

A.3) Messages exchanged between the DIB client and the host PC control program

Communication between the two pieces of the slow control system takes place by exchanging text-based messages on a TCP/IP network. A messaging standard is defined through which commands from the host PC control program are communicated to the DIB client and reports are transmitted from the DIB back to the host PC. The following list outlines the messages and their standard format.

Commands sent by the host PC control program

system_bias_ON

- *Description:* This command is sent by the server to set the system bias voltage to high
- *Method invoked on client:* `enable_sys_bias` in the `ReceiverBoard` module

system_bias_OFF

- *Description:* This command is sent by the server to set the system bias voltage to low
- *Method invoked on client:* `disable_sys_bias` in the `ReceiverBoard` module

DETBIAS[detector_num]%[target_voltage]

- *Description:* sets the detector bias voltage for the detector specified by [detector_num] to the value specified by [target_voltage]. [detector_num] ranges between 0-4 where 0 specified all detectors.
- *Method invoked on client:* `handle_det_bias_command` in the `ReceiverBoard` module.
- *Example:* DETBIASA%0.00 (powers down all detectors)
- *Example:* DETBIAS2%10.25 (Sets bias voltage for detector 2 to 10.25 volts)

CURVE%[detector_num]

- *Description:* instructs the client to run the curve reporting routine, where the bias voltage of the detector is set to a start voltage and from there it is gradually increases by increments specified in the config file. At each step the corresponding values for bias current and bias temperature are read from the ADC and all data is sent to the server in one data block. (see the entry under client data blocks for the format of this data block). [detector_num] ranges between 1-4.
- *Method invoked on client:* `handle_det_bias_command` in the `ReceiverBoard` module.
- *Example:* CURVE2 : curve reporting routine for detector 2

settings

- *Description:* instructs the client that the data following this command in the buffer is a series of key/value entries that should be used to update the client config file.
- *Method invoked on client:* `parse_config_command` in the `DetClient` module.

getcnfg

- *Description:* Asks the client for a copy of config entries found in the client's config file.
- *Method invoked on client:* `send_config_values_to_server` in the `ReceiverBoard` module.

restart_thread

- *Description:* If the operation of the ReceiverBoard module has been terminated as a result of an exception, this command asks the client to restart the execution of the thread. If this command is set when the ReceiverBoard module is running, a non-fatal IO Error will result.
- *Method invoked on client:* `restart_monitor_thread` in the `DetClient` module.

Appendix B: Fit parameters and breakdown voltage values for the 36 SensL SPM ArraySB-4 used in building the PET insert prototype

The fitting function is the same as Equation 1-6 in Section 1.6.6.2. The following table lists the values for breakdown voltage, and also DC, N_{ca}, and β.

SiPM ID	V_{BD}	DC	N_{ca}	β
1	24.56497	9.355222	0	5.55E-16
3	24.54877	10.79986	3.89E-17	8.33E-16
4	24.51136	10.53304	0	2.22E-15
5	24.51887	10.83308	5.55E-18	6.11E-15
6	24.6109	11.39361	0	0
7	24.45219	13.30968	5E-17	0
8	24.51188	13.8773	1.11E-17	2.5E-15
9	24.53991	11.78637	3.89E-17	5.55E-16
10	24.57298	11.94951	4.44E-17	6.38E-15
11	24.55091	11.84674	6.11E-17	0
12	24.50538	13.07755	5E-17	8.33E-16
13	24.49112	11.55445	1.11E-17	0
14	24.53048	14.29799	0	0
15	24.49157	13.14246	5.55E-18	2.78E-16
16	24.54191	13.97337	2.78E-17	5.55E-16
17	24.55705	13.23919	0	0
18	24.49051	14.23021	2.78E-17	5.55E-16
19	24.59802	12.16245	5.55E-18	0
20	24.5992	12.87926	8.33E-17	0.025402

SiPM ID	V_{BD}	DC	N_{ca}	β
21	24.51845	13.10178	1.11E-17	2.78E-16
22	24.55568	12.06521	3.33E-17	2.78E-16
23	24.55358	11.84893	5.55E-18	1.54E-13
24	24.56775	12.55406	1.61E-16	0
25	24.54534	12.5822	5.55E-18	0
26	24.58809	13.04472	6.66E-17	0
27	24.59144	10.26022	0	2.22E-15
28	24.50805	12.85398	5.55E-18	2.78E-16
29	24.57576	11.93082	7.22E-17	0
30	24.58617	12.44512	1.11E-17	1.94E-15
31	24.49182	13.51392	0.002124	4.72E-15
32	24.56614	13.16466	1.11E-17	0
33	24.4598	13.61156	0	2.78E-16
34	24.58984	11.9705	6.11E-17	2.78E-16
35	24.54074	11.96836	0	2.78E-15
36	24.6099	11.82803	5.55E-18	2.78E-16
Mean	**24.54407**	**12.3299**	**5.9E-05**	**0.00111**
Std	**0.041313**	**1.162539**	**0.000354**	**0.00482**
Min	**24.45219**	**9.355222**	**0**	**0**
Max	**24.6109**	**14.29799**	**0.002124**	**0.025402**